New Analysis and Operational Control Algorithms for Islanded Microgrid Systems

by

Morad Mohamed Abdelmageed Abdelaziz

A thesis
presented to the University of Waterloo
in fulfillment of the
thesis requirement for the degree of
Doctor of Philosophy
in
Electrical and Computer Engineering

Waterloo, Ontario, Canada, 2014

AUTHOR'S DECLARATION

I hereby declare that I am the sole author of this thesis. This is a true copy of the thesis, including any required final revisions, as accepted by my examiners.

I understand that my thesis may be made electronically available to the public.

Abstract

Driven by technical, economic and environmental benefits for different stakeholders in the power industry, the electric distribution system is currently undergoing a major paradigm shift towards having an increasing portion of its growing demand supplied via distributed generation (DG) units. As the number of DG units increase; microgrids can be defined within the electric distribution system as electric regions with enough generation to meet all or most of its local demand. A microgrid should be able to operate in two modes, grid-connected or islanded. The IEEE standard 1547.4 enumerates a list of potential benefits for the islanded microgrid operation. Such benefits include: 1) improving customers' reliability, 2) relieving electric power system overload problems, 3) resolving power quality issues, and 4) allowing for maintenance of the different power system components without interrupting customers. These benefits motivate the operation of microgrid systems in the islanded mode. However the microgrid isolation from the main grid creates special technical challenges that have to be comprehensively investigated in order to facilitate a successful implementation of the islanded microgrid concept.

Motivated by these facts, the target of this thesis is to introduce new analysis and operational control algorithms to tackle some of the challenges associated with the practical implementation of the islanded microgrid concept. In order to accomplish this target, this study is divided into four perspectives: 1) developing an accurate steady-state analysis algorithm for islanded microgrid systems, 2) maximizing the possible utilization of islanded microgrid limited generation resources, 3) allowing for the decentralized operation of islanded microgrid systems and 4) enabling the islanded microgrid operation in distribution systems with high penetration of plug-in electric vehicles (PEVs).

First for the steady-state analysis of islanded microgrid systems, a novel and generalized algorithm is proposed to provide accurate power flow analysis of islanded microgrid systems. Conventional power flow tools found in the literature are generally not suitable for the islanded microgrid operating mode. The reason is that none of these tools reflect the islanded microgrid special philosophy of operation in the absence of the utility bus. The proposed algorithm adopts the real characteristics of the islanded microgrid operation; i.e., 1) Some of the DG units are controlled using droop control methods and their generated active and reactive power are dependent on the power flow variables and cannot be pre-specified; 2) The steady-state system frequency is not constant and is considered as one of the power flow variables. The proposed algorithm is generic, where the features of distribution systems i.e. three-phase feeder models,

unbalanced loads and load models have been taken in consideration. The effectiveness of the proposed algorithm, in providing accurate steady-state analysis of islanded microgrid systems, is demonstrated through several case studies.

Secondly, this thesis proposes the consideration of a system maximum loadability criterion in the optimal power flow (OPF) problem of islanded microgrid systems. Such consideration allows for an increased utilization of the islanded microgrid limited generation resources when in isolation from the utility grid. Three OPF problem formulations for islanded microgrids are proposed; 1) The OPF problem for maximum loadability assessment, 2) The OPF for maximizing the system loadability, and 3) The bi-objective OPF problem for loadability maximization and generation cost minimization. An algorithm to achieve a best compromise solution between system maximum loadability and minimum generation costs is also proposed. A detailed islanded microgrid model is adopted to reflect the islanded microgrid special features and real operational characteristics in the proposed OPF problem formulations. The importance and consequences of considering the system maximum loadability in the operational planning of islanded microgrid systems are demonstrated through comparative numerical studies.

Next, a new probabilistic algorithm for enabling the decentralized operation of islanded microgrids, including renewable resources, in the absence of a microgrid central controller (MGCC) is proposed. The proposed algorithm adopts a constraint hierarchy approach to enhance the operation of islanded microgrids by satisfying the system's operational constraints and expanding its loading margin. The new algorithm takes into consideration the variety of possible islanded microgrid configurations that can be initiated in a distribution network (multi-microgrids), the uncertainty and variability associated with the output power of renewable DG units as well as the variability of the load, and the special operational philosophy associated with islanded microgrid systems. Simulation studies show that the proposed algorithm can facilitate the successful implementation of the islanded microgrid concept by reducing customer interruptions and enhancing the islanded microgrid loadability margins.

Finally, this research proposes a new multi-stage control scheme to enable the islanded microgrid operation in the presence of high PEVs penetration. The proposed control scheme optimally coordinates the DG units operation, the shedding of islanded microgrid power demand (during inadequate generation periods) and the PEVs charging/discharging decisions. To this end, a three-stage control scheme is formulated in order to: 1) minimize the load shedding, 2) satisfy the PEVs customers' requirements and 3) minimize the microgrid cost of operation. The proposed control scheme takes into consideration; the variability associated with the output power of renewable DG units, the random behaviour of PEV

charging and the special features of islanded microgrid systems. The simulation studies show that the proposed control scheme can enhance the operation of islanded microgrid systems in the presence of high PEVs penetration and facilitate a successful implementation of the islanded microgrid concept, under the smart grid paradigm.

Acknowledgements

I would like to express my sincerest gratitude to my supervisor Professor Ehab El-Saadany for his professional guidance, valuable advice, continual support and encouragement shown throughout the period of this research. My appreciation and thanks are also extended to my Ph.D. committee members: Professor Magdy Salama, Professor Mehrdad Kazerani and Professor Keith Hipel. Thanks are also due to my external examiner, Professor Badrul Chowdhury, for his coming from North Carolina to referee this thesis.

I would like to express my deepest thanks to Darin Mohy, my wife and friend, for whom I would never find the right words to express my gratitude for her endless understanding, patience, encouragement, optimism and support during all these years of my Ph.D. studies.

I wish to also thank my parents; Professor Mohamed Abdelaziz and Mrs. Laila Riyad, who share credit in every goal I achieved or may achieve in my life. I am truly grateful and thankful for their continuous support, love and encouragement without which this thesis would not have been possible. Thanks are also due to my sisters, Rania and Heidi for their continuous support and encouragement during my studies.

I also wish to thank my Father and Mother in-law; Mr. Mohy Gad and Mrs. Nema Mostafa, as well as my Sister and Brother in-law; Doaa and Samer, who though are far away have always offered me their sincerest encouragement and support throughout the period of my PhD studies.

Last but not least, I would like to express my special appreciation and thanks to Professor Mostafa Marei whose support, interest, assistance and many hours of technical discussions during my Masters studies had forged and shaped my research interests.

Dedication

This thesis is dedicated to my daughter ***Serene***; the *sweetest* thing ever.

Table of Contents

List of Figures

List of Tables

Nomenclature

Acronyms

ADS	Active distribution system
ARMA	Auto regression moving average
CHP	Combined heat and power
CMSP	Cost minimization sub-problem
DFIG	Doubly fed induction generator
DG	Distributed generation
DNO	Distribution network operator
IID	Island isolation device
LIB	Limit-induced bifurcation
LSMSP	Load shedding minimization sub-problem
MCS	Monte Carlo simulation
MGCC	Microgrid central controller
MPPT	Maximum power point tracking
NLP	Non-linear programming
NR	Newton Raphson
OPF	Optimal power flow
PCC	Point of common coupling
PDF	Probability density function
PEV	Plug-in electric vehicle
PLL	Phase locked loop
SMSP	SOC maximization sub-problem

SOC	State of charge
SNB	Saddle node bifurcation

Indices

eq	Index of equations
i,j,k	Index of system buses
is	Index of islanded microgrids
it	Index of iterations
ℓ	Index of system loading points
p	Index of preference level in a constraint hierarchy
st	Index of states
t_k	Index of time step
vh	Index of PEV
ϕ	Index of system phases

Parameters

$c_{PEV-kWh}$	Cost of PEV discharge per *kWh*
$E^i(vh)$	PEV battery capacity for vehicle *vh* connected to bus *i*.
K^{pi},K^{ii}	Current controller proportional and integral gains, respectively
K^{pv},K^{iv}	Voltage controller proportional and integral gains, respectively
K_{pf}, K_{qf}	Active and reactive power frequency dependency factors, respectively
K_{pv}, K_{qv}	Active and reactive power voltage dependency exponents, respectively
L_f, C_f	DG unit output filter inductance and capacitance, respectively
n_{bus}	Number of system buses
n_{droop}	Number of droop buses in the system

n_{levels}	Number of constraint hierarchy levels of preference
n_{MG}	Number of possible islanded microgrids in the system under study
n_{states}	Number of islanded microgrid states
n_{pq}	Number of PQ buses in the system
n_{pv}	Number of PV buses in the system
N_p	Number of time slots in a prediction horizon τ
$N_{PEV}^{i}(t)$	Number of PEVs connected to bus *i* at time instant *t*
P_{Loi},Q_{Loi}	Active and reactive nominal load power at bus i, respectively
$S_{loss\&spare}$	Apparent power loss and spare capacity requirements for islanded microgrid
$S_{Gi,max}$	Apparent power generation capacity at bus *i*, respectively
$SOCI^{i}(vh)$	Initial SOC of vehicle *vh* connected to bus *i*
$SOC_{min}^{i}(vh)$	Minimum allowed SOC of vehicle *vh* connected to bus *i*
$SOCR^{i}(vh)$	Required SOC by vehicle *vh* connected to bus *i*
$t_d^i(vh)$	Departure time of vehicle *vh* at bus *i*
$\|V_i\|^{ub}$, $\|V_i\|^{lb}$	Upper and lower bounds on the allowable voltage magnitude at bus *i*, respectively
$v_{st,\,min}$, $v_{st,max}$	Wind speed limits of state *st*
W_L^i	Load point *i* priority weight
$\Gamma^{(is,st)}$	Parameter indicating the priority of islanded microgrid *is* at state *st*
$\Gamma_i^{(is,st)}$	Parameter indicating the priority of load point *i* when operating in islanded microgrid *is* at state *st*
$\eta^{i}(vh)$	Charging/discharging efficiency for vehicle *vh* connected to bus *i*
$\lambda_{ub}^{(is,st)}$	Upper bound on the loading factor of islanded microgrid *is* at state *st*

$\rho_{st}^{G}, \rho_{st}^{L}, \rho_{st}$	Probability of generation, load, and combined states, respectively
τ	Prediction horizon
χ_j	Fuel price of the DG unit connected to bus *j*
ω_c	DG unit low pass filter cut-off frequency
ω^{ub}, ω^{lb}	Upper and lower bounds on the allowable system frequency, respectively

Sets

B	Set of all system buses
$B^{(is)}$	Set of all buses in islanded microgrid *is*
B_{droop}	Set of all droop-controlled buses in the system
$B_{droop}^{(is)}$	Set of all droop-controlled buses in islanded microgrid *is*
C_0	Set of mandatory constraints in a given constraint hierarchy *C*
C_p	Set of preferred constraints of *p* preference level in a given constraint hierarchy *C*
$N_{st}^{G}, N_{st}^{L}, N_{st}$	Set of all possible generation, load, and combined generation-load states, respectively
Z_0	Set of all admissible solutions to a constraint hierarchy
Z_p	Set of all constraint hierarchy solutions that satisfy constraints up to and including level *p*

Variables

$D_{PEV}^{i}(t_k, vh)$	Charging decision of vehicle *vh* connected to bus *i* at time instant t_k
i_o	DG unit output current at the PCC
I_{ij}	Magnitude of the current flowing in the line between buses *i* and *j*
i_{L_f}, i_{C_f}	Current in DG unit output filter inductor and capacitor, respectively

m_{pi}, n_{qi}	Active and reactive power static droop gains for droop-controlled DG unit at bus *i*, respectively
P_{Gi}, Q_{Gi}	Generated active and reactive power at bus *i*, respectively
$P_{Gi,max}$, $Q_{Gi,max}$	Active and reactive power generation capacities at bus *i*, respectively
$P_{i,inj}$, $Q_{i,inj}$	Active and reactive power injected at bus *i*, respectively
P_{Li} ,Q_{Li}	Active and reactive load power at bus *i*, respectively
$P_{PEV}^{i}(t_k, vh)$	The consumed/delivered power by vehicle *vh* connected to bus *i* at time instant t_k
$\tilde{p}$, $\tilde{q}$	Instantaneous output active and reactive powers, respectively
$SOC^{i}(t_k, vh)$	SOC of vehicle *vh* connected to bus *i* at time instant t_k
V_i^*, ω_i^*	No-load output voltage magnitude and frequency of droop-controlled DG unit at bus *i*, respectively
$\|V_i\|$,δ_i	Voltage magnitude and angle at bus *i*, respectively
v_i	Voltage at the terminal of the DG unit inverter
v_{L_f}	Voltage across DG unit output filter inductor
v_o	Voltage across DG unit output filter capacitor
$\Delta V_i^{(is,st)}$	Binary variable indicating the voltage regulation status of load point *i* when operating in islanded microgrid *is* at state *st*
z	Solution of constraint hierarchy
Z_{ij}^{abc}	Three phase frequency dependent impedance of the feeder connecting buses *i* and *j*
λ	Loading factor of islanded microgrid
ω	Steady-state frequency of droop-controlled DG units output voltages

Chapter 1
Introduction

1.1 Motivation

Driven by the urgent need to develop cleaner and more efficient, reliable, resilient, and responsive power grids, the energy sector is currently moving towards an era of smart grids [1], [2], [3]. From a functionality perspective, the smart grid technologies aim to deliver better system performance and to enable a wide spectrum of additional services and benefits to both customers and utilities. The main features of such smart grid setup are; 1) transforming the electrical power system from the centralized paradigm to a deregulated paradigm, 2) increasing the system reliability and efficiency, 3) facilitating the interconnection between customers, network operators and electric power producers, and 4) promoting a high level of renewable generation [4], [5].

In electric distribution systems the smart grid setup is based on the evolution of the passive network structure characterized by its unidirectional power flow into an active distribution system (ADS) characterized by high distributed generation (DG) penetration along with multi-direction power flow [6], [7]. As the number of DG units increases electrical regions with sufficient generation to meet all or most of its local loads can be formed within the ADS; these regions are known as microgrids [8], [9]. The IEEE Std. 1547.4 presents the microgrid structure as the building block of future ADSs [10]. Additional features of microgrid systems are defined as; 1) capable of operating in parallel with the main grid (i.e. grid-connected mode), as well as in isolation from the main grid (i.e. autonomous or islanded mode), and 2) intentionally planned. The connection between a microgrid and the main grid does not necessarily have to be active all the time. For instance, this connection might be normally open and only closes in particular situations such as an internal outage inside the microgrid or when it is convenient to sell electricity to the main grid.

The idea supporting the formation of microgrids is that a paradigm consisting of multiple DG units and aggregated loads is far more reliable, economical and practical than a single DG unit serving a single load [8], [10]. The implementation of the microgrid concept can bring multiple benefits to both the consumers and distribution utilities. Examples of such benefits include:

1- Reliability increase: the capability of the microgrid to operate independently of the main grid allows the microgrid to feed its loads autonomously when the main grid is not available and thus avoid possible load interruptions [11], [12].

2- Grid support: by clustering loads and DG units and treating each of these clusters as a relatively independent power unit, microgrids can be used to supply electrical services to the main grid especially at the times of grid peak demand. Examples of such services include ancillary services, spinning reserve, voltage support, etc. [13].

3- Local community support: with the increasing efficiencies of the DG units, microgrids can support local and developing communities' economies by creating jobs within such communities to generate the required electricity instead of importing it from the main grid. The implementation of microgrids can also expedite the development of such communities instead of waiting for the power companies to build centralized power plants that are costly and take much longer to come online [14].

4- Reducing the carbon footprint: the microgrid concept can reduce the environmental impacts associated with the construction of large power plants to cope with the electrical load growth by allowing more dependence on small efficient DG units. Moreover, microgrids can largely facilitate the implementation of the combined heat and power (CHP) plants [15].

The IEEE standard 1547.4 enumerates a list of potential benefits for the islanded microgrid operation. Such benefits include:

1- Improving the microgrid customers' reliability by supplying the islanded portion during an upstream outage or disturbance.

2- Relieving electric power system overloading issues by allowing microgrids to be intentionally islanded.

3- Resolving power quality issues by isolating the microgrid from its upstream network in power quality events such as voltage distortion, voltage sag and flicker.

4- Allowing for maintenance of the power system components without interrupting customers' power supply.

These benefits motivate the operation of microgrid systems in the islanded mode. However the operation of the islanded microgrid systems faces several challenges that need to be overcome in order to allow for such potential benefits; important among these challenges are:

1- There is a lack of an accurate steady-state analysis tool for islanded microgrid systems. The practical implementation of the islanded microgrid concept by the distribution utilities requires different operational studies. The first requirement for any stability, planning, control, protection, or management study is the availability of an accurate power flow analysis tool. Despite the fact

that power flow analysis is a mature subject, the traditional power flow tools found in the literature are generally not suitable for the islanded microgrid operating mode. The reason is that none of these tools reflect the islanded microgrid special philosophy of operation, where the islanded microgrid is operated in isolation from the main grid and is fed from a group of small DG units of comparable sizes.

2- There is a need to maximize the possible utilization of the islanded microgrid limited generation capacities while meeting the system operational requirements. Maximum loadability is of particular importance in the case of islanded microgrids as the system active and reactive demands are fed from an isolated group of small DG units of limited capacities. The operational characteristics of the different DG units in the island can significantly affect the overall system loadability. Hence, the incorporation of a criterion for assessing and maximizing the system loadability in the islanded microgrid optimal power flow (OPF) problem is crucial for the successful implementation of the islanded microgrid concept. Such incorporation should account for an accurate representation of the islanded microgrid special philosophy of operation in the absence of the utility bus.

3- There is a need for a decentralized operation scheme for islanded microgrid systems. Centralized operation schemes based on a communication infrastructure are possible. Yet, the operation of islanded microgrids without a central controller and its associated communication infrastructure is still the viable solution in a number of scenarios, the most critical of which occurs when the microgrid is intended to operate only in emergency conditions during inadvertent events in the upstream network. Without centralized controllers, islanded microgrid decentralized operation schemes need to predesigned offline to accommodate the variability associated with the output power of renewable DG units as well as the load variability. Moreover, such schemes should account for the different possible islanded microgrid configurations that can be initiated in a distribution system depending on the fault and the isolation device locations. In this context, the problem of designing an islanded microgrid decentralized operation scheme presents an unprecedented challenge in ensuring the satisfaction of the system operational constraints considering all the states in which the different possible islanded configurations may reside.

4- There is a need to mitigate the potential risks imposed to the islanded microgrid operation by the widespread vehicle electrification under the smart grid paradigm. The coordinated operation and control of islanded microgrid resources together with plug-in electric vehicles (PEVs) is central to the successful operation of islanded microgrid systems in the presence of high PEV penetration. However such coordination can be particularly complex as the PEVs charging/discharging schemes need to be coordinated across multiple time steps considering the islanded microgrid limited

generation resources along with the uncertainty and variability associated with the output power of renewable DG units, as well as the islanded microgrid load variability. Further, during inadequate generation periods, PEVs can interfere with the existing islanded microgrid load shedding schemes leading to either total system collapse or unnecessary load shedding, if they are not appropriately managed. Moreover, the PEVs charging behavior (i.e. residence time, arrival rate and driver preferences) is random and yet there is a lack of sufficient historical data to accurately model the PEVs charging behavior properly.

1.2 Research objectives

The ultimate goal of the work adopted in this thesis is to facilitate the wide spread implementation of the microgrid concept. Motivated by facing the islanded microgrid operational challenges, this research study focuses on developing new analysis and operational control algorithms for islanded microgrid systems. The specific objectives of this research are outlined as follows:

1- Developing a generalized three-phase power flow algorithm for microgrid systems operating in the islanded mode.

2- Developing accurate and detailed models for maximum loadability consideration in islanded microgrid OPF problems.

3- Developing an effective methodology to design decentralized operation schemes of islanded microgrids including renewable energy resources.

4- Developing an operational control scheme to enable the islanded microgrid seamless operation in the presence of high PEVs penetration.

1.3 Thesis layout

The remainder of this thesis is structured as follows:

Chapter 2 presents necessary background, state-of-the-art and a critical literature survey on islanded microgrids analysis and operational control.

Chapter 3 presents a novel algorithm for studying the power flow in three-phase islanded microgrid systems. The proposed algorithm adopts the real characteristics of islanded microgrid operation as well as the features of three-phase distribution systems. The problem is formulated as a set of nonlinear equations. A globally convergent Newton-trust region method is proposed to solve this set of nonlinear equations.

Chapter 4 presents different formulations for the incorporation of a maximum loadability criterion in islanded microgrid OPF problem. A fuzzy-based approach is then developed to determine the best compromise solution of the bi-objective OPF problem for loadability maximization and generation cost minimization.

Chapter 5 introduces a probabilistic methodology for the design of islanded microgrid decentralized operation schemes taking into consideration the special features and philosophy of operations of islanded microgrids combined with the probabilistic models of DG units and the load variability.

Chapter 6 presents the development of a centralized multi-stage control scheme for islanded microgrids with high penetration of PEVs. The proposed control scheme coordinate the operation of islanded microgrid resources with the charging/discharging decisions of PEVs in the island in order to minimize the amount of load shedding, maximize the PEVs customers' satisfaction and minimize the overall islanded microgrid cost of operation.

Chapter 7 presents the thesis summary, contributions, and directions for future work.

Chapter 2

Background and Literature Review

2.1 Introduction

In chapter 1, the motivations of the research work have been discussed and the research objectives are presented. In this chapter, first some background information and a literature survey pertaining to the islanded microgrid operational philosophy, implementation and dynamic stability are presented. Thereafter, the rest of the chapter is divided into three main folds to review and critique the state-of-the-art research in the area of islanded microgrid analysis and operational control. The first part is dedicated for reviewing the islanded microgrid steady-state modeling and analysis. The second part reviews the islanded microgrid optimal operation techniques. The third part presents the main challenges facing the islanded microgrid operation in light of the expected high penetration of PEVs in the distribution systems.

2.2 Islanded microgrid philosophy of operation

In the grid-connected mode of operation, the DG units in the microgrid are operated to supply a pre-specified amount of active and/or reactive power to fulfill a predetermined system requirement (e.g. peak shaving, exporting power to the main grid, etc.). The difference between the active and reactive power produced by the microgrid DG units and the microgrid total load demand are either supplied or absorbed by the main grid and thus the frequency and voltage regulation are maintained at the different microgrid buses. In such a way, the DG units in the microgrid can be controlled as either PV or PQ buses similar to the case of conventional power systems [16], [17]. In this case, the DG units' output voltage reference is often taken from the grid voltage sensing via a phase-locked-loop (PLL) circuit, while an inner current loop ensures that the DG unit acts as a current source fulfilling its required function.

On the other hand, in the autonomous mode of operation, the DG units within the microgrid cannot be controlled as PQ and PV buses due to the following reasons:

1- The concept of operating the different generation units in a conventional power system as PQ or PV buses depends on the existence of a slack bus capable of holding and stabilizing the system frequency at constant value by supplying the difference between the specified generation and the load. However, in the islanded microgrid all the DG units are of relatively small and comparable sizes and as such there is not one generation point that is capable of performing such a task.

2- In conventional power system with DG units working as PQ or PV, any increase in the system load is fed from the slack bus till the dispatch center increases the setting of the PQ or PV buses. However, in islanded microgrids this will not work as the system has no slack bus. Accordingly, the total power produced by different DG units in the microgrid must meet the total islanded microgrid load demands. As the microgrid load demand is time varying, and given that the system has no slack bus, the active and reactive power produced by the different DG units in the microgrid cannot be pre-specified and have to exhibit real-time response to match the microgrid demand.

3- The main grid voltage signal is not available to be used as a reference for the system voltage and frequency; i.e. the DG units do not have a reference system signal to control their generation, it is rather the DG units that control the system voltage and frequency. This in turn raises the need for a separate control measure to control the autonomous microgrid system voltage's magnitude and frequency, other than the control measure adopted to control the DG units' terminal voltages. If the DG units were to be connected to the microgrid, paralleled, without such a control measure and depending only on the control of the DG units' terminal voltages to pre-set values; large circulating currents will flow between these DG units due to the system components tolerances and due to any system configuration change [18].

The majority of DG in the microgrid units are interfaced via a power electronic converter system coupled with an output passive filter [19], [20]. Different techniques have been proposed in the literature to accommodate this type of DG interface with the aforementioned requirements/challenges. These techniques can be generally categorized into two main approaches: centralized control approach and decentralized control approach (also known as wireless control).

The centralized control approach, as its name implies, depends on having a central controller controlling the operation of all the DG units in the islanded microgrid. This approach includes two main categories: the master/slave control techniques and the current/power sharing control techniques. The master/slave control technique depends on designating the different DG units in the islanded microgrid into either master or slave units. Several types of the master/slave control technique have been proposed in the literature. The single master/slave control technique uses one of the DG units in the islanded microgrid as a master unit and all the other DG units as slave units. The master unit generates a sinusoidal voltage that is used as a reference signal by all the slave units. A central controller receives information about the islanded microgrid loads and sends generation commands to the slave units which operate in a current control mode (or PQ mode) to produce the required power [21], [22]. The auto-master-slave control technique automatically sets the DG unit with the highest rating as a master unit that derives the reference voltage signal, the other DG units in the islanded microgrid are operated as slaves [23]. The multi-master

control technique sets several DG units in the islanded microgrid as masters operating with predefined voltage output signal. Again, other DG units in the islanded microgrid operate as slave units [24]. On the other hand, the current/power sharing control techniques depends on measuring the total load current in the islanded microgrid and dividing it among the different DG units available in the islanded microgrid to calculate the average unit current. The output current of each DG unit is measured and compared with the calculated average current to generate the control signal for load sharing [25].

Given its single point of failure, the centralized control approach does not offer the required redundant operation. Further, having a single point of failure in the islanded system can counteract the positive reliability boost anticipated from the implementation of the islanded microgrid concept. Also, as the DG units forming the microgrid might be dispersed from one another; achieving high bandwidth communication to share the dynamic current and voltage signals among these DG units or between the different DG units and a central controller can be both expensive and impractical. Moreover, such a communication link will decrease the overall system modularity [20], [26].

As such, to overcome these limitations, the widely accepted trend in the literature/industry is to standardize the decentralized control approach [10], [27]. Moreover, a low bandwidth communication can be coupled with this decentralized approach to achieve other goals e.g. optimizing the system operation in real-time. The decentralized control approach depends on local controllers located at the different DG units in the islanded microgrid and uses the system frequency as a means of communication among these controllers. This approach is mainly based on the droop control technique first proposed in [28] to be used in an isolated UPS system. It operates by mimicking the behavior of conventional synchronous generators. In conventional isolated power systems, powered only by synchronous generators and not connected to an infinite bus, the system voltage and frequency as well as the appropriate load sharing among the different paralleled generators are controlled throughout the system by the intrinsic characteristic of the synchronous generators known as the static droop characteristics [29]. For a constant mechanical input to the synchronous generator, the frequency of the generator decrease, as the active power supplied increase. Similarly, as the reactive power supplied by the generator increase, the output voltage magnitude decrease. In droop control, the local controller of each DG unit emulates the characteristics of a synchronous generator by subtracting proportional parts of the output active and reactive powers from the frequency and magnitude of the output voltage of the DG unit, respectively i.e. hence implementing specific droop characteristics. This provides a degree of negative feedback that ensures that the different DG unit in the islanded microgrid will always stabilize at the required load sharing; for instance, if the power drawn from one DG unit increases; its voltage slows, its angle retards and so it supplies less power.

2.3 Droop control implementation

Figure 2.1 shows the static droop characteristics implemented by the DG unit controller to emulate synchronous generator characteristics. Equations (2.1) and (2.2) give the droop characteristics implemented by the droop controller:

$$\omega = \omega^* - m_p P_G \tag{2.1}$$

$$|V| = V^* - n_q Q_G \tag{2.2}$$

where $|V|$ and ω are the DG unit output voltage fundamental component magnitude and frequency, V^* and ω^* are the inverter output voltage fundamental components magnitude and frequency at no load, m_p and n_q are the static-droop gains, P_G and Q_G are the active and reactive power generation by the DG unit, respectively.

Figure 2.2 shows the block diagram of the power circuit as well as the control circuit of a DG unit operating in an islanded microgrid. This is the most typical arrangement for a DG unit operating with DG control in islanded microgrid and there is a trend towards its standardization [20], [27]. The power circuit consists of the DG source interfacing inverter and the output LC filter used to remove the switching harmonics produced by the inverter. The controller of each DG unit consists of three cascaded control loops. The outermost control loop is used to realize the power sharing between the different DG units in the microgrid. The power sharing control loop achieves the required power sharing functionality through generating the reference magnitude and frequency of the fundamental output voltage across the LC capacitor according to the droop characteristics given in equations (2.1) and (2.2). The middle and innermost control loop then ensure that this reference voltage waveform is realized. Specifically, the middle control loop is the voltage controller used to control the voltage across the LC filter capacitor by generating the reference signal of the LC filter inductor current. The inner most control loop is the current controller used to control the LC filter inductor current by generating the inverter reference output voltage i.e. the gating signals.

The use and design of the innermost and middle control loops can be understood further by investigating the operation of an inverter connected to an LC filter. In such a system, there are two energy storage elements (the LC filter's capacitor and inductor). Accordingly, if we try to control the output voltage across the capacitor directly we will end up with a second order system. So, in order to guarantee a stable operation of the system under all conditions; we decouple the interactions between the capacitor and inductor by using two control loops; namely the voltage control loop and the current control loop. Each of these loops is accordingly dealing with a first order system and as such a stable operation can be ensured for all operating conditions.

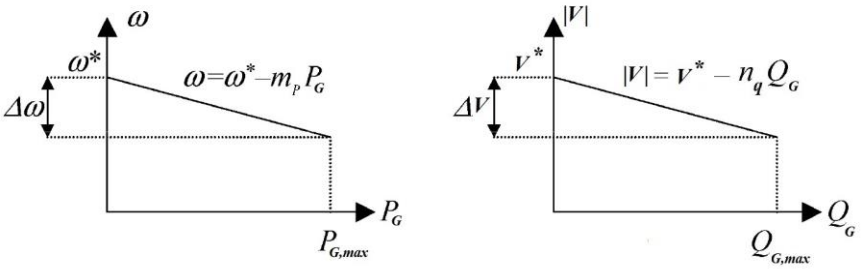

Figure 2.1: Static droop characteristics

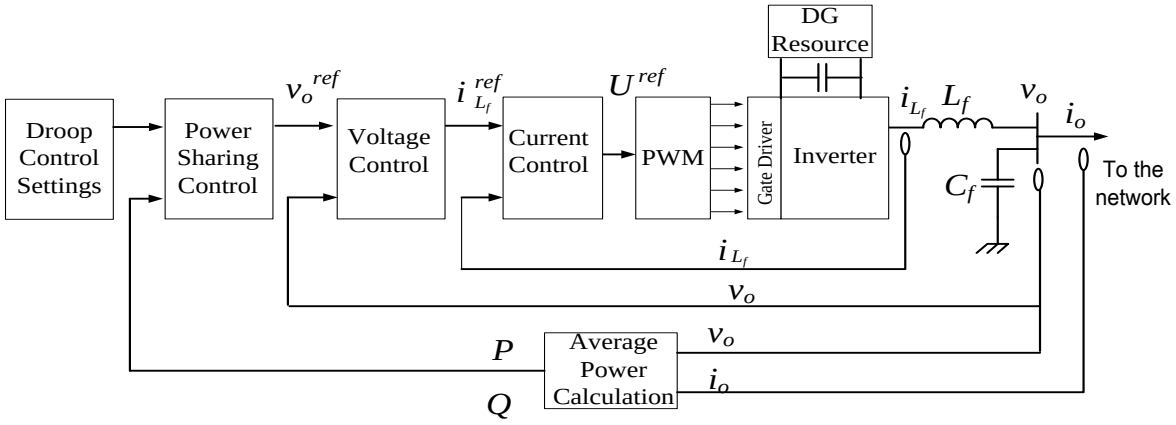

Figure 2.2: Power circuit and control structure of a DG unit operating in an islanded microgrid

To design the current control loop, we have to first determine the system transfer function. So, starting by the voltage across the filter inductor v_{L_f}

$$v_{L_f} = v_i - v_o = L_f . \frac{di_{L_f}}{dt} \tag{2.3}$$

The system transfer function can be written as

$$TF(s) = \frac{I_{L_f}(s)}{V_{L_f}(s)} = \frac{1}{L_f . s} \tag{2.4}$$

where the measured output voltage, v_o, is acting as a feed-forward signal and giving the system the ability to respond fast to any sudden change in the measured output voltage. As the transfer function is of first order, a proportional controller should have been enough to achieve the required closed loop control. However, because of the inverter's switches dead times, some noticeable non-linearities will appear in the current waveform and in the final output voltage waveform as well. Accordingly, a proportional integral controller is used to remove any steady state error. On the other hand, as the feedback signals are varying

with time, a PI controller will produce phase shifts on the feedback signals [30]. So in order to solve this problem; the time varying quantities are all transformed to a *d-q* reference frame rotating synchronously with the inverter output voltage angular speed ω, From which we can get

$$s.I_{L_{f\_d}}(s)=\frac{1}{L_f}\{[-\omega.L_f.I_{L_{f\_q}}(s)]+V_{i\_d}(s)-V_{o\_d}(s)\} \tag{2.5}$$

$$s.I_{L_{f\_q}}(s)=\frac{1}{L_f}\{[\omega.L_f.I_{L_{f\_d}}(s)]+V_{i\_q}(s)-V_{o\_q}(s)\} \tag{2.6}$$

Accordingly, the closed current control loop for the *d*-component, based on equation (2.5), can be depicted as shown in figure 2.3. A similar loop can also be drawn for the *q*-component based on equation (2.6). The proportional and integral gains of the PI controller, K^{pi}, K^{ii}, can be determined with a good accuracy by using the transfer function representation of the system and neglecting the coupling and feed-forward terms [26], [31]. Accordingly, any of the classical control techniques can be used to design the PI controller for the current control loop to work on a specific bandwidth. The dynamics of the current controller can thus be given by

$$v_{o\_d}^{ref}=K^{pi}(i_{L_{f\_d}}^{ref}-i_{L_{f-d}})+K^{ii}\int(i_{L_{f\_d}}^{ref}-i_{L_{f-d}}).dt-\omega.L_f.i_{L_{f\_q}}+v_{o\_d} \tag{2.7}$$

$$v_{o\_q}^{ref}=K^{pi}(i_{L_{f\_q}}^{ref}-i_{L_{f-q}})+K^{ii}\int(i_{L_{f\_q}}^{ref}-i_{L_{f-q}}).dt+\omega.L_f.i_{L_{f\_d}}+v_{o\_q} \tag{2.8}$$

where the superscript *ref* stands for reference. The design of the voltage control loop can be accomplished in exactly the same way. Starting by the equation of the current in the filter capacitor

$$i_{C_f}=i_{L_f}-i_o=C_f.\frac{dv_o}{dt} \tag{2.9}$$

From which we can write the system transfer function as

$$TF(s)=\frac{V_o(s)}{I_{C_f}(s)}=\frac{1}{C_f.s} \tag{2.10}$$

Then transforming the system to the *d-q* frame, we will end up with the dynamic equations of the voltage controller as

$$i_{L_{f\_d}}^{ref}=K^{pv}(v_{o\_d}^{ref}-v_{o\_d})+K^{iv}\int(v_{o\_d}^{ref}-v_{o-d}).dt-\omega.C_f.v_{o\_q}+i_{o\_d} \tag{2.11}$$

$$i_{L_{f\_q}}^{ref}=K^{pv}(v_{o\_q}^{ref}-v_{o\_q})+K^{iv}\int(v_{o\_q}^{ref}-v_{o-q}).dt+\omega.C_f.v_{o\_d}+i_{o\_q} \tag{2.12}$$

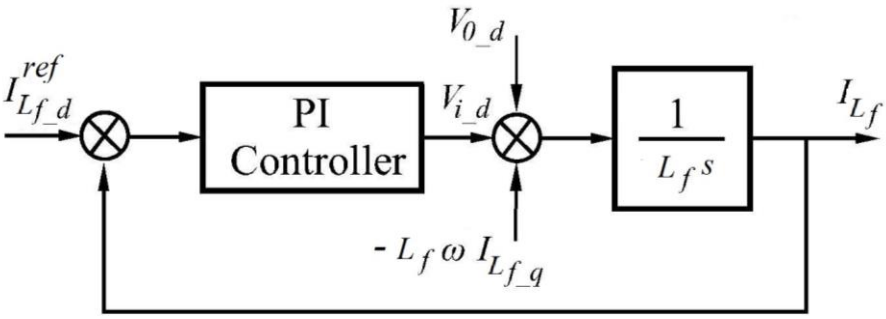

Figure 2.3: The *d*-component current control loop

Similar to the current controller, the proportional and integral gains of the PI controller, K^{pv}, K^{iv}, can be determined by using any of the classical control techniques considering the transfer function representation of the system and neglecting the coupling and feed-forward terms [31].

The power sharing control loop is used to obtain the reference voltage across the filter capacitor, v_o^{ref} . The instantaneous output active and reactive powers, $\tilde{p}$, $\tilde{q}$, are calculated

$$\tilde{p} = \frac{3}{2}\left(v_{o\_d}.i_{o\_d} + v_{o\_q}.i_{o\_q}\right) \tag{2.13}$$

$$\tilde{q} = \frac{3}{2}\left(v_{o\_d}.i_{o\_q} - v_{o\_q}.i_{o\_d}\right) \tag{2.14}$$

These instantaneous components are then passed through two low pass filters with a cut off frequency, ω_c, to obtain active and reactive power output of the DG unit corresponding to the fundamental component, P_G, Q_G.

$$P = \frac{\omega_c}{s+\omega_c}\tilde{p} \tag{2.15}$$

$$Q = \frac{\omega_c}{s+\omega_c}\tilde{q} \tag{2.16}$$

These average powers are then used in equations (2.1) and (2.2) to obtain the desired reference output voltage magnitude and frequency.

As the controller contains three cascaded control loops, the middle loop should be designed with a bandwidth at least 3-5 times slower than the innermost control loop in order to ensure a stable operation [26]. Also, the outermost control loop should be designed with a bandwidth at least 3-5 times slower than the middle control loop. The inner most control loop bandwidth is usually determined by the inverter switching frequency limitations due to the losses. Furthermore, a factor of 3 between the current control

loop bandwidth and the inverter switching frequency allows for good resolution and to mitigate the effects of the innermost and middle control loops on the system dynamic performance. The outermost control loop bandwidth is limited to the low pass filter cut-off frequency. Also, the LC filter is designed to have its cut-off frequency one decade below the switching frequency.

2.4 Islanded microgrid dynamic stability

In order to study the dynamic stability of the islanded microgrid system, a mathematical model of the system is needed. In reference [32] a single-phase inverter (DG unit) connected to the grid through an LC filter is modeled in order to study its small signal stability. The inverter output voltage is controlled to implement the conventional droop characteristics given by equations (2.1) and (2.2). The effects of the low pass filter used to measure the active and reactive power output of the inverter are incorporated in the model. By assuming that the grid voltage is stiff enough and is not affected by the output voltage of the inverters; a homogeneous equation describing the free motion of the system for a small disturbance around the equilibrium point is derived. Later in [33] the same authors of [32] developed their model further to model a small microgrid comprising two inverters connected in parallel. The main difference in [33] is that the system is isolated from the grid. Accordingly, unlike [32] the point of common coupling (PCC) of the DG units cannot be assumed to have a constant voltage magnitude i.e.; a stiff voltage. A state space model for each of the DG units is developed in a common *d-q* frame. The individual inverters state space models are then combined together to form the overall microgrid state space model using the network admittance matrix. The main disadvantages of this work are 1) it did not consider the inverter's voltage and current control dynamics in the model, and 2) it did not consider the network dynamics.

The work in [34] presented a control structure and a modeling procedure for the DG's operating in the microgrid. Driven by the significant impacts that voltage and current control loops can have on the dynamic stability of autonomous microgrids; especially when the closed loop bandwidth of the inverter's inner controls are close to the power sharing controller bandwidth for the case of higher power inverters. The work in [34] presented a detailed modeling procedure that takes into account the inverter inner controls' dynamics. However, the main drawback of this work is that it did not consider the network dynamics in the microgrid model. In conventional power system small-signal analysis neglecting the network dynamics and representing the network by its admittance matrix is justified by the fact that the network's time constant is negligible when compared to the synchronous generation time constants. Nonetheless, this assumption does not hold in the islanded microgrid case as most of the DG units are interfaced through power electronic converters and thus exhibit fast dynamic and control response.

To overcome the above mentioned disadvantages; the work in [20] presented a modeling and analysis technique for inverter-based microgrids that considers both the inverter inner control loops dynamics as well as the network dynamics. This technique is based on dividing the microgrid into sub-modules. Each inverter in the system represents a sub-module and is modeled on its individual reference frame whose frequency of rotation is set by its local power sharing controller. An arbitrary choice is made to select one of the inverter's frames as the system common reference frame and all the other inverters models are transformed to this frame. The network and loads are modeled on the common reference frame as separate sub-modules. A complete state-space small-signal model of the microgrid is the obtained by combining the state-space models of the different sub-modules in the microgrid.

The eigenvalue analysis of the islanded microgrid small-signal state-space models developed in [20] shows that there is a trade-off between the requirements of accurate power sharing from one side and the small signal stability from the other side. In droop control, a high value droop coefficient is required for accurate power sharing, while a small droop coefficient is required for good damping [26], [35]. Moreover, the droop method can exhibits slow dynamic response, since it requires low pass filter with low bandwidth to measure the active and reactive output power of the DG units in the microgrid.

The work in [35] proposed the decoupling of the system dynamic and steady-state responses by introducing power derivative and integral terms along with the conventional proportional droop terms given in equations (2.1) and (2.2). The added supplemental dynamic droop characteristics improve the system dynamic performance without affecting its steady state performance, as both the derivative and integral terms vanishes at steady-state. Accordingly, this creates a possibility of improving the system stability (i.e. dynamic response) without the loss of power sharing accuracy (i.e. or more generally without affecting the steady-state response). Reference [26] proposed the use of adaptive gains for the derivative and integral terms to guarantee the system dynamic stability along the system loading trajectory without affecting its steady-state response. Starting with a prespecified set of static-droop gains to implement a particular steady-state response, the coefficients of the adaptive dynamic droop gain are scheduled along the loading trajectory of each DG unit by means of a simple pole placement technique [26]. Accordingly, the work in [35], [26] shows that the dynamic operation of droop controlled islanded microgrid systems can be studied and improved separately from its steady state response; similar results have been obtained in other works [27], [36].

2.5 Islanded microgrid steady-state analysis

In order to ensure a successful practical implementation of the microgrid concept, operational and planning studies must be done a priori by the distribution utilities. Such studies include (and are not limited to):

1- Volt/Var control and planning studies of islanded microgrids.

2- Reconfiguration and restoration studies of islanded microgrids.

3- Islanded microgrid planning studies.

4- Optimal allocation of DG units considering the islanded microgrid operation.

5- Steady state Voltage stability analysis of islanded microgrid.

6- Contingency analysis of islanded microgrids.

7- Small signal stability analysis of islanded microgrids.

8- Protection coordination studies for islanded microgrid systems.

A prerequisite for all the aforementioned studies is the availability of an accurate power flow analysis tool. On the other hand, the problem of power flow analysis in islanded microgrid systems has not been addressed sufficiently in the literature. Most of the studies performed on islanded microgrids uses a time-domain simulation tool (e.g. PSCAD/EMTP or SIMULINK**)** to get the steady state operating conditions of the islanded microgrid system (e.g. [31], [26], [20], [37]).

Time-domain simulation tools numerically solve the set of differential equations describing the system response at every sampling instant. As such using this tool to solve for the system steady state values (which are independent of time) is 1) computationally expensive, 2) difficult to implement, 3) time consuming and 4) limits the studies to small test systems. On the other hand, a power flow tool should only formulate and solve the set of nonlinear algebraic equations describing the islanded microgrid operation at the steady state operating point only. As such using a power flow tool to analyze the islanded microgrid operation would be computationally less expensive than solving a larger set of differential equations at different points of time until the system reaches the steady state (i.e. time domain simulation).

Only a handful of recent publications tackled the subject of power flow analysis in islanded microgrid systems. Reference [38] proposes a two-step power flow analysis technique for islanded microgrid systems. This technique accurately represents the power electronic interface of the DG units in the microgrid. Detailed steady-state fundamental-frequency models for 1) matrix converters and 2) voltage-

sourced *ac-dc-ac* converters used for interfacing DG units are formulated. Using these model the proposed power flow technique in [38] solves for the internal variables of each DG unit in the islanded microgrid. In its first step, this technique uses the conventional concepts of power flow analysis to solve the islanded microgrid system power flow problem. In its second step, this technique uses the electrical variables at the PCC of the different DG units as calculated in the first step to solve for the internal variables of the DG units.

The technique presented in [38] only considered the positive sequence component i.e. only considered balanced systems. To overcome this limitation, reference [39] presents another method, for power flow analysis in islanded microgrids, that accommodates single-phase loads as well as unbalanced loads and lines. This method is based on the use of sequence components for the solution of the power flow problem. Generalized sequence component frame models are formulated for 1) three-phase synchronous generator based DG unit, and 2) voltage source inverter interface DG unit. The formulated models accommodate both PQ and PV modes of operation of the different DG units. Through incorporating the developed DG units' models with the network sequence models, the power flow problem is solved for the positive, negative and zero sequence of the system. Finally, the phase voltages at the different system buses are extracted. In [40] the work presented in [39] is expanded to incorporate 1) a unified and generic three-phase, steady-state, fundamental frequency, sequence-frame-based model for a DG unit, 2) DG unit operational limits and constraints, e.g. maximum phase current, and 3) different operation strategies for the DG other than the PQ and PV e.g. current control. The main drawback of the work presented in [38] - [40] is that it do not reflect the operational characteristics of the islanded microgrid operating with decentralized droop control. It rather presents steady-state models for the different power electronics interfaces and coupled them with conventional power flow method.

The conventional power flow formulation is not applicable in most of the islanded microgrid operation cases as;

1- In the conventional power flow formulation, the representation of a DG unit as slack bus means that this DG unit is treated as an infinite bus capable of holding the system frequency and its local bus voltage constant. This representation does not reflect the microgrid configuration where an islanded microgrid system is typically fed from a group of DG units of small and comparable sizes and there is no one generation unit capable of performing the slack bus function. Furthermore, if we consider the DG units owners perspectives, it will be difficult to guarantee the availability of a DG unit that is willing to operate as a slack bus at the time of the microgrid islanding.

2- In conventional power flow formulation, the representation of the DG units as PV/PQ buses, assumes that the required active power generation and/or local voltage at each DG unit are pre-

specified. However, this representation does not reflect the reality of the decentralized droop control based microgrid operation, where both the generated active power and the local voltage at each DG unit are determined locally based on the droop characteristics and cannot be pre-specified prior to the solution of the power flow equations.

3- In conventional power flow formulation, the system steady state frequency is assumed to be constant. However in islanded microgrid systems, given that there is no slack bus, the steady state frequency is not pre-specified and needs to be calculated as one of the power flow variables.

Hence, this review of the literature shows that there is a lack of a power flow algorithm tool tailored for the islanded microgrid systems. Some of the previous islanded microgrid studies used a time-domain simulation tool to solve for the steady state values in the islanded microgrid. Nonetheless, this solution is computationally expensive and cannot be applied to large islanded microgrid system which in turn limits the islanded microgrid system studies to small systems. Other previously proposed methods for power flow in islanded microgrids focused on the calculation of the DG units' power electronic interface control parameters, and formulated the power flow problem in islanded microgrid as a conventional power flow problem. In these studies, the DG unit with the highest rating is usually selected as the system slack bus. Other DG units in the islanded microgrid are represented as either PV or PQ buses with a pre-specified or selected active voltage magnitude and/or power. As such these power flow problem formulations do not reflect the islanded microgrid special philosophy of operation under droop control. Accordingly, for studying the power flow in an islanded microgrid, there is a need for a new power flow algorithm.

2.6 Islanded microgrid optimal operation

Decentralized droop control depends on locally measured values to; 1) achieve appropriate sharing of the power demand among the different DG units in the islanded microgrid; and 2) control the islanded microgrid voltage and frequency. Generally, decentralized droop control can; 1) provide an adequate means of sharing the islanded microgrid active power demand among the different DG units in the island in proportion to the DG units' respective capacities, 2) maintain an acceptable system frequency, and 3) maintain an appropriate voltage regulation at the DG units' PCC. Nonetheless, the decentralized droop control does not consider the optimal operation in terms of minimizing the system generation costs [41], [42], [43], [44], [45]. Moreover, it can only ensure voltage regulation at the DG units PCC. Here it is worth noting that even if required voltage regulation is achieved at the DG units PCC, still a voltage violation might occur at some load points due to voltage drops along the feeders [46]. Furthermore, the appropriate reactive power sharing between the DG units is not achieved [46]. The reactive power generation of the different DG units depends on the system parameters. Circulating reactive power

between the different DG units in the microgrid can arise due to mismatches in the power line impedances.

Accordingly, to overcome the aforementioned limitations, the decentralized droop control scheme is usually complemented with a microgrid central controller (MGCC) [43], [44]. Using non-critical communication links, the MGCC periodically updates the droop settings (i.e. droop characteristics determined by ω^*, V^*, m_p and n_q) of the different DG units in the island. Periodic measurements of the islanded microgrid generation and loads are transmitted to the MGCC. The MGCC uses the received data to solve the islanded microgrid OPF problem and consequently update the DG units' droop characteristics in a way that dispatches the different DG units in the islanded microgrid to implement the desired OPF. The advantage of such schemes is that any failure in the MGCC or its associated communication links will not result in a failure of the islanded microgrid system; such failure will only imply lack of optimal operation and resorting back to decentralized droop control with no communication; using the droop settings in place at the moment of communication interruption. Compared to master/slave control schemes, the droop control schemes are found to be more economical and reliable as it minimize the communication bandwidth required and provide robust operation against any communication failure or delay. This multilevel control approach (i.e. a MGCC performing a supervisory control function to complement the DG units local droop controllers) is presented in the literature as the standard approach to endow islanded microgrid smartness and flexibility (e.g. [27], [43], [44]).

Different schemes have been proposed in the literature to optimize the islanded microgrid operation using a MGCC. In [41], [42] a MGCC is used to minimize the overall islanded microgrid fuel consumption. This scheme considers the DG units droop control as well as the presence of a CHP plant and a local heat demand in the microgrid. As such the optimization scheme implemented in the MGCC aimed at reducing the fuel consumption while constraining the islanded microgrid to supply both its electrical and thermal loads. The main drawbacks of the work presented in [41], [42] is that: 1) it did not consider the reactive power requirements and the network losses in the system optimization; 2) it did not consider the voltage and frequency operational constraints. Motivated by these drawbacks, the work in [43] presented a MGCC multistage optimization algorithm that minimizes the islanded microgrid fuel consumption. The proposed algorithm in [43] accounted for the islanded microgrid droop operation while considering the system losses, reactive power requirements and voltage and frequency operational constraints. Similarly in [44], [45] different algorithms are presented to minimize the islanded microgrids harmful gases emissions along with the system fuel consumption. In [47] an optimal VAR scheduling algorithm was proposed to be run by the MGCC, considering the DG units voltage droop control as well as the

uncertainty of wind farms. Similarly, another algorithm for proportional reactive power sharing was proposed in [48] .

This review of literature shows that considerable work has been done with respect to the islanded microgrid optimal operation. Yet, all the previous work fall short in two main aspects;

1- The consideration of system maximum loadability in the optimal operational planning of islanded microgrids. System maximum loadability is a key consideration in any power system operational problem (e.g. [49], [50], [51], [52]). System maximum loadability is related to the voltage collapse occurring as the system experience a qualitative change in the structure of its solutions due to small disturbances. Unlike conventional power system where the maximum loadability problem is merely dependent on the reactive power flow in the system [53], in islanded microgrids it can be shown that the maximum loadability is dependent on the droop control active and reactive power sharing [54], [55]. In this sense, maximum loadability problem is of particular importance in the case of islanded microgrids as the system is fed from a group of small DG units of limited capacities. Hence, it is important to maximize the distance of the operating point to voltage collapse during the operational planning of the islanded microgrid system in order to increase the system robustness against possible contingencies. In [56], [57] a continuation power flow algorithm based on a predictor-corrector scheme was developed to calculate the maximum loading factor of droop-controlled islanded microgrid systems. Nonetheless, the work in [56], [57] did not provide a method for optimally controlling the droop based islanded microgrid so as to maximize its loadability. To our best knowledge, the problem of optimally controlling the DG units in a droop controlled islanded microgrid in order to maximizes the island loadability has not been previously addressed in the literature. Hence, the problem regarding the operational planning of islanded microgrids still requires attention to incorporate the maximization the system loadability and thus allow islanded microgrid systems to operate at higher load demands.

2- The consideration of islanded microgrid optimal operation in the absence of the MGCC. The previously proposed methods in the literature, for enhancing the operation of droop-controlled islanded microgrids, presuppose the existence of a MGCC and a non-critical low bandwidth communication infrastructure to complement the droop control scheme. In this paradigm, the optimization of the islanded microgrid operation is performed centrally by a higher level coordinated management function at the MGCC. Yet, the operation of islanded microgrids without a MGCC is still the viable solution in different scenarios [58], [59]. The most salient of which is when the islanded microgrids are merely intended to operate in emergency conditions in their upstream networks; i.e. the events that might initiate the transition to islanded mode of operation

are unscheduled events [10]. The expected short time spans of such islanded microgrids operation might not motivate the installation of a MGCC and its associated communication infrastructure. In these scenarios, there will be no periodic update of the DG units droop characteristics. As such, the DG units droop characteristics have to be predesigned offline for a possible operational planning horizon within which the islanded microgrid operation might be initiated. Such design of the droop settings: i) should be capable of satisfying the system operational constraints in all operating conditions considering the uncertainty and variability associated with the output power of renewable DG as well as the load variability; ii) should take into consideration the different microgrid configurations that can be created within a typical distribution network, where the same droop characteristics of a DG unit must enable its operation in different possible islands; iii) should ensure the islanded microgrid capability to feed the maximum possible demand by enhancing the voltage instability proximity index taken over all the states in which the islanded system may reside. Accordingly, there is a need for an algorithm to optimally set the droop characteristics of the different DG units in a distribution network in the case of the unavailability of a MGCC.

2.7 Islanded microgrid operation with high penetration of PEVs

The vehicles electrification has been recently considered as one of the smart grid objectives. The widespread of PEVs will reduce fuel consumption and harmful gases emissions. However, without appropriate considerations, the charging process of PEVs can pose potential risks to electric distribution systems [60], [61]. The additional loads imposed by a high penetration of PEVs are expected to cause severe consequences such as increased power losses, power quality problems, transformer degradation, and fuse blowouts. Two control schemes of PEVs charging are proposed in the literature to address the PEV integration challenges. The first scheme involves uncoordinated PEVs charging, which is possible via either upgrading the distribution system infrastructure or deploying DG units to meet the excess power demand [62]. However, such planning alternatives reflect long-term horizons, and feasible solutions require consideration of multiple prospective factors, such as load growth and updated PEV models, which change rapidly due to the constant development of new technologies. Accordingly, the second scheme targets coordinated PEVs charging or charging/discharging that relies on the availability of two-ways communication infrastructure under the smart grid paradigm. Coordinated PEV charging/discharging schemes are known to be more beneficial to the customers and distribution network operators compared with the uncoordinated operation (e.g. [63], [64], [65], [66]).

Yet, the previous work in the literature gave full attention to conventional electric distribution networks operating in grid-connected mode and falls short in coordinating islanded microgrid operation in the

presence of PEVs. The coordinated operation and control of islanded microgrid resources together with PEVs is key for the successful implementation of the islanded microgrid concept under high penetration of PEVs. The integration of PEVs charging/discharging coordination schemes within the MGCC will allow the PEVs to play a pivotal role in the successful and optimized operation of the islanded microgrid systems. With proper integration, PEVs can behave as an electric shifting demand, peak clipping, and as a source of energy during inadequate generation in unscheduled events of islanded microgrid. Nonetheless, in islanded microgrid mode of operation, such integration can be particularly complex due to: i) the need to consider multiple time steps in the charging/discharging schemes, ii) the variability and uncertainty associated with the islanded microgrid demand and renewable resources coupled with its limited dispatchable generation resources, iii) the PEV charging/discharging scheme needs to be coordinated with the existing islanded microgrid load shedding algorithms to avoid unnecessary load shedding or possible total system collapse, and iv) the randomness in the PEVs charging behavior (i.e. residence time, arrival rate and driver preferences) accompanied by the lack of sufficient historical data to accurately model the PEVs charging behavior. Moreover, each vehicle has different battery characteristics, charging behavior, and charger ratings. Therefore, each individual vehicle in the system must be treated in a different way.

Recently, the authors in [67] proposed a 24-hours ahead dynamic OPF formulation to coordinate generation scheduling and PEVs charging in industrial microgrids for both grid-connected and islanded modes of operation. As the problem is solved for 24-hours ahead, the work in [67] assumed that the number of PEVs and their plug-in and preferred plug-out times are predetermined 24-hours ahead. Similarly, it is also assumed that the generated powers from photovoltaic units are perfectly forecasted for one day ahead. Such assumptions are not applicable as they will incorporate significant inaccuracies that might lead to islanded microgrid system collapse. A 24-hours ahead scheduling cannot account for the short term random behavior of PEVs charging and photovoltaic units generated power. Further, the work in [67] assumed that the islanded microgrid always have enough generation to fully charge all PEVs before their preferred plug-out times. However, this is not a typical scenario, where islanded microgrids might have a shortage of generation and a load shedding might be required. In consequence, considering PEV requirements as hard constraints might result in an infeasible optimization problem. Moreover, the work in [67] has formulated the OPF problem for the islanded microgrid as a conventional OPF problem. Hence, it did not account for the special features of droop-controlled islanded microgrid systems [68].

Accordingly, there is a need for a coordinated control scheme to manage the islanded microgrid operation in the presence of high PEV penetration in a way that improves the islanded microgrid operation during adequate and inadequate generation intervals. Such control scheme should account for the special

operational philosophy of droop-controlled islanded microgrid systems, and the stochastic nature of the islanded microgrid renewable power generation, and the random PEVs charging behavior.

2.8 Discussion

The critical review of literature presented in this chapter shows that some research work has been done to facilitate the implementation of the islanded microgrid concept. However, exiting literature fall short in addressing a number of key challenges. Firstly, there is a lack of a power flow algorithm tailored to accurately model the islanded microgrid special operation philosophy. Also the review shows that the islanded microgrid operational control schemes need to be revisited to consider the system maximum loadability as well as the islanded microgrid operation in the absence of a MGCC. Furthermore, a new control scheme is required to accommodate an anticipated high penetration level of PEVs in the islanded microgrids.

Chapter 3

Generalized Three-Phase Power Flow Algorithm for Islanded Microgrids

3.1 Introduction

In chapter 2, it was shown that a new formulation is required to provide a proper power flow analysis in islanded microgrids taking into consideration their special philosophy of operation where: 1) the power produced by the DG units in the islanded microgrid cannot be prespecified prior to the solution of the power flow equations and 2) the islanded microgrid system has no slack bus capable of maintain a constant system frequency, as such the islanded microgrid steady-state frequency is not prespecified and is one of the power flow variables. In this chapter, a novel and generic three-phase power flow algorithm is formulated for islanded microgrids. The proposed algorithm is novel since it adapts the real characteristics of the islanded microgrid operation; i.e., 1) Some of the DG units are controlled using the droop control methods; accordingly their generated active and reactive powers are dependent on the power flow variables and are governed by their droop characteristics; 2) The system frequency acts as a communication medium between the different DG units in the islanded microgrid and as such the steady-state system frequency is not pre-specified and is considered as one of the power flow variables; and 3) There is no slack bus in the system. The proposed algorithm is generic, where the features of distribution systems i.e. three-phase feeder models, unbalanced loads and load models are taken in consideration. Further, all possible operation modes of DG units (i.e., droop, PV or PQ) are considered in the formulated power flow algorithm. The problem is formulated as a set of nonlinear equations describing the power flow problem in both balanced and unbalanced islanded microgrid systems. A globally convergent Newton-trust region method is proposed to solve this set of nonlinear equations. The proposed power flow algorithm can be a powerful tool that helps the distribution network operator (DNO) to perform the steady analysis for islanded microgrids of considerably large dimensions with different DG operating modes. The remainder of this chapter is organized as follows: section 3.2 presents the islanded microgrid system components modeling. In section 3.3 the power flow problem formulation for islanded microgrid systems is presented. Section 3.4 provides the details of the Newton-trust region method adopted for the solution of the islanded microgrid power flow equations. In section 3.5 the proposed algorithm is validated based on comparison with exact time-domain solution, using the PSCAD/EMTDC platform. Numerical simulations with different case studies have been carried out in section 3.6 to test the effectives

and robustness of the proposed algorithm. Section 3.7 concludes this chapter and summarizes its main findings.

3.2 Islanded microgrid system modeling

3.2.1 Feeders modeling

In islanded microgrids the system frequency is a power flow variable. Therefore its variation should be taken into account in the line reactance model. In this work, Carson's equations of a three-phase grounded four-wire system are used. Carson's equations allow the computation of conductor self-impedance and the mutual impedance between any numbers of conductors above ground. Figure 3.1 shows a three-phase line section between bus *i* and *j*. A (4×4) matrix, which takes into account the self and mutual coupling terms, and the frequency variation can be expressed as shown in equation (3.1). For a well-grounded distribution system, the ground and the neutral potentials are assumed to be zero.

$$\left[Z_{ij}^{abcn}(\omega)\right]=\begin{bmatrix} Z_{ij}^{aa} & Z_{ij}^{ab} & Z_{ij}^{ac} & Z_{ij}^{an} \\ Z_{ij}^{ba} & Z_{ij}^{bb} & Z_{ij}^{bc} & Z_{ij}^{bn} \\ Z_{ij}^{ca} & Z_{ij}^{cb} & Z_{ij}^{cc} & Z_{ij}^{cn} \\ Z_{ij}^{na} & Z_{ij}^{nb} & Z_{ij}^{nc} & Z_{ij}^{nn} \end{bmatrix} \tag{3.1}$$

Kron's reduction [69] can be applied to (3.1), to get (3.2). The feeder model in (3.2) is designed to include the effects of the neutral or ground wire, incorporate the impact of the frequency variation and to be used in the unbalanced power flow calculations.

$$\left[Z_{ij}^{abc}(\omega)\right]=\begin{bmatrix} Z_{ij}^{aa-n} & Z_{ij}^{ab-n} & Z_{ij}^{ac-n} \\ Z_{ij}^{ba-n} & Z_{ij}^{bb-n} & Z_{ij}^{bc-n} \\ Z_{ij}^{ca-n} & Z_{ij}^{cb-n} & Z_{ij}^{cc-n} \end{bmatrix} \tag{3.2}$$

3.2.2 Load modeling

Behavior of loads can be modeled by representing the changes in their active and reactive power requirements due to changes in system voltages and frequency. The voltage dependency of load characteristics is represented by the static load models expressed as:

$$P_{Li} = P_{Loi} \, |V_i|^{K_{pv}} \tag{3.3}$$

$$Q_{Li} = Q_{Loi} \, |V_i|^{K_{qv}} \tag{3.4}$$

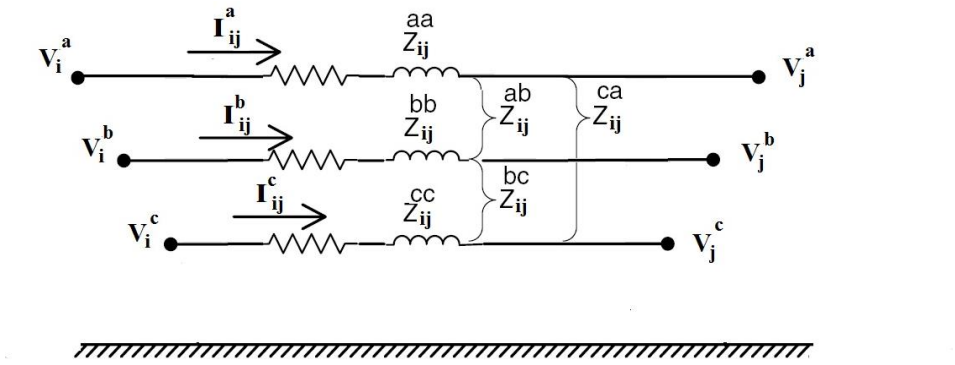

Figure 3.1: Three-phase feeder model

where, P_{oi} and Q_{oi} are the nominal active and reactive power operating points respectively; K_{pv} and K_{qv} are the active and reactive power voltage dependency exponents. In the constant power, constant current and constant impedance models, the active and reactive voltage dependency power exponents are equal to zeros, ones and twos, respectively. The values of the active and reactive power voltage dependency exponents for residential, industrial and commercial loads are given in [70]. The frequency dependency of load characteristics is represented by multiplying the voltage dependent static load model by a factor as follows:

$$P_{Li} = P_{oi} |V_i|^{K_{pv}} \left(1 + K_{pf} \Delta\omega\right) \tag{3.5}$$

$$Q_{Li} = Q_{oi} |V_i|^{K_{qv}} \left(1 + K_{qf} \Delta\omega\right) \tag{3.6}$$

where $\Delta\omega$ is the angular frequency deviation ($\omega - \omega_0$); K_{pf} ranges from 0 to 3.0, and K_{qf} ranges from -2.0 to 0 [71]. A load class mix of residential, industrial and commercial loads has been adopted in this work to generalize the proposed algorithm and take the impacts of load modeling in consideration.

3.2.3 DG modeling

In grid-connected microgrids, given the relatively small sizes of the DG units, they are controlled as PV or PQ buses. On the other hand, in islanded microgrids, the DG units are operated to achieve appropriate sharing of the load demands and to control the microgrid voltage magnitude and frequency levels. Given that there is no slack bus, it will be impossible to make all DG units operate in PV or PQ modes. Accordingly, in islanded microgrids, the DG units can operate in three modes of operation; i.e., PV, PQ and droop. For DG units operating in PV mode, the DG units inject pre-specified quantity of active power and the required reactive power to bring the bus voltage to a pre-specified voltage value. To take the DG reactive current limits in consideration, the calculated DG reactive power is compared with the minimum and maximum limits. If the calculated reactive power violates the upper or lower limits, the DG switch

from PV to PQ mode and the reactive power is kept at its limits. When the DG operates in PQ mode, the DG unit injects pre-specified quantities of active and reactive powers. Yet, the representation of DG units operating with droop control in power flow studies has not been previously tackled in the literature.

The majority of DG units are interfaced via a power electronic converter and an output filter [19], [20]. A review of possible converter interface arrangements, different control techniques and synchronization algorithms for DG units can be found in [21], [72], [73]. Figure 3.2 shows the proposed steady-state, fundamental frequency, power flow model of a DG unit operating in droop mode. As shown in the figure, the DG units operating in the droop mode, comprising the energy resource, the output filter and the power electronic converter, are modeled as an ideal voltage source whose voltage magnitude and frequency are determined using droop. This model is sufficient to calculate steady-state operating point for the electrical variables at the PCC of each DG unit operating in droop mode irrespective of the internal power circuit and the control structure used to implement such droop characteristics. For DG units operating in droop mode, the power electronic interface converter, the output filter, the energy resource and the control structure used to implement the droop characteristics at the PCC of the DG unit, do not affect the power flow solution. On the other hand, it is worth noting that detailed steady-state models of the different types of power electronic interface converters that can be used to calculate the different power electronic interface converters' internal variables have been previously presented in [38], [39]. Using the electrical variables at the PCC, calculated by the proposed power flow algorithm, the calculation of the DG units' power electronic converter internal variables can be performed as a second step. However, this calculation of the internal variables is not a point of concern in this work.

As discussed in chapter 2, in the droop mode of operation active power sharing is realized by introducing droop characteristics to the frequency of the DG unit output voltage at the PCC such that for the DG unit connected to bus *i*:

$$\omega = \omega_i^* - m_{pi} P_{Gi} \tag{3.7}$$

where ω is the DG output voltage frequency, ω_i^* is the no-load nominal frequency set point, m_p is the active power static droop gain, and P_{Gi} is the three-phase injected active power by the DG unit. From (3.7), it can be seen that the droop characteristic provide a measure of negative feedback that ensures that all the DG units are producing voltages with the same angular frequency at steady state i.e. system angular frequency [20].

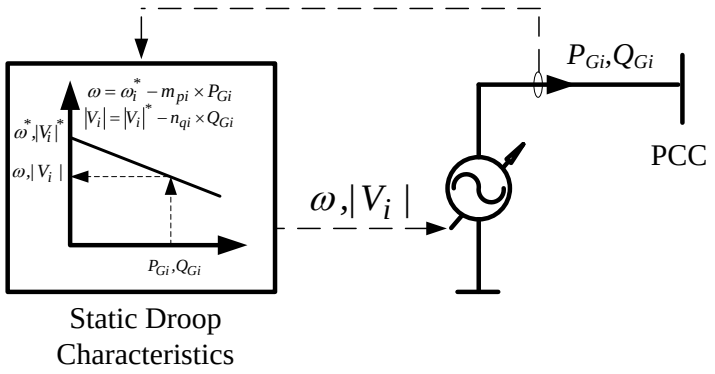

Figure 3.2: Steady-state, fundamental frequency model of a DG unit operating in droop mode

On the other hand, the reactive power sharing among the different DG units in the microgrid is achieved through the control of the DG output voltage magnitude. This control is accomplished in a *d*-*q* frame that rotates with the angular speed ω. A droop is introduced in the voltage magnitude of the DG unit output voltage at the PCC, such that

$$V_{di} = V_i^* - n_{qi} Q_{Gi}, \quad V_{qi} = 0 \tag{3.8}$$

where, V_{di} and V_{qi} are the *d*-axis and *q*-axis components of the DG output voltage at bus *i*, respectively, V_i^* stands for the no-load nominal output voltage set point, n_{qi} is the reactive power static droop gain, and Q_{Gi} is the injected three-phase reactive power by the DG unit. As per (3.8), the output voltage magnitude is aligned to the *d*-axis of the DG reference frame and the output voltage *q*-axis component is set to zero. As such for a DG unit connected to bus *i*; the three-phase output voltages can be given by the inverse Park transform as follows:

$$\begin{bmatrix} V_i^{(a)} \\ V_i^{(b)} \\ V_i^{(c)} \end{bmatrix} = \begin{bmatrix} V_{di}\cos(\omega t) \\ V_{di}\cos\left(\omega t - \frac{2\pi}{3}\right) \\ V_{di}\cos\left(\omega t + \frac{2\pi}{3}\right) \end{bmatrix} = \begin{bmatrix} |V_i|\cos(\omega t) \\ |V_i|\cos\left(\omega t - \frac{2\pi}{3}\right) \\ |V_i|\cos\left(\omega t + \frac{2\pi}{3}\right) \end{bmatrix} \tag{3.9}$$

The static droop gains for the DG unit connected to bus *i* (m_{pi}, n_{qi}) are conventionally calculated based on the allowable voltage and frequency regulation as well as the DG unit capacity [20], [26]

$$m_{pi} = \frac{\omega^{ub} - \omega^{lb}}{P_{Gi,max}}, \qquad n_{qi} = \frac{|V_i|^{ub} - |V_i|^{lb}}{Q_{Gi,max}} \tag{3.10}$$

where ω^{ub} and ω^{lb} are the upper and lower bounds on system frequency, $|V_i|^{ub}$ and $|V_i|^{lb}$ are the upper and lower bounds on allowable voltage magnitudes at bus *i*, $P_{Gi,max}$ and $Q_{Gi,max}$ are the maximum active and reactive power capability of the DG unit. The choice of the minimum and maximum allowable values of the frequency and voltage magnitude depend on the required voltage and frequency regulation [20].

In case of having DG units with different ratings, to achieve proper sharing in proportion to the DG units' ratings, the static droop gains are conventionally chosen as follows:

$$m_{p1} P_{G1,max} = m_{p2} P_{G2,max} = \cdots = m_{pi} P_{Gi,max}, \forall i \in B_{droop} \tag{3.11}$$

$$n_{q1} Q_{G1,max} = n_{q2} Q_{G2,max} = \cdots = n_{qi} Q_{Gi,max}, \forall i \in B_{droop} \tag{3.12}$$

where B_{droop} is the set of all droop controlled buses in the system.

Based on (3.7)-(3.9) the three-phase injected active and reactive power from a DG unit *i* operating with droop control can be expressed in the power flow formulation as follows:

$$P_{Gi} = \frac{1}{m_{pi}} \left(\omega_i^* - \omega \right) \tag{3.13}$$

$$Q_{Gi} = \frac{1}{n_{qi}} \left(V_i^* - |V_i| \right) \tag{3.14}$$

Typically the DG units are equipped with a current limiter to limit the production of the DG unit to its rated active and reactive capacities $P_{Gi,max}$ and $Q_{Gi,max}$. To take the DG current limits in consideration in the power flow formulation, the calculated DG active and reactive power generations are compared with their specified limits. If the calculated power violates its limits, the DG switches from droop-mode to PQ mode and the specified power is kept at the limit value.

In this work, the conventional droop equations expressed by (3.13) and (3.14) have been used in compliance with the IEEE standard 1547.4 for DG islanded systems. These characteristics are usually justified by assuming that the output impedance of the converter is mainly inductive due to the coupling inductor used at the converter output [20], [26], the large inductor of the output filter or by the use of virtual inductive output impedance [73]. However, it is worth noting that in some cases the output impedance of the converter is highly resistive due to: 1) the absence of the coupling inductor, 2) predominately resistive line impedances, or 3) the use of virtual resistive output impedance. In this case, the *P/Q* droops expressed by (3.13) and (3.14) exchange their roles and *P*-*V* and *Q*-ω droop characteristics are used [73], [74]. Furthermore, recently in [75], [76] it was shown that in several practical applications the converter output impedance can be complex. In such case the active and reactive

power sharing cannot be completely decoupled. Accordingly, a *P-V-ω* and *Q-V-ω* droop characteristics are used [75], [76] Such droop characteristics for either resistive or complex converter output impedances can be easily implemented in the proposed work hereafter by substituting (3.13) and (3.14) with the respective *P-V/Q-ω* or *P-V-ω/Q-V-ω* droop equations in the power flow formulation.

3.3 Problem formulation

This section presents the power flow problem formulation in the islanded microgrids. As shown in Figure 3.1, the relation between the branch voltages V_{ij} and branch currents I_{ij} between two nodes *i* and *j* can be expressed as follows:

$$\left[V_{ij}^{abc}\right] = \left[Z_{ij}^{abc}\right]\left[I_{ij}^{abc}\right] \tag{3.15}$$

where

$$\left[V_{ij}^{abc}\right] = \begin{bmatrix} V_i^{(a)} - V_j^{(a)} \\ V_i^{(b)} - V_j^{(b)} \\ V_i^{(c)} - V_j^{(c)} \end{bmatrix}, \left[I_{ij}^{abc}\right] = \begin{bmatrix} I_{ij}^{(a)} \\ I_{ij}^{(b)} \\ I_{ij}^{(c)} \end{bmatrix}$$

The branch currents can be obtained as a function of the branch voltages using

$$\left[I_{ij}^{abc}\right] = \left[Y_{ij}^{abc}\right]\left[V_{ij}^{abc}\right] \tag{3.16}$$

where $\left[Y_{ij}^{abc}\right]$ is the branch admittance matrix given as follows

$$\left[Y_{ij}^{abc}\right] = \left[Z_{ij}^{abc}\right]^{-1} = \begin{bmatrix} Y_{ij}^{aa-n} & Y_{ij}^{ab-n} & Y_{ij}^{ac-n} \\ Y_{ij}^{ba-n} & Y_{ij}^{bb-n} & Y_{ij}^{bc-n} \\ Y_{ij}^{ca-n} & Y_{ij}^{cb-n} & Y_{ij}^{cc-n} \end{bmatrix} \tag{3.17}$$

For each bus *i* the injected power in each of the three phases can be calculated as follows:

$$\left[S_{i,inj}^{(\phi)}\right] = \left[V_i^{(\phi)}\right]\left[I_{i,inj}^{(\phi)}\right]^{conj.} \qquad ,\forall \phi = a,b,c \tag{3.18}$$

where $\left[I_{i,inj}^{(\phi)}\right]^{conj.}$ is the complex conjugate of the injected currents at node *i* in phase ϕ. This injected current represents the sum of all the branch currents connected with bus *i*, therefore the injected current could be given by:

$$I_{i,inj}^{(\phi)} = \sum_{\substack{j=1 \\ j\neq i}}^{n_{bus}} I_{ij}^{(\phi)} \qquad ,\forall \phi = a,b,c \tag{3.19}$$

Let $P_{i,inj}^{(\phi)}$ and $Q_{i,inj}^{(\phi)}$ denote the calculated active and reactive power injected to the microgrid at each of the three phases at bus *i*. Substituting with (3.16) and (3.19) in (3.18), the calculated active and reactive power for phase *a*, $P_{i,inj}^{(a)}$ and $Q_{i,inj}^{(a)}$, can be given as in (3.20)-(3.21). Similar equations can be extracted for the calculated active and reactive power for phases *b* and *c*.

$$P_{i,inj}^{(a)} = \sum_{\substack{j=1 \\ j\neq i}}^{n_{bus}} \sum_{\phi=a,b,c} \left[\left|V_i^{(a)}\right| \left|Y_{ij}^{a(\phi)-n}\right| \left|V_i^{(\phi)}\right| cos\left(\theta_{ij}^{a(\phi)} + \delta_i^{(\phi)} - \delta_i^{(a)}\right) - \left|V_i^{(a)}\right| \left|Y_{ij}^{a(\phi)-n}\right| \left|V_j^{(\phi)}\right| cos\left(\theta_{ij}^{a(\phi)} + \delta_j^{(\phi)} - \delta_i^{(a)}\right) \right] \tag{3.20}$$

$$Q_{i,inj}^{(a)} = \sum_{\substack{j=1 \\ j\neq i}}^{n_{bus}} \sum_{\phi=a,b,c} \left[\left|V_i^{(a)}\right| \left|Y_{ij}^{a(\phi)-n}\right| \left|V_j^{(\phi)}\right| sin\left(\theta_{ij}^{a(\phi)} + \delta_j^{(\phi)} - \delta_i^{(a)}\right) - \left|V_i^{(a)}\right| \left|Y_{ij}^{a(\phi)-n}\right| \left|V_i^{(\phi)}\right| sin\left(\theta_{ij}^{a(\phi)} + \delta_i^{(\phi)} - \delta_i^{(a)}\right) \right] \tag{3.21}$$

where θ_{ij} is the bus admittance angle for branch *ij*, and δ_i is the voltage angle at bus *i*.

The system mismatch equations describing the power flow in the islanded microgrid is made up of n_{eq}-equations comprising the n_{eq}-unknown variables to be calculated. The voltage angle at bus#1 is taken as the system reference by setting $\delta_1^{(a)} = 0$. The number of mismatch equations describing each bus in the system depends on the type of the bus.

For each PQ-Bus, there are 6 mismatch equations; for PQ bus *i*, these mismatch equations are given as follows:

$$P_{Gi,spec}^{(\phi)} = P_{Li}^{(\phi)}(\omega, |V_i^{(\phi)}|) + P_{i,inj}^{(\phi)}(\omega, \left|V_i^{(a,b,c)}\right|, \left|V_j^{(a,b,c)}\right|, \delta_i^{(a,b,c)}, \delta_j^{(a,b,c)}) \tag{3.22}$$

$$Q_{Gi,spec}^{(\phi)} = Q_{Li}^{(\phi)}(\omega, |V_i^{(\phi)}|) + Q_{i,inj}^{(\phi)}(\omega, \left|V_i^{(a,b,c)}\right|, \left|V_j^{(a,b,c)}\right|, \delta_i^{(a,b,c)}, \delta_j^{(a,b,c)}) \tag{3.23}$$

$$, \forall \phi = a,b,c \text{ and } \forall j \in \{1,2,\ldots n_{bus}\}$$

where $P_{Gi,spec}^{(\phi)}$ and $Q_{Gi,spec}^{(\phi)}$ represent the pre-specified active and reactive generated power in phase ϕ. The corresponding unknown power flow variables for PQ bus *i* are given as:

$$x_{PQi} = \left[\delta_i^{(a,b,c)} \left|V_i^{(a,b,c)}\right| \right]^T \tag{3.24}$$

The corresponding unknown power flow variables for all PQ buses in the system can be given as:

$$x_{PQ} = \left[x_{PQ1} \ldots\ldots x_{PQn_{pq}} \right]^T \tag{3.25}$$

where n_{pq} is the number of PQ buses.

Each PV-Bus has 3 mismatch equations; for PV bus *i*, these mismatch equations are given as follows:

$$P_{Gi,spec}^{(\phi)} - P_{Li}^{(\phi)}(\omega, |V_{i,spec}^{(\phi)}|) = P_{i,inj}^{(\phi)}(\omega, \left|V_{i,spec}^{(a,b,c)}\right|, \left|V_{j}^{(a,b,c)}\right|, \delta_i^{(a,b,c)}, \delta_j^{(a,b,c)}) \tag{3.26}$$

$$, \forall \phi = a,b,c \text{ and } \forall j \in \{1,2,\ldots n_{bus}\}$$

where, $\left|V_i^{(\phi)}\right| = \left|V_{i,spec}^{(\phi)}\right|$

The corresponding unknown power flow variables for PV bus *i* are given as:

$$x_{PVi} = \left[\delta_i^{(a,b,c)}\right]^T \tag{3.27}$$

and the corresponding unknown power flow variables for all PV buses can be given as:

$$x_{PV} = \left[x_{PV1} \ldots\ldots x_{PVn_{pv}}\right]^T \tag{3.28}$$

where n_{pv} is the number of PV buses.

For each of the Droop-Buses, there are 12 mismatch equations; for droop bus *i*, these mismatch equations are given as follows:

$$0 = P_{Li}^{(\phi)}(\omega, |V_i^{(\phi)}|) - P_{Gi}^{(\phi)} + P_{i,inj}^{(\phi)}(\omega, \left|V_i^{(a,b,c)}\right|, \left|V_j^{(a,b,c)}\right|, \delta_i^{(a,b,c)}, \delta_j^{(a,b,c)}) \tag{3.29}$$

$$0 = Q_{Li}^{(\phi)}(\omega, |V_i^{(\phi)}|) - Q_{Gi}^{(\phi)} + Q_{i,inj}^{(\phi)}(\omega, \left|V_i^{(a,b,c)}\right|, \left|V_j^{(a,b,c)}\right|, \delta_i^{(a,b,c)}, \delta_j^{(a,b,c)}) \tag{3.30}$$

$$0 = \left|V_i^{(a)}\right| - \left|V_i^{(b)}\right| \tag{3.31}$$

$$0 = \left|V_i^{(a)}\right| - \left|V_i^{(c)}\right| \tag{3.32}$$

$$0 = \delta_i^{(a)} - \delta_i^{(b)} - (2\pi/3) \tag{3.33}$$

$$0 = \delta_i^{(a)} - \delta_i^{(c)} + (2\pi/3) \tag{3.34}$$

$$0 = P_{Gi}^{(a)} + P_{Gi}^{(b)} + P_{Gi}^{(c)} - P_{Gi}(\omega) \tag{3.35}$$

$$0 = Q_{Gi}^{(a)} + Q_{Gi}^{(b)} + Q_{Gi}^{(c)} - Q_{Gi}(|V_i^{(a,b,c)}|) \tag{3.36}$$

$$, \forall \phi = a,b,c \text{ and } \forall j \in \{1,2,\ldots n_{bus}\}$$

The corresponding unknown power flow variables for droop-bus *i* are given as:

$$x_{Di} = \left[\delta_i^{a,b,c} \; \left| V_i^{a,b,c} \right| \; P_{Gi}^{a,b,c} \; Q_{Gi}^{a,b,c} \right]^T \tag{3.37}$$

The corresponding unknown power flow variables for all droop-buses can be given as:

$$x_D = \left[x_{D1} \ldots\ldots x_{Dn_{droop}} \right]^T \tag{3.38}$$

As shown in the above equations, the total number of mismatch equations, n_{eq}, and their corresponding unknown power flow variables, X, in the islanded microgrids can be given as:

$$n_{eq} = 6 \times n_{pq} + 3 \times n_{pv} + 12 \times n_{droop} \tag{3.39}$$

$$X = \left[\omega \; x_{PQ} \; x_{PV} \; x_D \right]^T \tag{3.40}$$

3.4 Newton-trust region method

Traditionally the non-linear equations of the power flow problem are solved using the Newton Raphson (NR) algorithms. Generally, the NR algorithms provide fast quadratic convergence characteristics. However they face several challenges when dealing with distribution systems due to several factors such as the high R/X ratio as well as the sparse Jacobian matrix inversion [77], [78], [79], [80]. Further, in the case of islanded microgrids NR methods may fail to get a solution even with starting from a flat initial guess. Typically this situation is due to the fact that the region of attraction of the power flow solution in the islanded microgrid is narrow. Moreover, the system is operating close to the boundary between the solvable and unsolvable region as there is no infinite bus in the system. To tackle the demerits of the NR algorithms; this paper presents a Newton-trust region method as an alternative to the NR algorithms. Trust region methods are simple and powerful tools for solving systems of nonlinear equations and large scale optimization problems. Initially they were developed to solve unconstrained optimization problems. These methods behave like the NR algorithms featuring a quadratic convergence [81]. Furthermore, they have the advantages of guaranteeing a solution whenever it exists.

The set of nonlinear equations describing the power flow in an islanded microgrid is to be regarded as a minimization problem on the form of:

$$\min \begin{cases} F_1(X) = f_1(X) - A_1 = 0 \\ F_2(X) = f_2(X) - A_2 = 0 \\ \quad \vdots \\ F_{eq}(X) = f_{eq}(X) - A_{eq} = 0 \\ \quad \vdots \\ F_{n_{eq}}(X) = f_{n_{eq}}(X) - A_{n_{eq}} = 0 \end{cases} \tag{3.41}$$

$$subject\ to\ X \in \Re^n$$

Where $F_{eq}(X)$ $(eq=1,2,....,n_{eq})$ is the system of nonlinear functions described by (3.22) to (3.40), $f_{eq}(X)$ is the variable dependent term, A_{eq} is the constant term and n_{eq} is the number of unknown variables. The trust-region solution starts from an initial guess X_0 for the system variables vector X. For each succeeding iteration "*it*", a step Δ_{it} is calculated in an attempt to make $F_{eq}(X_{it}+\Delta_{it})$ smaller than $F_{eq}(X_{it})$. If this condition is achieved, the solution is updated from (X_{it}) to $(X_{it}+\Delta_{it})$. The step Δ_{it} is chosen to minimize a simpler quadratic model $\tilde{F}_{eq}|_{it}$ whose behavior around X_{it} is approximately the same as that of $F_{eq}(X_{it})$. This quadratic model can be defined by the second-order Taylor series of the original function F_{eq} around X_{it} [81], as follows

$$\tilde{F}_{eq}|_{it}(\Delta_{it}) = F_{eq}(X_{it}) + \Delta_{it}^T \nabla F_{eq}(X_{it}) + \frac{1}{2}\Delta_{it}^T \nabla^2 F_{eq}(X_{it})\Delta_{it} \tag{3.42}$$

where Δ_{it} is the increment of X_{it}, $\nabla F_{eq}(X_{it}) \in \Re^n$ is the gradient of F_{eq} at X_{it} and the $\nabla^2 F_{eq}(X_{it}) \in \Re^{n\times n}$ is the Hessian of F_{eq} at X_{it}. A region around the current iterate X_{it} is defined where we can trust the quadratic model to be an adequate representation of the original function F_{eq}. Accordingly, the trust region step can be defined as the step Δ_{it} which minimizes $\tilde{F}_{eq}|_{it}$ in a ball of radius r_{it} centered at X_{it} and a trust region sub-problem around X_{it} can be introduced as:

$$\begin{aligned} min. \quad & \tilde{F}_{eq}|_{it}(\Delta_{it}) \\ & subject\ to \|\Delta_{it}\| < r_{it} \end{aligned} \tag{3.43}$$

The trust region radius r_{it} is updated with each iteration according to the performance of the algorithm during the previous iterations. This update is based on the comparison ratio σ_{it} given by:

$$\sigma_{it} = \frac{F_{eq}(X_{it}) - F_{eq}(X_{it}+\Delta_{it})}{\tilde{F}_{eq}|_{it}(0) - \tilde{F}_{eq}|_{it}(\Delta_{it})} \tag{3.44}$$

If σ_{it} is small or negative (<0.01), this means that $\tilde{F}_{eq}|_{it}$ does not reflect the behavior of F_{eq} at X_{it}. In this case, this iteration is designated as a bad iteration; its results are rejected (i.e. $X_{it+1} = X_{it}$) and for the next iteration, the trust region radius r_{it} is decreased (i.e. $r_{it+1} = r_{it}/2$). If the quadratic model seems to be accurately approximating the original function, two cases are distinguished. If $\sigma_{it} \in [0.01, 0.9]$, the solution is updated with the computed step ($X_{it+1} = X_{it} + \Delta_{it}$) but the trust region radius is not modified (i.e. $r_{it+1} = r_{it}$). On the other hand, if $\sigma_{it} \geq 0.9$, the solution is updated ($X_{it+1} = X_{it} + \Delta_{it}$) and the trust region is increased ($r_{it+1} = 2 \times r_{it}$) [82].

The trust region algorithm has to solve the sub-problem defined by (3.43) at the beginning of each iteration to calculate Δ_{it}. It can be proved [83] that the solution of this constrained minimization satisfies

$$(\nabla^2 F_{eq}(X_{it}) + \Psi I)\Delta_{it}^* = -\nabla F_{eq}(X_{it}), \qquad \text{for some } \Psi \geq 0 \tag{3.45}$$

If r_{it} is big enough, the solution of the sub problem is the unconstrained minimizer given by

$$\Delta_{it}^* = -(\nabla^2 F_{eq}(X_{it}))^{-1} \nabla F_{eq}(X_{it}) \quad \& \quad \Psi = 0 \tag{3.46}$$

When $\Delta_{it}^* > r_{it}$, we define

$$\Delta_{it}(\psi) = -(\nabla^2 F_{eq}(X_{it}) + \psi I)^{-1} \nabla F_{eq}(X_{it}) \tag{3.47}$$

and seek a value for $\Psi > 0$ such the constraint $\|\Delta_{it}(\psi)\| < r_{it}$ is achieved. A number of algorithms have been proposed in the literature to achieve this [81], [82]. A very efficient and relatively simple method for doing so is the Dogleg method. The Dogleg algorithm solves the problem by approximating the function $\Delta_{it}(\Psi)$ with a piecewise linear polygon $\tilde{\Delta}(\tau)$ and solving $\|\tilde{\Delta}(\tau)\| = r_{it}$. The polygon $\tilde{\Delta}(\tau)$ is defined as

$$\tilde{\Delta}(\tau) = \begin{cases} \tau \Delta^U, & 0 \leq \tau \leq 1, \\ \Delta^U + (\tau - 1)(\Delta^* - \Delta^U), & 1 \leq \tau \leq 2, \end{cases} \tag{3.48}$$

Where Δ^U is the point that solves the quadratic model problem in (3.42); i.e., the Cauchy point [81].

Based on the above discussion, the Newton-Trust region method can be summarized in the following steps:

<u>*Step #1*</u>: Given X_0, $\varepsilon \geq 0$, $r_{it}|_{max} > 0$, $r_{it0} \in [0, r_{it}|_{max}]$, $it=0$

<u>*Step #2*</u>: if $F_{eq}(X_{it}) \leq \varepsilon$ then stop;

Solve (3.43) using Dogleg method (3.45-3.48) to get Δ_{it}

<u>*Step #3*</u>: Compute σ_{it}, eq. (3.44);

if $\sigma_{it} < 0.01$; $X_{it+1} = X_{it}$ & $r_{it+1} = r_{it}/2$

if $0.01 < \sigma_{it} < 0.9$; $X_{it+1} = X_{it} + \Delta_{it}$ & $r_{it+1} = r_{it}$

if $0.9 > \sigma_{it}$; $X_{it+1} = X_{it} + \Delta_{it}$ & $r_{it+1} = 2 \times r_{it}$

<u>*Step #4*</u>: *it=it+1*; Go to step *#2*

3.5 Algorithm validation

To validate the applicability of the novel power flow algorithm and demonstrate its accuracy, the results of the proposed algorithm are compared with the steady-state results obtained from a detailed time-domain model [20], [26] of an islanded microgrid. The balanced 6-bus test system shown in Figure 3.3 has been used in the algorithm validation. This system was chosen since it is adequately small and balanced so that in can be modeled in detail in a time-domain simulation tool such as the PSCAD/EMTDC. This system includes three identical droop-based DG units and represents an islanded microgrid. Data about the line impedances and system loads can be found in Appendix A. The proposed islanded microgrid power flow algorithm was developed in the MATLAB environment to solve the power flow problem of the 6-bus test system. A detailed time-domain simulation of the 6-bus test system was also performed in the PSCAD/EMTDC environment. The details of the time-domain model implemented in PSCAD are similar to those previously described in section 2.3 of this thesis. The results obtained from the proposed algorithm and from the detailed time-domain simulation are presented in Table 3.1. The results in Table 3.1 show that the maximum phase error is less than 0.5% and the maximum magnitude error is less than 0.05%. The good agreement between the results indicates the accuracy of the proposed power flow algorithm in solving the droop controlled islanded microgrid networks.

To show the limitation of the conventional power flow algorithms when it is applied to islanded microgrid with droop controlled DG units, a comparison between the results obtained by the proposed power flow algorithm and the results obtained from the conventional power flow algorithms that traditionally assign one DG unit as a slack bus and the other DG units as PV buses has been held. Two different case studies have been carried out on the test system shown in Figure 3.3. In the first case study, the test system has been solved using the proposed power flow algorithm that accurately model the DG units operating in droop mode. In the second case study, the test system has been solved using a conventional power flow method [84]; where DG unit # 1 is modeled as a slack bus and DG units # 2 and #3 are modeled as PV buses. In the second case study, several scenarios with different pre-specified settings of the generated active power of the PV buses are selected to be a percentage of the total islanded-microgrid loading.

Figure 3.4 shows the voltage profile of the 6-bus test system obtained from the two case studies. As shown in the figure, none of the different scenarios in the second case study coincide of the solution of the first case study. Given that the solution of the first case study coincide with the detailed time domain model, as shown in Table 3.1, the result in Figure 3.4 show that the conventional power flow algorithms cannot solve droop controlled islanded microgrids networks.

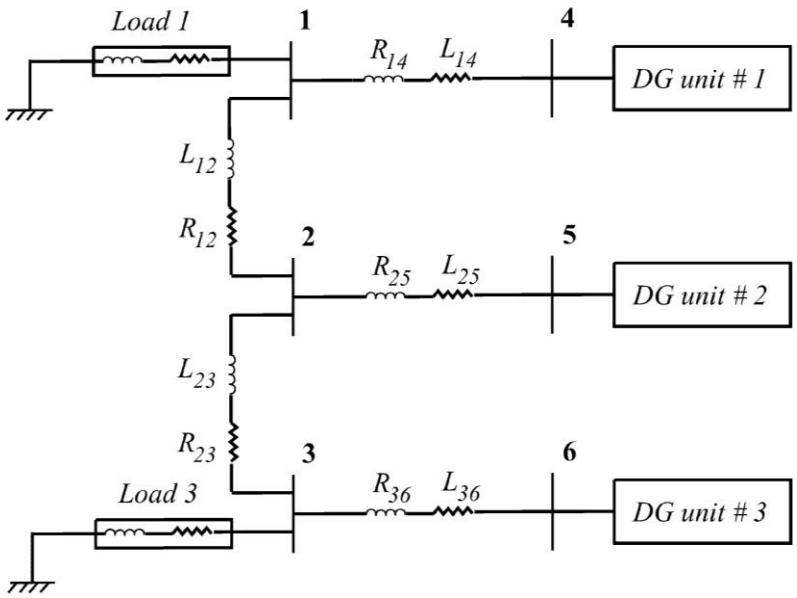

Figure 3.3: Single line diagram of the 6-bus microgrid test system

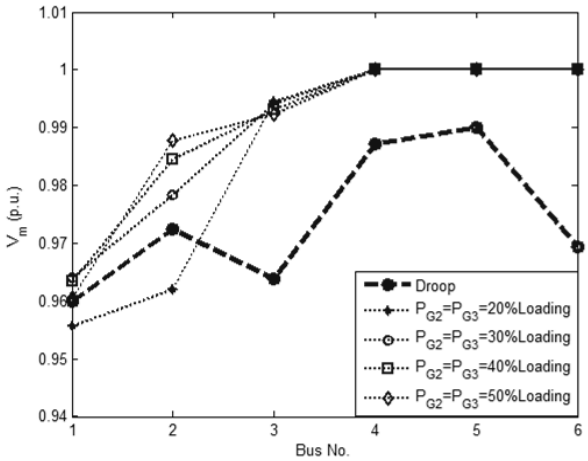

Figure 3.4: The voltage profile of the 6-bus test system using droop and conventional power flow algorithms

Table 3.1: Proposed power flow algorithm validation results of the 6-bus test system (V_{base}=127 V)

Node	PSCAD/EMTDC Results (Phase-A)		Power Flow Results (Phase-A)	
	Mag. (p.u.)	Ang. (degree)	Mag. (p.u.)	Ang. (degree)
1	0.9605	0.0000	0.9601	0.0000
2	0.9730	-0.5270	0.9725	-0.5262
3	0.9643	-2.6850	0.9638	-2.6822
4	0.9877	-0.0725	0.9873	-0.0722
5	0.9906	-0.4520	0.9901	-0.4510
6	0.9698	-2.8690	0.9694	-2.8653

These results also validate the limitations of the conventional power flow algorithms and the importance of the proposed method in solving islanded microgrid networks.

3.6 Case studies

In this section, a balanced and unbalanced radial distribution test systems have been chosen to test the effectiveness of the proposed algorithm. The proposed power flow algorithm was implemented in MATLAB environment. Several case studies have been carried out to illustrate the robustness of the algorithm and the effects of the different DG units' operation modes on the islanded microgrid operation. The algorithm shows good convergence in all operating conditions. The number of required iterations for convergence was under 5 iterations for all the study cases.

3.6.1 Balanced microgrid

Figure 3.5 shows the 38 bus balanced studied system [85]. The feeder parameters (at nominal frequency), load nominal power, type, and active and reactive power exponents are given in Appendix A. K_{pf} and K_{qf} are selected as 1 and -1 respectively [71]. As shown in Figure 3.5, five DG units have been placed in buses 34,35,36,37 and 38. Table 3.2 shows the DGs locations, static droop coefficients, nominal setting and ratings in the test system.

Case study# 3-1*:* When all DG units operate in droop mode

Table 3.3 shows the voltage profile, load and generation power in each bus and the total system losses in per unit when all DG units operate in droop mode with the parameters shown in table 3.2. The proposed algorithm has converged at steady-state frequency equals 0.9987 p.u. Even though this small deviation in the frequency does not impact the load characteristics much, such small frequency deviation is crucial in determining the active power sharing between the different DG units. Also, it is worth noting that this frequency deviation may increase significantly if the static droop gains are not properly designed. As shown in table 3.3, the sharing of active power among the DG units is divided among them based on the ratio of their ratings. Where, the generated active power from each DG unit depends on the system frequency. On the other side, the reactive power sharing among the DG units is not proportional to their ratings as proven in [86], [20].

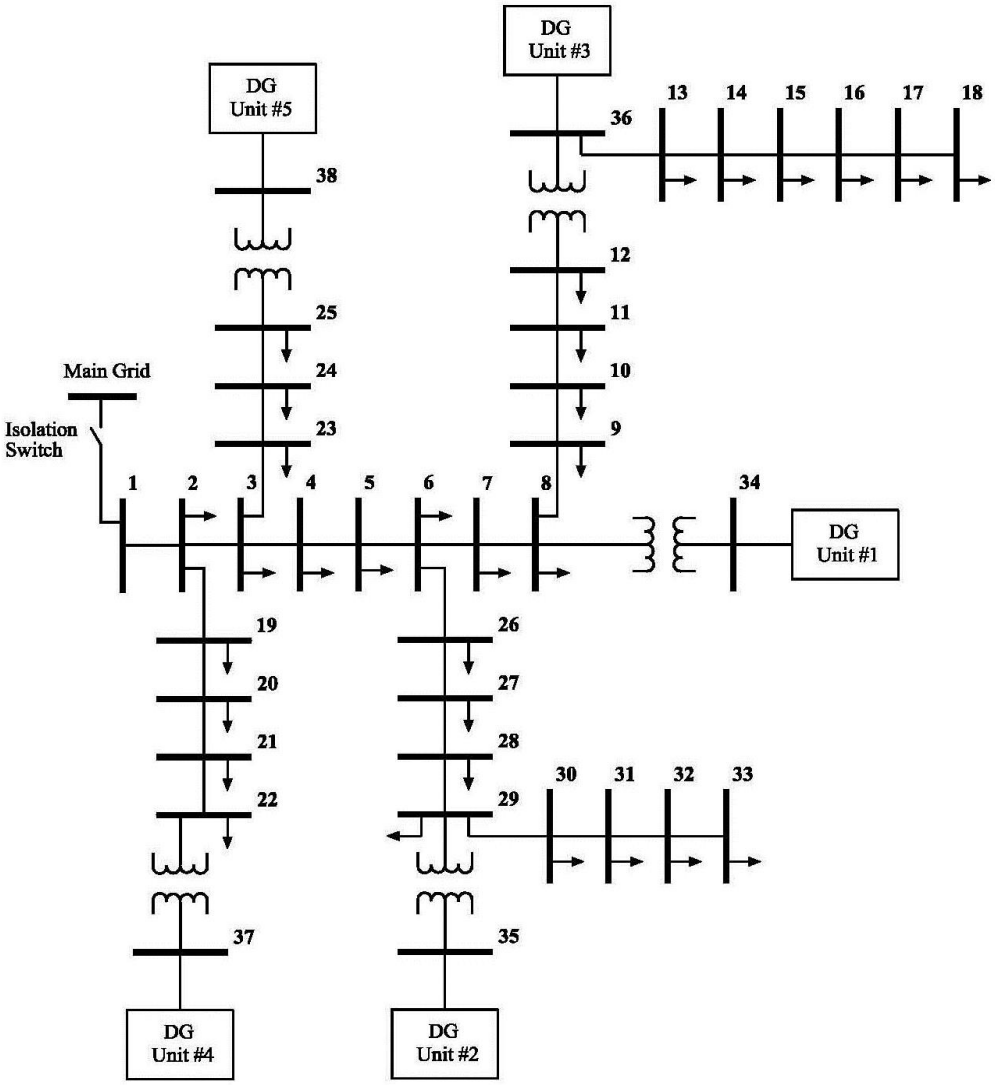

Figure 3.5: The 38-bus balanced microgrid test system

Table 3.2: DGs locations, static droop coefficients, nominal setting and ratings in 38 bus test system.

DG #	Location	m_p (p.u.)	n_q (p.u.)	ω^* (p.u.)	V^* (p.u.)	S_{gmax} (p.u.)	Q_{gmax} (p.u.)
1	34	0.751×10^{-3}	0.01667	1	1.01	3	1.8
2	35	1.501×10^{-3}	0.03333	1	1.01	1.5	0.9
3	36	4.504×10^{-3}	0.01000	1	1.01	0.5	0.3
4	37	2.252×10^{-3}	0.05000	1	1.01	1.0	0.6
5	38	4.504×10^{-3}	0.01000	1	1.01	0.5	0.3

Table 3.3: Case study# 3-1: load flow results of the proposed power flow algorithm in balanced microgrid

Node	Voltage (p.u., degree)		Load (p.u.)		Generation (p.u.)		Node	Voltage (p.u., degree)		Load (p.u.)		Generation (p.u.)	
	Mag.	Ang.	P_L	Q_L	P_G	Q_G		Mag.	Ang.	P_L	Q_L	P_G	Q_G
1	0.9563	0.0000	-	-	-	-	**20**	0.9641	-0.1484	0.085	0.035	-	-
2	0.9563	0.0000	0.096	0.501	-	-	**21**	0.9667	-0.1617	0.090	0.033	-	-
3	0.9560	-0.0197	0.089	0.031	-	-	**22**	0.9722	-0.1458	0.088	0.036	-	-
4	0.9576	-0.0014	0.112	0.069	-	-	**23**	0.9542	-0.0756	0.084	0.043	-	-
5	0.9596	0.0159	0.058	0.025	-	-	**24**	0.9510	-0.2012	0.389	0.169	-	-
6	0.9647	0.1365	0.060	0.016	-	-	**25**	0.9509	-0.2778	0.389	0.169	-	-
7	0.9672	0.3165	0.190	0.089	-	-	**26**	0.9645	0.1410	0.057	0.022	-	-
8	0.9728	0.2868	0.192	0.091	-	-	**27**	0.9644	0.1480	0.060	0.020	-	-
9	0.9704	0.1690	0.060	0.017	-	-	**28**	0.9645	0.1854	0.057	0.018	-	-
10	0.9658	0.0607	0.057	0.018	-	-	**29**	0.9649	0.2235	0.114	0.062	-	-
11	0.9682	0.0493	0.043	0.027	-	-	**30**	0.9617	0.3009	0.189	0.525	-	-
12	0.9678	0.0258	0.058	0.031	-	-	**31**	0.9580	0.2138	0.149	0.059	-	-
13	0.9624	-0.0697	0.057	0.031	-	-	**32**	0.9572	0.1909	0.208	0.084	-	-
14	0.9604	-0.1441	0.116	0.068	-	-	**33**	0.9569	0.1839	0.056	0.034	-	-
15	0.9591	-0.1808	0.056	0.009	-	-	**34**	1.0006	1.1047	-	-	1.681	0.563
16	0.9579	-0.2058	0.060	0.016	-	-	**35**	0.9850	0.2899	-	-	0.841	0.751
17	0.9562	-0.2792	0.056	0.017	-	-	**36**	0.9752	0.0105	-	-	0.280	0.300
18	0.9556	-0.2905	0.089	0.031	-	-	**37**	0.9759	-0.1534	-	-	0.560	0.600
19	0.9570	-0.0166	0.086	0.034	-	-	**38**	0.9529	-0.2818	-	-	0.280	0.300

Total	P_L	Q_L	P_G	Q_G	P_{Loss}	Q_{Loss}
	3.549	**2.426**	**3.642**	**2.514**	**0.093**	**0.088**

Case study# 3-2: Mix of Operation

Figures 3.6 and 3.7 show the voltage profile along the 38 buses and the generated reactive power when DG #1 operates in PV mode and injects $P_{G3,spec}$ = 1.681 p.u. with different settings of its local voltage, DG #5 operates in PQ mode and injects $P_{G5,spec}$=0.4 p.u. and $Q_{G5,spec}$=0.3 p.u. into the microgrid. The rest of the DG units operate in droop control mode. As shown in the figures, when the PV bus control its voltage at 0.98 p.u., all droop control DG units reach their Q_{gmax} trying to keep the voltages within the specified limits, however, under-voltages occur at most of the system buses. When the PV bus (DG #1) is required to control its voltage at 1.02 p.u., it injects large amount of reactive power. Therefore, the droop control DG units are still operating in the region of droop characteristics without reaching Q_{gmax}; i.e., given that the larger portion of the system reactive power requirement is supplied by DG #1, the other DG units (DG #2, 3 and 4) do not reach their maximum reactive power capacity. The figures also show that a proper setting of the voltage at the PV bus is required to guarantee appropriate reactive power sharing

between the PV bus and the droop DG units and to keep the voltages within the specified limits and avoid under-voltages.

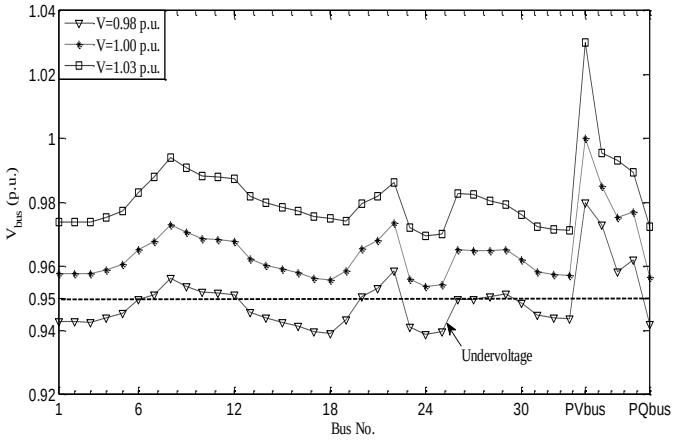

Figure 3.6: Case study# 3-2: voltage profile when DG #5 is working in PQ mode and DG #1 is working in PV mode

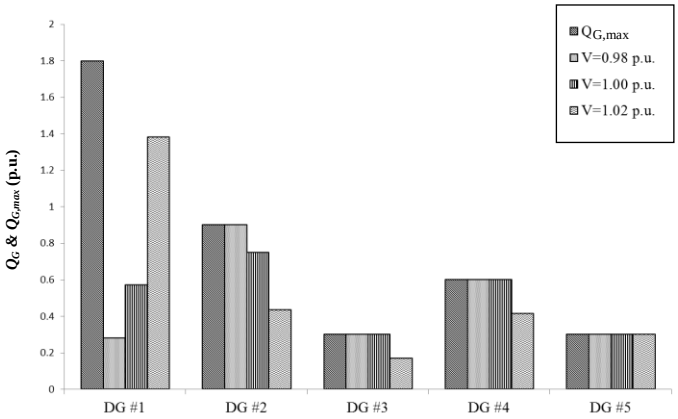

Figure 3.7: Case study# 3-2: Q_G and $Q_{G,max}$ of the different DG when DG #5 is working in PQ mode and DG #1 is working in PV mode at different settings of V

3.6.2 Case study# 3-3: unbalanced microgrid

A 25 bus unbalanced test system [87] is used in this case study. The system single line diagram, feeder parameters (at nominal frequency) and phase load power are given in Appendix A. Three DG units have been placed at buses 13, 19 and 25 respectively, to feed the system in the islanded mode of operation. To show the effectiveness of the proposed algorithm, the system load data in [87] have been modified in this work to increase the system unbalance by 20%. Table 3.4 shows the locations, static droop coefficients, nominal setting and ratings of these DG units in the 25 bus unbalanced test system. The proposed power flow algorithm has been converged at steady-state frequency equals 0.9980 p.u. Table 3.5 shows the

active and reactive power in each phase and the total injected power from each DG in p.u. Table 3.6 shows the power flow results (voltage profile and loads in each phase and the total system losses) of the proposed algorithm when all DG units in Table 3.4 operate in droop control mode. As shown in Table 3.6, the three-phase voltages at the locations of the DG units are equals in magnitude and they have 120^o phase shift (balanced). These results are matched with the capability of both converter and synchronous based DG units to generate balanced voltages on their points of connection. Table 3.5 shows that the total active power generations of the three DG units are shared appropriately based on the ratio of their ratings, even though there is no equal sharing between the generated active powers in each phase. Also, the results in Table 3.5 show that both DG #1 and DG #2 reach their $Q_{G,max}$ and only one DG operates in droop control. The results in Table 3.5 demonstrate that the total reactive power produced by each of three DG units is not proportional to its rated capacity; e.g. DG units #1 and #3 have equal capacity but are producing different $Q_{G\text{-}tot}$.

In Figure 3.8 the fast convergence characteristics of the proposed power flow algorithm is shown by plotting the maximum mismatch at each iteration versus the iteration number for the two systems under study in case studies # 3-1 and #3-3.

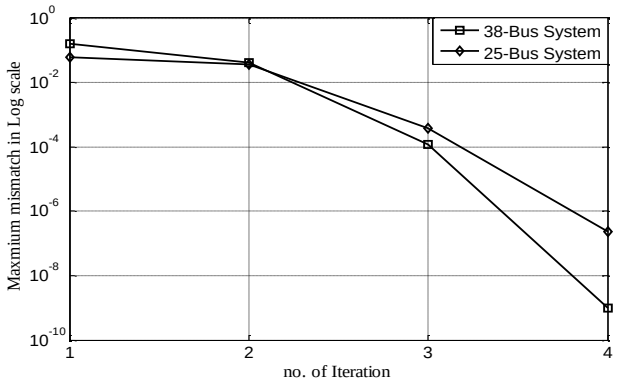

Figure 3.8: Maximum mismatch versus number of iteration in case studies # 3-1 and # 3-3

Table 3.4: Case study# 3-3: DG units' locations, static droop coefficients, nominal setting and ratings

DG #	Location	m_p (p.u.)	n_q (p.u.)	ω^* (p.u.)	V^* (p.u.)	S_{gmax} (p.u.)	Q_{gmax} (p.u.)
1	13	0.005	0.05	1	1.01	0.6	0.36
2	19	0.010	0.10	1	1.01	0.3	0.18
3	25	0.005	0.05	1	1.01	0.6	0.36

Table 3.5: Case study# 3-3: DG units active and reactive power generation

DG #	P_{G-A} (p.u.)	P_{G-B} (p.u.)	P_{G-C} (p.u.)	Q_{G-A} (p.u.)	Q_{G-B} (p.u.)	Q_{G-C} (p.u.)	$P_{G-total}$ (p.u.)	Q_{G-tot} (p.u.)
1	0.102	0.134	0.161	0.097	0.121	0.142	0.397	0.36
2	0.047	0.066	0.086	0.045	0.061	0.074	0.199	0.18
3	0.113	0.132	0.152	0.052	0.063	0.079	0.397	0.194

Table 3.6: Case study# 3-3: load flow results of the proposed power flow algorithm in unbalanced microgrid

Node	Phase A				Phase B				Phase C			
	V_{an} (p.u., degree)		Load (p.u.)		V_{bn} (p.u., degree)		Load (p.u.)		V_{cn} (p.u., degree)		Load (p.u.)	
	Mag.	Ang.	P_L	Q_L	Mag.	Ang.	P_L	Q_L	Mag.	Ang.	P_L	Q_L
1	0.9791	0.0000	0.000	0.000	0.9733	-119.9336	0.000	0.000	0.9707	119.9081	0.000	0.000
2	0.9791	0.0000	0.000	0.000	0.9733	-119.9336	0.000	0.000	0.9707	119.9081	0.000	0.000
3	0.9800	0.0568	0.008	0.006	0.9746	-119.8879	0.012	0.009	0.9720	119.9902	0.016	0.012
4	0.9812	0.1432	0.012	0.010	0.9762	-119.8165	0.018	0.013	0.9737	120.0924	0.018	0.013
5	0.9804	0.1450	0.010	0.007	0.9752	-119.8100	0.012	0.009	0.9725	120.0889	0.014	0.011
6	0.9770	-0.0664	0.010	0.007	0.9704	-119.9828	0.013	0.010	0.9674	119.8277	0.013	0.009
7	0.9765	-0.1379	0.000	0.000	0.9698	-120.0411	0.000	0.000	0.9662	119.7547	0.000	0.000
8	0.9754	-0.0627	0.010	0.007	0.9683	-119.9697	0.012	0.009	0.9650	119.8206	0.014	0.011
9	0.9812	-0.2182	0.014	0.011	0.9761	-120.1485	0.015	0.012	0.9732	119.7098	0.018	0.013
10	0.9871	-0.2996	0.008	0.006	0.9838	-120.2640	0.012	0.009	0.9816	119.6722	0.016	0.012
11	0.9910	-0.3488	0.011	0.008	0.9890	-120.3370	0.010	0.007	0.9874	119.654	0.014	0.011
12	0.9903	-0.3475	0.012	0.008	0.9879	-120.3334	0.018	0.013	0.9863	119.6582	0.018	0.014
13	0.9974	-0.4156	0.008	0.006	0.9974	-120.4156	0.013	0.010	0.9974	119.5844	0.014	0.011
14	0.9722	-0.1306	0.012	0.008	0.9639	-119.9975	0.015	0.012	0.9591	119.7302	0.022	0.016
15	0.9706	-0.1268	0.032	0.024	0.9617	-119.9841	0.040	0.030	0.9568	119.7230	0.048	0.036
16	0.9757	-0.1361	0.010	0.007	0.9687	-120.0345	0.012	0.009	0.9650	119.7512	0.014	0.011
17	0.9713	-0.1282	0.010	0.007	0.9628	-119.9944	0.010	0.007	0.9575	119.7307	0.016	0.012
18	0.9797	0.0182	0.010	0.007	0.9750	-119.9344	0.012	0.009	0.9726	119.9711	0.014	0.011
19	0.9864	-0.0899	0.014	0.011	0.9864	-120.0899	0.015	0.010	0.9864	119.9101	0.018	0.014
20	0.9819	-0.0250	0.008	0.006	0.9790	-120.0017	0.012	0.009	0.9771	119.9637	0.016	0.012
21	0.9770	0.0240	0.010	0.007	0.9713	-119.9229	0.010	0.007	0.9681	119.9809	0.016	0.012
22	0.9755	0.0267	0.012	0.008	0.9689	-119.9154	0.018	0.013	0.9657	119.9892	0.018	0.014
23	0.9851	0.2184	0.014	0.011	0.9812	-119.7571	0.015	0.012	0.9789	120.1850	0.018	0.013
24	0.9900	0.2914	0.008	0.006	0.9873	-119.7060	0.013	0.010	0.9853	120.2817	0.014	0.011
25	1.0003	0.4138	0.014	0.011	1.0003	-119.5862	0.015	0.009	1.0003	120.4138	0.018	0.013

Total	P_{L-A}	Q_{L-A}	P_{L-B}	Q_{L-B}	P_{L-C}	Q_{L-C}	$P_{L-total}$	$Q_{L-total}$	P_{Loss}	Q_{Loss}
	0.258	0.190	0.325	0.240	0.390	0.288	0.973	0.718	0.02	0.015

3.7 Discussion

In this chapter, a generalized three-phase power flow algorithm has been proposed for islanded microgrids. The proposed algorithm incorporates the three-phase feeder models, the load modeling and the DG modeling. To provide proper modeling of the DG units in the islanded microgrid, the power flow problem has been formulated without a slack bus. In this formulation, generation buses have been represented as droop, PV or PQ buses. The proposed formulation reflects the concept of microgrid operation, where DG units are required to share the load demands and keep the system frequency and voltages within their limits. The problem has been formulated as a set of nonlinear equations. To achieve a robust solution and a global convergence in all feasible solutions, a Newton-trust region method has been proposed. The proposed algorithm has been validated by comparing its results with the results of a detailed time-domain simulation. Several case studies for both balanced and unbalanced microgrid test systems have been carried out to show the robustness and effectiveness of the proposed power flow algorithm. The results show good convergence characteristics in all operating conditions. The proposed algorithm is a powerful tool to study the power flow in an islanded microgrid. This power flow analysis helps the DNO to consider the islanded microgrid in both operational and planning studies.

Chapter 4

Maximum Loadability Consideration in Droop-Controlled Islanded Microgrids Optimal Power Flow

4.1 Introduction

Droop controlled islanded microgrid systems are usually complemented with a MGCC to optimize its operation (e.g. [27], [43], [44], [54]). Using non critical low-bandwidth communication links the MGCC collects periodic measurements of the islanded microgrid generation and loads. The MGCC then uses the collected data about the generation and load status to run an OPF problem that updates the DG units' droop settings (i.e. characteristics) in a way that optimally dispatches the different DG units in the island while satisfying the system operational constraints. In this sense, the MGCC periodically performs a higher level coordinated management function by centrally optimizing the update of the DG units droop characteristics. Other than higher level coordination, a major advantage of this scheme is that any failure in the MGCC and/or its associated infrastructure will not result in a complete failure of the islanded microgrid, However, such failures will only imply lack of optimal operation and resorting back to decentralized droop control with no communications; using the droop settings in place at the moment of communication interruption. In general, the OPF problem solved by the MGCC is a nonlinear programming (NLP) problem that is used to determine the "optimal" control parameter settings of a given islanded microgrid in order to minimize some pre-specified desired objective function(s), subject to the system constraints. With the variety of possible objective functions, diverse OPF problems can be defined for the islanded microgrid system. An important consideration in the operation of droop-controlled islanded microgrid systems is its maximum loadability. This chapter proposes the consideration of the system maximum loadability in droop-controlled islanded microgrids OPF problems. Three new OPF problem formulations for droop controlled islanded microgrid systems are investigated; 1) The OPF problem for maximum loadability assessment, 2) The OPF for maximizing system loadability, and 3) The bi-objective OPF problem for loadability maximization and generation cost minimization. The detailed microgrid model proposed in chapter 3 is adopted to reflect the special features and operational characteristics of droop-controlled islanded microgrid systems in the proposed OPF problems formulations. The remainder of this chapter is organized as follows: section 4.2 presents the modeling of droop controlled DG units in islanded microgrid OPF problems. In section 4.3 the proposed droop controlled islanded microgrids OPF formulations are presented. Section 4.4 provides the details of a proposed fuzzy-based utopia tracking algorithm for solving the bi-objective OPF problem for loadability

maximization and generation cost minimization. In section 4.5 the importance and consequences of considering the system maximum loadability in the operational planning of droop-controlled islanded microgrids is validated through comparative numerical case studies. In section 4.6 the chapter is concluded and its main findings are discussed.

4.2 Droop-controlled DG units modelling in islanded microgrid OPF problems

4.2.1 Control parameters

In droop control, the power sharing is achieved by mimicking the behavior of synchronous generators operating in parallel. Hence, as depicted in equation (3.7), the frequency of the DG unit output voltage is drooped as the generated active power by the DG unit increases. Similarly, as depicted in equation (3.8), the magnitude of the DG unit output voltage is drooped as the generated reactive power by the DG unit increases. The previously discussed droop relations, given in (3.7) and (3.8), show that the steady-state operating point (i.e. equilibrium point) of droop-controlled DG units in islanded microgrids depends on the static droop gains of the respective DG unit. The transient behavior of droop controlled DG unit can be adapted to modify the dynamic stability of the islanded microgrid system by incorporating active and reactive power compensators to the droop relations. Accordingly, the droop relations given in (3.7) and (3.8) can be modified to [26], [27], [36]:

$$\omega = \omega_i^* - G_{pi}(s) \times P_{Gi} \tag{4.1}$$

$$|V_i| = V_i^* - G_{qi}(s) \times Q_{Gi} \tag{4.2}$$

where $G_{pi}(s)$ and $G_{qi}(s)$ are the active and reactive power compensators' transfer functions for the DG unit connected to bus i, respectively. Yet, irrespective of the compensators' design (i.e. transfer functions) used, the *dc* gain of the compensators' transfer functions always represents the static-droop gain (i.e. m_{pi} and n_{qi}, respectively) controlling the steady-state operating point of the system [27]. Starting with a pre-specified set of static droop gains to implement a particular steady-state response (i.e. *dc* gains of active and reactive power compensators' transfer functions), the design of $G_{pi}(s)$ and $G_{qi}(s)$ to shape the dynamic response of the DG units, can be achieved as a separate and subsequent step without affecting the required steady state solution of the system. Here it is worth noting that algorithms for scheduling $G_{pi}(s)$ and $G_{qi}(s)$, for different static droop gains values have been previously proposed in [26], [36]. Accordingly, the steady-state behavior of droop-controlled DG units can be represented and studied by (3.7) and (3.8) only. Hence, in this work we only focus on the design of the static droop characteristics droop-controlled DG

unit in the island, given by the control parameters vector *x*, where $x = \{x_j \mid \forall j \in B_{droop}\}$, $x_j = \left[\omega_j^*, V_j^*, m_{pj}, n_{qj}\right]$ and B_{droop} is the set of all droop controlled buses in the system..

4.2.2 Generation capacity

Typically the DG units are equipped with a current limiter intended to limit the P_{Gi} and Q_{Gi} generation of the DG unit to its rated capability [88], [89]. Accordingly, the DG units' P_{Gi} and Q_{Gi} generation follows the droop relations given in (3.7) and (3.8) up till the DG units' maximum active and reactive power generation limits, $P_{Gi,max}$ and $Q_{Gi,max}$, respectively. Beyond $P_{Gi,max}$ the DG unit active power generation is not allowed to follow the droop relation, given by (3.7), and the DG is transformed to inject a constant amount of active power set at the violated limit (i.e. $P_{Gi,max}$). Similarly, beyond $Q_{Gi,max}$ the DG unit reactive power generation is not allowed to follow the droop relation, given by (3.8), and the DG is transformed to inject a constant amount of reactive power set at the violated limit (i.e. $Q_{Gi,max}$). The relationships governing the DG units active and reactive power generation capabilities can be given as:

$$P_{Gi,max} = S_{Gi,max} \tag{4.3}$$

$$Q_{Gi,max} = \sqrt{(S_{Gi,max})^2 - (P_{Gi})^2} \tag{4.4}$$

In order to model the behavior of DG units as they reach their maximum generation capability in the droop-controlled islanded microgrid OPF problem, a set of nonlinear complementary constraints have been adopted. The nonlinear complementary constraint problem, as defined in [56], [49], is to find the vector $\partial \in \Re^n$ such that for the given mappings $\gamma(\partial): \Re^n \to \Re^n$ and $\beta(\partial): \Re^n \to \Re^n$,

$$\gamma(\partial) \geq 0, \;\; \beta(\partial) \geq 0, \; \gamma(\partial) \times \beta(\partial) = 0 \tag{4.5}$$

with the notation "$\perp$" indicating complement, (4.5) can be written as

$$0 \leq \gamma(\partial) \perp \beta(\partial) \geq 0 \tag{4.6}$$

Following this definition, the constraints in (4.7) - (4.8) ensures that the active and reactive power generation of the DG unit is either following the droop characteristics given by (3.7) and (3.8) or set at the DG limits, $P_{Gi,max}$ and $Q_{Gi,max}$, given by (4.3) and (4.4).

$$0 \leq S_{Gi,max} - P_{Gi} \perp \frac{1}{m_{pi}} \times (\omega_i^* - \omega \;) - P_{Gi} \geq 0 \qquad ,\forall\, i \in B_{droop} \tag{4.7}$$

$$0 \leq \sqrt{(S_{Gi,max})^2 - (P_{Gi})^2} - Q_{Gi} \perp \frac{1}{n_{qi}} \times \left(V_i^* - |V_i|\right) - Q_{Gi} \geq 0 \qquad ,\forall\, i \in B_{droop} \tag{4.8}$$

Moreover, droop-controlled DG units have a limit on the apparent power injected from each phase [90]. The limits on the apparent power injected per phase can be given as

$$\sqrt{\left(P_{Gi}^{(\phi)}\right)^2+\left(Q_{Gi}^{(\phi)}\right)^2} \le S_{Gi,max}^{(\phi)} \qquad ,\forall \phi \in \{a,b,c\} \tag{4.9}$$

where $S_{Gi,max}^{(\phi)}$ is the apparent power capacity of phase ϕ for droop controlled DG unit connected to bus *i*.

4.3 Proposed droop-controlled islanded microgrids OPF problem formulations

Similar to conventional power systems [49], [50], [51], [52] in droop-controlled islanded microgrids, the maximum loadability problem is associated with the increase of system demand beyond certain limits leading to the disappearance of the system power-flow solution, i.e., steady-state equilibrium point. The point at which the system steady-state solution disappears (i.e. point of voltage collapse) is known as a static bifurcation point. The steady-state voltage stability margin quantifies how close a particular operating point is to the point of voltage collapse. For a linearly increasing load, with $\lambda \in \Re$ representing a scalar bifurcation parameter known as the "load factor", assuming an increase in the generation capacity to match the load increase, the disappearance of the system steady-state solution with an increasing λ can be related to the appearance of a singularity in the Jacobian matrix of the power flow equations describing the droop controlled islanded microgrid system. This type of bifurcation is known as Saddle Node Bifurcation (SNB). Moreover, considering the generation capacity limits of the different DG units in the islanded microgrid system and the operational limits, a reduced static voltage stability margin might result. In this case, the disappearance of the system equilibrium can arise instantaneously with a sudden jump to instability as the capacity limit of a system equipment or an operational limits is reached. This type of bifurcation is known as Limit Induced Bifurcation (LIB). In droop controlled islanded microgrid the LIB can be related to the violation of the system operational constraints or the shortage of active power supply and/or reactive power supply.

The remainder of this section discusses three formulations that incorporate the maximum loadability consideration in droop-controlled islanded microgrid OPF problem;

4.3.1 OPF problem for maximum loadability assessment

Given some pre-specified control parameters for the droop-controlled DG units in the island, i.e. $x=x_o$, the maximum loading point of a droop controlled islanded microgrid can be calculated by solving the following OPF problem:

$$Min.. \quad -\lambda^{(m)} \tag{4.10a}$$

$$Subject\ to: \quad F(h^{(m)},\lambda^{(m)})=0 \tag{4.10b}$$

$$0 \le S_{Gj,max} - P_{Gj}^{(m)} \perp \frac{1}{m_{pj}} \times (\omega_j^* - \omega^{(m)}) - P_{Gj}^{(m)} \ge 0 \tag{4.10c}$$

$$0 \le \sqrt{\left(S_{Gj,max}\right)^2 - \left(P_{Gj}^{(m)}\right)^2} - Q_{Gj}^{(m)} \perp \frac{1}{n_{qj}} \times \left(V_j^* - \left|V_j\right|^{(m)}\right) - Q_{Gj}^{(m)} \ge 0 \tag{4.10d}$$

$$\sqrt{\left(P_{Gj}^{(\phi,m)}\right)^2 + \left(Q_{Gj}^{(\phi,m)}\right)^2} \le S_{Gj,max}^{(\phi)} \tag{4.10e}$$

$$H_{lb}^{(m)} \le H(h^{(m)},\lambda^{(m)}) \le H_{ub}^{m} \tag{4.10f}$$

$$\forall i \in \{1,2,\ldots,n_{bus}\}, \forall \phi \in \{a,b,c\} \ and \ \ \forall j \in B_{droop}$$

The objective of this OPF problem is to find the maximum loading factor at which the islanded microgrid operation is still feasible as governed by the operational constraints in (4.10b) - (4.10f). In this OPF problem, the current operating point is not considered in the system model. The variables in this problem are the maximum loading level, λ^m, and the power flow state-variables at the system maximum loading point $h^{(m)}$ comprising $\left|V_i\right|^{(\phi,m)}, \delta_i^{(\phi,m)}, \omega^{(m)}, P_{Gj}^{(\phi,m)}$ and $Q_{Gj}^{(\phi,m)}$. On the other hand, the control parameters of the droop-controlled DG units are given as fixed values in this optimization problem at x_o. The equality constraints in (4.10b) represents the power balance conditions at the maximum loading point denoted with a superscript "*m"* ; described by the droop-controlled islanded microgrid power flow equations derived in chapter 3. The complementary constraint in (4.10c) and (4.10d) represent the active and reactive power capacity constraints at the maximum loading condition, respectively. The inequality constraints in (4.10e) represent the DG unit phase loading limits. The inequality constraints in (4.10f) represent the operational limits imposed on the system operation at the point of maximum loading in terms of voltage magnitudes, frequency deviation and distribution feeders' thermal loading limits.

4.3.2 OPF problem for maximizing system loadability

In droop-controlled islanded microgrids, the steady-state voltage stability margin, and consequently the system maximum loadability, is strongly dependent on the sharing of the microgrid demand between the different DG units in the island as determined by the droop characteristics of the droop-controlled DG units in the microgrid. This is similar to conventional power systems where the system voltage stability margin is largely controlled by the dispatch of the different active and reactive power sources in the system [49], [51]. Accordingly, the objective of this OPF problem is to optimally choose the DG units control parameters (that controls the system steady-state solution) so as to maximize the possible loading

margin from the current loading point while guaranteeing the feasibility of both the current and maximum loading points. This problem considers both the current operating point, denoted by a superscript "*c"*, and the maximum loading operating point "*m"*. The mapping between the current and maximum loading points is made through the variable droop-controlled DG units control parameters, *x*, which govern the DG units operation at both operating points. In addition to the maximum loading level, $\lambda^{(m)}$, and the droop-controlled DG units' control parameters, *x*, this problem also assumes that the system power flow variables at both the current operating point and the maximum loading points are variables within the optimization problem. The OPF problem to maximize the islanded microgrid loading margin can be given by;

$$\textit{Min..} \quad -\lambda^{(m)} \tag{4.11a}$$

$$\textit{Subject to:} \quad F(h^{(\ell)},\lambda^{(\ell)},x)=0 \tag{4.11b}$$

$$0 \le S_{Gj,max} - P_{Gj}^{(\ell)} \perp \frac{1}{m_{pj}} \times (\omega_j^* - \omega^{(\ell)}) - P_{Gj}^{(\ell)} \ge 0 \tag{4.11c}$$

$$0 \le \sqrt{\left(S_{Gj,max}\right)^2 - \left(P_{Gj}^{(\ell)}\right)^2} - Q_{Gj}^{(\ell)} \perp \frac{1}{n_{qj}} \times \left(V_j^* - \left|V_j\right|^{(\ell)}\right) - Q_{Gj}^{(\ell)} \ge 0 \tag{4.11d}$$

$$\sqrt{\left(P_{Gj}^{(\phi,\ell)}\right)^2 + \left(Q_{Gj}^{(\phi,\ell)}\right)^2} \le S_{Gj,max}^{(\phi)} \tag{4.11e}$$

$$H_{lb}^{(\ell)} \le H(h^{(\ell)},\lambda^{(\ell)},x) \le H_{ub}^{(\ell)} \tag{4.11f}$$

$$x_{lb} \le x \le x_{ub} \tag{4.11g}$$

$$\forall i \in \{1,2,\ldots,n_{bus}\}, \forall \phi \in \{a,b,c\},\ \forall \ell \in \{c,m\}\ ,and\ \forall j \in B_{droop}$$

The inequality constraints in (4.11g) represents the bounds on the DG units droop control parameters. These bounds are determined by the maximum and minimum allowable voltage and frequency deviation at the PCC for maximum and zero output power production by the DG units.

4.3.3 Bi-objective OPF Problem for loadability maximization and generation cost minimization

This OPF problem is formulated as a bi-criteria optimization problem with the objectives of: 1) minimizing the generation cost, and 2) maximizing the load that can be added to the system, while ensuring that the system operation remain feasible at both the current and maximum loading points. This OPF can be given as:

$$\textit{Min.} \quad \left\lfloor -\lambda^{(m)}, Cost \right\rfloor \tag{4.12a}$$

$$\textit{Subject to:} \quad F(h^{(\ell)},\lambda^{(\ell)},x)=0 \tag{4.12b}$$

$$0 \le S_{Gj,max} - P_{Gj}^{(\ell)} \perp \frac{1}{m_{pj}} \times (\omega_j^* - \omega^{(\ell)}) - P_{Gj}^{(\ell)} \ge 0 \tag{4.12c}$$

$$0 \le \sqrt{\left(S_{Gj,max}\right)^2 - \left(P_{Gj}^{(\ell)}\right)^2} - Q_{Gj}^{(\ell)} \perp \frac{1}{n_{qj}} \times \left(V_j^* - \left|V_j\right|^{(\ell)}\right) - Q_{Gj}^{(\ell)} \ge 0 \tag{4.12d}$$

$$\sqrt{\left(P_{Gj}^{(\phi,\ell)}\right)^2 + \left(Q_{Gj}^{(\phi,\ell)}\right)^2} \le S_{Gj,max}^{(\phi)} \tag{4.12e}$$

$$H_{lb}^{(\ell)} \le H(h^{(\ell)}, \lambda^{(\ell)}, x) \le H_{ub}^{(\ell)} \tag{4.12f}$$

$$x_{lb} \le x \le x_{ub} \tag{4.12g}$$

$$\forall i \in \{1,2,\ldots,n_{bus}\}, \forall \phi \in \{a,b,c\},\ \ell \in \{c,m\}\ , and\ \ \forall j \in B_{droop}$$

where

$$Cost = \sum_{j=1}^{n_{DG}} FC_j(P_{Gj}^{(c)}) \times P_{Gj}^{(c)} \times \chi_j \tag{4.13a}$$

$FC_j(P_{Gj})$ is the fuel consumption of the j^{th} DG unit as a function of its active power generation, and χ_j is the fuel price for the j^{th} DG unit. Here it is worth noting that, if all the DG units in the system have the same fuel price, the minimization of the generation cost in this OPF can be represented by the minimization of the system fuel consumption and equation (4.13a) can be reduced to

$$Cost = \sum_{j=1}^{n_{DG}} FC_j(P_{Gj}^{(c)}) \times P_{Gj}^{(c)} \tag{4.13b}$$

4.4 Bi-objective fuzzy-based utopia tracking algorithm

The problem encountered in the bi-objective OPF problem described in section 4.3.3 is how to balance an economic metric; which is the generation cost, with another metric that cannot be directly translated to an economic value; which is the system loadability. A very popular approach for converting this type of multi-criteria problem into a scalar optimization problem is to convert the multi-objective function into one with single objective by assigning arbitrary relative weights to the different objectives. However, a major disadvantage of this approach is that the effect of the weights is highly dependent on the system state and cannot be known until the problem is solved. Relaxing some objective by a small percentage can lead to a disproportionate reduction in its optimality. Consequently, fixing weights "*a priori*" can lead to large excursions in the optimization performance and output [91]. Another approach determines the required weights by constructing the Pareto front and then selecting an appropriate set of weights from it. However, constructing the Pareto front can be computationally expensive as it requires the solution of numerous optimization problems and is accordingly not feasible for the on-line MGCC application. A

third approach depends on optimizing one of the problem objectives while bounding other objectives to pre-specified limits; by adding them as problem constraints. Nonetheless, the drawback of this approach is that it may be possible to define constraints for which there is no feasible solution to the optimization problem. For instance, an arbitrary defined maximum loadability may be greater than what the system can provide.

In order to overcome the limitations of the aforementioned multi-objective optimization approaches, in this work an alternative approach that yields a single best compromise solution is adopted. This approach entails minimizing the distance between the potential solution and the utopia point (the ideal point given by the intersection of the minima of the independent objectives). The utopia point represents the unbiased point of consensus among the different objectives of the optimization problem; where at such point all the objectives are individually optimal. Figure 4.1 shows a schematic representation of the Pareto front and the Utopia point "*o*" of two competing objective functions f_1 and f_2. As shown on the figure, the Utopia point is the point where all objectives are individually minimized (optimal). The utopia point is generally unattainable because among the Pareto optimal solutions (forming the Pareto front) it is not possible to minimize one objective without increasing the other(s). Even though all the points on the Pareto Front are optimal solutions to the multi-objective optimization problem, still different points on the Pareto front are at different distances (in some norm) to the Utopia point. As shown on Figure 4.1 different optimal solutions on the Pareto front (points "1", "2" and "N") are at different distances to the Utopia point (distances L_1, L_2 and L_N). Given that the utopia point is generally unattainable, the next best thing is a solution that is as close as possible [92], [93]. Accordingly, the best compromise solution is the solution with the minimum distance to the utopia point. A fuzzy utility function is used to transform the problem objectives to non-dimensional objective functions [94]. By associating with each value of the objective functions, a normalized value that expresses the degree of desirability of the considered objective, the fuzzy utility functions serves to equate the relative differences (i.e. difference in magnitude and units) between the generation cost and the maximum loading. In other words, the fuzzy utility function is used to transform the problem objectives to non-dimensional objective functions in order to allow for the representation of closeness to the utopia point mathematically.

The multi-objective OPF problem given by (4.12) is solved by a fuzzy-based approach to determine the best compromise solution between the two non-commensurable and conflicting objectives [92], [93], [94]. This approach avoids the need for setting time invariant weights and does not require the computation of the Pareto front for the solving the bi-criteria OPF problem. Figure 4.2 shows a flow chart of the proposed approach. First, the individual objectives of maximum loadability and generation cost minimization are optimized separately. The first objective is optimized by solving the OPF problem

given in Section 4.3.2. The second objective is optimized by solving the OPF problem given in equations (4.14a) – (4.14g).

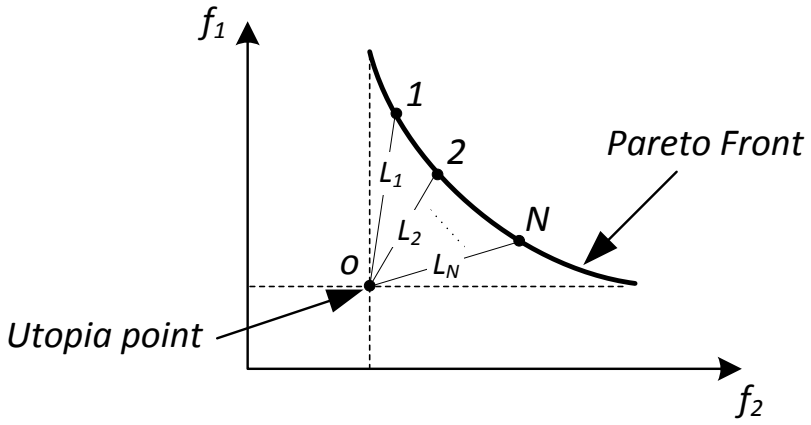

Figure 4.1: Schematic representation of Pareto front and Utopia point

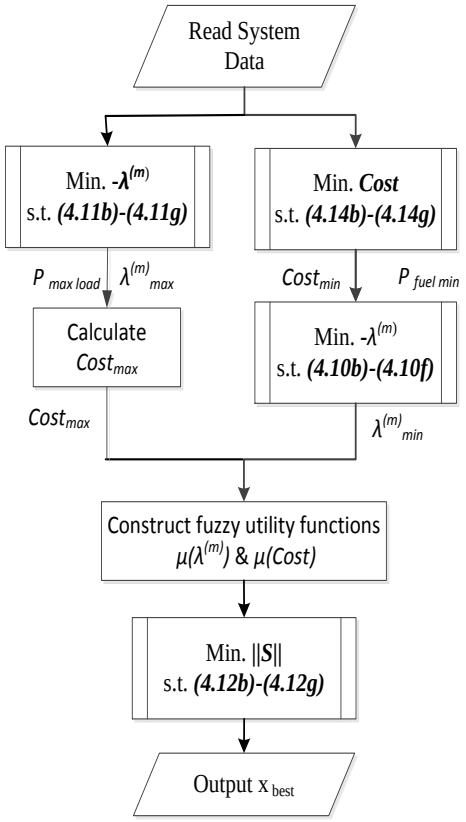

Figure 4.2: Flowchart of the proposed bi-objective fuzzy-based utopia tracking algorithm

$$\textit{Min.} \qquad \textit{Cost} \tag{4.14a}$$

$$\textit{Subject to:} \qquad F(h^{(c)}, x) = 0 \tag{4.14b}$$

$$0 \le S_{Gj,max} - P_{Gj}^{(c)} \perp \frac{1}{m_{pj}} \times (\omega_j^* - \omega^{(c)}) - P_{Gj}^{(c)} \ge 0 \tag{4.14c}$$

$$0 \le \sqrt{\left(S_{Gj,max}\right)^2 - \left(P_{Gj}^{(c)}\right)^2} - Q_{Gj}^{(c)} \perp \frac{1}{n_{qj}} \times \left(V_j^* - \left|V_j\right|^{(c)}\right) - Q_{Gj}^{(c)} \ge 0 \tag{4.14d}$$

$$\sqrt{\left(P_{Gj}^{(\phi,c)}\right)^2 + \left(Q_{Gj}^{(\phi,c)}\right)^2} \le S_{Gj,max}^{(\phi)} \tag{4.14e}$$

$$H_{lb}^{(c)} \le H(h^{(c)}, \lambda^{(c)}, x) \le H_{ub}^{(c)} \tag{4.14f}$$

$$x_{lb} \le x \le x_{ub} \tag{4.14g}$$

$$\forall i \in \{1,2,\ldots,n_{bus}\}, \forall \phi \in \{a,b,c\} \text{ and } \forall j \in B_{droop}$$

The optimal solutions of the individual problems are used to set the lower and upper bounds of the two objectives i.e. the optimal solution to the generation cost minimization problem sets the lower bound on system loadability, $\lambda^{(m)}_{min}$, and generation cost, $Cost_{min}$; while the optimal solution to the maximum loadability problem sets the upper bounds on system loadability, $\lambda^{(m)}_{max}$, and generation $Cost_{max}$. Here it is worth noting that the generation cost minimization problem; given in (4.14), does not consider the system maximum loadability. Accordingly, $\lambda^{(m)}_{min}$ is obtained by solving the maximum loadability assessment OPF problem, given in section 4.3.1, using the droop settings obtained from generation cost minimization OPF problem. Second, the lower and upper bounds on the individual objectives are used to characterize fuzzy utility functions of the two objectives concerned. The fuzzy utility function of an objective is defined as a value ranging from 0 to 1, with value of 1 indicating full desirability of the objective value, and 0 denoting full undesirability of the objective value. Values between 0 and 1 of the fuzzy utility function represent the degree of desirability of an objective value. Accordingly, the fuzzy utility functions give normalized values that express the degree of desirability of each objective and as such resolves the relative differences in magnitude and units between the generation cost and the maximum loading. Figure 4.3 shows the schematic diagram of the linear utility functions for generation cost and loadability. As shown on the figure the utility membership of the generation cost can be given as:

$$\begin{aligned} \mu(Cost) &= 1, \quad \forall Cost \le Cost_{min} \\ &= \frac{Cost - Cost_{max}}{Cost_{min} - Cost_{max}}, \quad \forall Cost_{min} < Cost < Cost_{max} \\ &= 0, \quad \forall Cost \ge Cost_{max} \end{aligned} \tag{4.15}$$

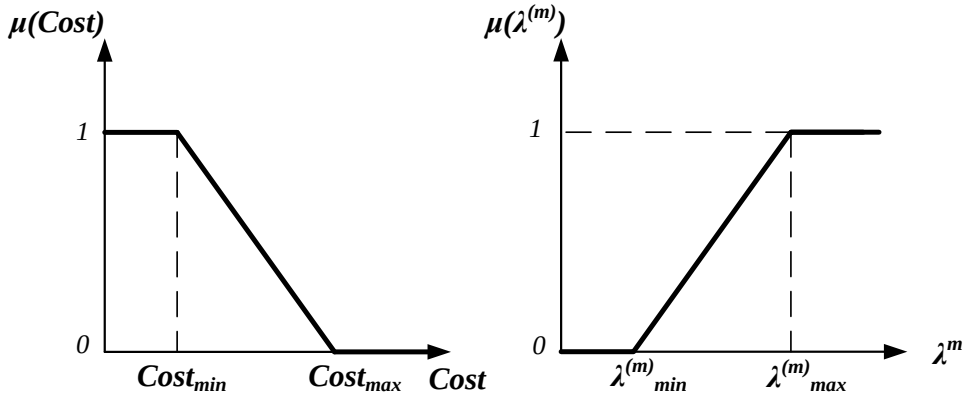

Figure 4.3: Fuzzy desirability membership functions

and the utility function of the system loadability can be given as:

$$\begin{aligned} \mu(\lambda^{(m)}) &= 0, \quad \forall \lambda^{(m)} \le \lambda^{(m)}_{min} \\ &= \frac{\lambda^{(m)} - \lambda^{(m)}_{min}}{\lambda^{(m)}_{max} - \lambda^{(m)}_{min}}, \quad \forall \lambda^{(m)}_{min} < \lambda^{(m)} < \lambda^{(m)}_{max} \\ &= 1, \quad \forall \lambda^{(m)} \ge \lambda^{(m)}_{max} \end{aligned} \tag{4.16}$$

Finally, the bi-objective optimization problem is solved by minimizing the distance of the solution to the utopia point ($\lambda^{(m)}_{max}$, $Cost_{min}$). The Euclidean distance of the solution ($\lambda^{(m)}$,*Cost*) to the utopia point can be given as;

$$\|S\| = \sqrt{(1-\mu(\lambda^{(m)}))^2 + (1-\mu(Cost))^2} \tag{4.17}$$

The lower $\|S\|$ value the solution has, the shorter its distance from the ideal point is. Accordingly minimizing (4.17), subject to (4.12b) - (4.12f), yields the best compromise solution with the shortest distance to the utopia point.

4.5 Numerical results

In this section, a balanced and unbalanced distribution test systems have been chosen to assess the effectiveness of the proposed problem formulations. Three OPF problems are solved for each of these systems to demonstrate the importance and consequence of considering the system maximum loadability on the selection of droop-controlled islanded microgrids control parameters. The three problems are as follows:

1) The OPF problem for minimizing the overall system generation cost (given by (4.14)); results from this OPF problem are denoted by *"Minimum Cost"*.

2) The OPF problem for maximizing the system loading margin (given by (4.11)); results from this OPF problem are denoted by *"Maximum Loadability".*
3) The OPF problem for achieving the best possible compromise between the system maximum loadability and minimum generation cost using the fuzzy-based utopia tracking method (given by (4.12)); results from this OPF problem are denoted by *"Best Compromise".*

The proposed OPF problems were implemented in Matlab environment. The upper and lower limits on the node voltage variation are taken as 1.05 p.u. and 0.95 p.u., respectively. A maximum frequency variation of ± 0.005 p.u. is considered in the reported case studies. The complementary constraints were transformed to nonlinear constraints using a Fischer-Burmeister-based method [56], [95]; where a nonlinear complementary problem function $\Psi : \Re^2 \to \Re$ on the form of:

$$\Psi(a,b) = 0 \Leftrightarrow a \geq 0, b \geq 0, a.b = 0 \tag{4.18}$$

Can be expressed by the Fischer-Burmeister Function as:

$$\Psi(a,b) := \sqrt{a^2 + b^2} - (a + b)) \tag{4.19}$$

4.5.1 Case study# 4-1: balanced microgrid

The 33-bus balanced test system is used in this case study [96]. The system single line diagram, feeder parameters (at nominal frequency) and load power are given in Appendix A. An islanded microgrid is formed by isolating the system from the main grid by the island isolation switch. Table 4.1 shows the DG units' ratings, locations, and fuel consumption (Natural Gas) in standard cubic feet per kilowatt-hour (scf/kWh). Table 4.2 shows the optimal settings for droop-based DG units obtained by solving the three OPF problems under consideration. As discussed in section 4.3.3, given that the DG units in the system utilize the same type of fuel, the system generation cost is represented by the fuel consumption. Table 4.3 shows the overall islanded microgrid generation cost and maximum loadability when the islanded microgrid is operated with the settings obtained from each OPF problem. As shown in the results, in the "minimum cost" OPF problem the whole emphasis is on minimizing the system generation cost and no emphasis is placed on enhancing the system maximum loadability. As such, in this case the lower generation cost of the islanded microgrid can be achieved on the expense of smaller loading margins. On the other hand, the "maximum loadability" OPF problem enables the operation of the islanded microgrid system with larger loading margins on the expense of higher generation cost. These results demonstrate the trade-off between the minimization of the system generation cost and the maximization of the system loadability. The fuzzy-based utopia-tracking algorithm "best compromise" locates the best trade-off between the system loading margin and generation cost at the system current operating condition. Note that the ideal generation cost is around *35,118.5 (scf/hr)* given by the limit in which the system maximum

loadability is fully relaxed. This also represents the absolute minimum generation cost required to keep the islanded microgrid operating at this loading level. The generation cost of the best compromise solution is around *35,520.6 (scf/hr)* which indicates that the cost of the increase in system maximum loadability from 1.179 *p.u.* to *1.456 p.u.* is 402.1*(scf/hr)*.

Table 4.1: Case study# 4-1: DGs locations, fuel consumption and ratings

DG #	*Location (Bus #)*	*Fuel Consumption (scf/kWh)*	S_{Gmax} *(p.u.)*
1	08	7.806	1
2	09	7.316	1
3	22	11.165	2
4	02	11.105	2
5	25	11.418	1

Table 4.2: Case study# 4-1: droop settings obtained from the three OPF problems under consideration

DG #	**Minimum Cost**			
	m_p *(p.u.)*	n_q *(p.u.)*	V^* *(p.u.)*	ω^* *(p.u.)*
1	*5.25E-04*	*3.33E-02*	*1.034*	*1.0002*
2	*6.31E-04*	*1.60E-02*	*1.038*	*1.0002*
3	*1.34E-03*	*1.39E-03*	*1.050*	*0.9998*
4	*4.17E-04*	*7.11E-04*	*1.049*	*1.0001*
5	*2.69E-03*	*5.87E-03*	*1.045*	*0.9999*
DG #	**Maximum Loadability**			
	m_p *(p.u.)*	n_q *(p.u.)*	V^* *(p.u.)*	ω^* *(p.u.)*
1	*1.20E-03*	*2.47E-02*	*1.016*	*1.0002*
2	*1.13E-03*	*2.59E-02*	*1.018*	*1.0001*
3	*4.18E-04*	*1.51E-06*	*1.050*	*1.0000*
4	*5.91E-04*	*1.80E-03*	*1.029*	*1.0001*
5	*9.92E-04*	*9.34E-03*	*1.022*	*1.0000*
DG #	**Best Compromise**			
	m_p *(p.u.)*	n_q *(p.u.)*	V^* *(p.u.)*	ω^* *(p.u.)*
1	*6.59E-04*	*2.00E-02*	*1.027*	*1.0002*
2	*6.59E-04*	*1.79E-02*	*1.027*	*1.0002*
3	*5.05E-04*	*5.39E-04*	*1.049*	*1.0001*
4	*1.04E-06*	*7.46E-03*	*1.034*	*0.9996*
5	*8.41E-04*	*2.80E-02*	*1.036*	*1.0002*

Table 4.3: Case study # 4-1: maximum loadability and total generation cost

	$\lambda^{(m)}$ *(p.u.)*	*Cost (scf/hr)*
Minimum Cost	*1.179*	*35,118.5*
Maximum Loadability	*1.517*	*38,468.2*
Best Compromise	*1.456*	*35,520.6*

Figures 4.4 (a)-(c) show the voltage profile at the current loading level as the system is operated with the settings obtained from the different OPF problems. Even though the results in Figures 4.4 (a)-(c) show that the settings obtained from the three OPF problems are capable of satisfying the voltage constraints at the current operating point, still the distance of the current operating point to the point of voltage collapse is different in the three cases. Figure 4.5 (a) shows the voltage magnitude profile as a function of the system loadability (PV curve) for the most remote bus in the islanded microgrid (bus #33) when the microgrid is operated with the settings obtained from the three OPF problems. When the islanded microgrid is operated with the settings obtained from the "minimum cost" OPF problem, point "A" represent the SNB point and any increase of the system loading beyond point "A" will result in a voltage collapse. When the islanded microgrid is operated with the settings obtained from the "best compromise" OPF problem, point "B" shows the system maximum loadability when all system constraints are enforced at the maximum loading point, while point "D" shows the system maximum loadability when voltage constraints are relaxed at the maximum loading point; with all other constraints enforced. All system constraints are always enforced at the current loading point. The rapid descend in the voltage magnitude from point "B" to point "D", can be associated to the transfer of the reactive power support from DG #4 to the remoter DG #3 as DG #4 reaches its maximum capacity at point "B". Both points "B" and "D" represent a LIB when the system operates with these settings. Points "C" and "E" represent similar system loading levels when the system is operated with the settings obtained from the "Maximum Loadability" OPF problem. Figure 4.5(b) shows the system frequency as a function of the system loading level, as can be seen in the figure the limits imposed on the selection static droop coefficients guarantee to keep the system frequency within the allowable deviation tolerance as the system loading increase. It is worth noting that similar bounds imposed on the reactive power static droop gain coefficients can only ensure proper voltage regulation at the PCC.

In order to explain the different points of voltage collapse attained by the different settings, Figures 4.6 (a)-(i) show the active, reactive and apparent power production by the different DG units in the islanded microgrid as the loading factor of the microgrid increase in steps of 0.005 p.u.; when the DG units are operated with the three sets of settings given in Table 4.2. The results in Figures 4.6 (a)-(i) show that even though the initial islanded microgrid loading factor is the same, the maximum loading factor that can be attained by the three settings is different. Without violating the DG capacity constraints, the settings obtained from the "maximum loadability" and the "best compromise" OPF problems allow the islanded microgrid to feed higher load demand as compared to the settings obtained from "minimum cost" OPF problem. Figures 8(a)-(i) also show that the complementary constraints given in (4.7)-(4.8) are capable of correctly modeling the behavior of the droop controlled DG units as they reach their maximum generation capability and transform to inject their maximum generation capacity. The increase of active power

generation with the increase of the system loading is governed by the droop relation given in (3.7) for all the droop-controlled DG units in the system. As the DGs reaches their respective maximum apparent power capacity, the reactive power production switches from being governed by the droop equation given by (4.8) to being governed by the available capacity as denoted by (4.4). For instance, Figure 4.6 (a)-(c) show that DG unit #5 produces its maximum apparent power at a loading factor of 1.046. Hence, further increase in the loading factor results in a decrease in the reactive power production of DG #5 to preserve its active power sharing capability up to the maximum loading point at which ($P_{G\ DG\#5}$=0.2076 p.u., and $Q_{G\ DG\#5}$=0.9781 p.u.). The rate of decrease in the reactive power production as the DG unit reaches its maximum apparent power capacity is governed by the active power static droop coefficient i.e. the rate of active power production increase. This explains the difference in the rate of reactive power production change as the system loading increase between DG #4 and DG #5 in the "minimum cost" case. Fig 4.7 (a)-(c) show the fast convergence characteristics of the three OPF problems under consideration.

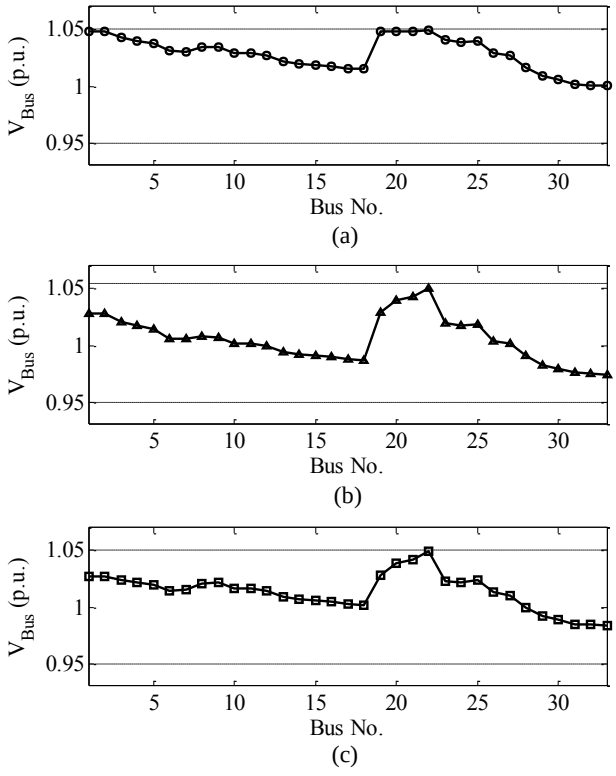

Figure 4.4: Case study# 4-1: voltage profile when the system is operated with the settings obtained from: a) minimum cost, b) maximum loadability, and c) best compromise.

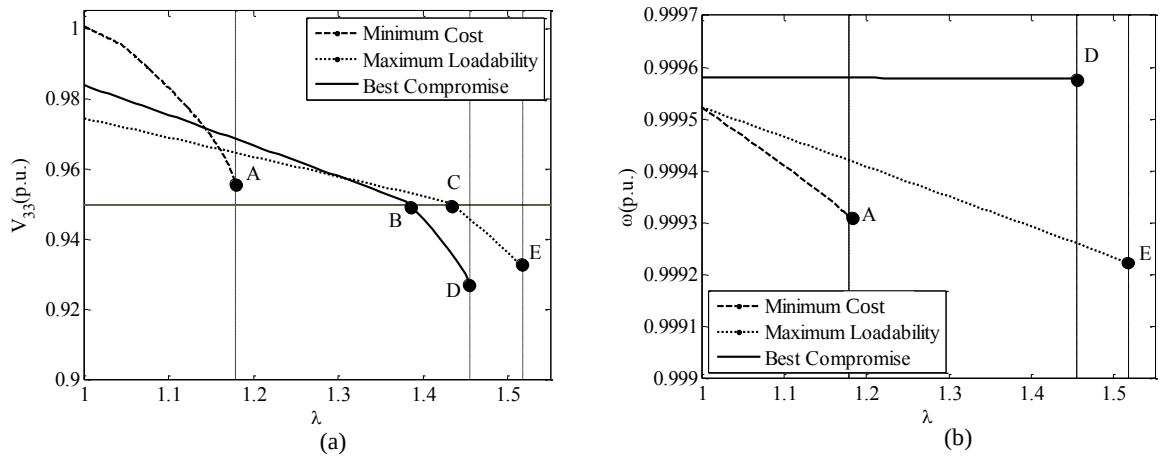

Figure 4.5: Case study# 4-1: a) voltage at bus #33, and b) system frequency, as a function of λ under the different settings

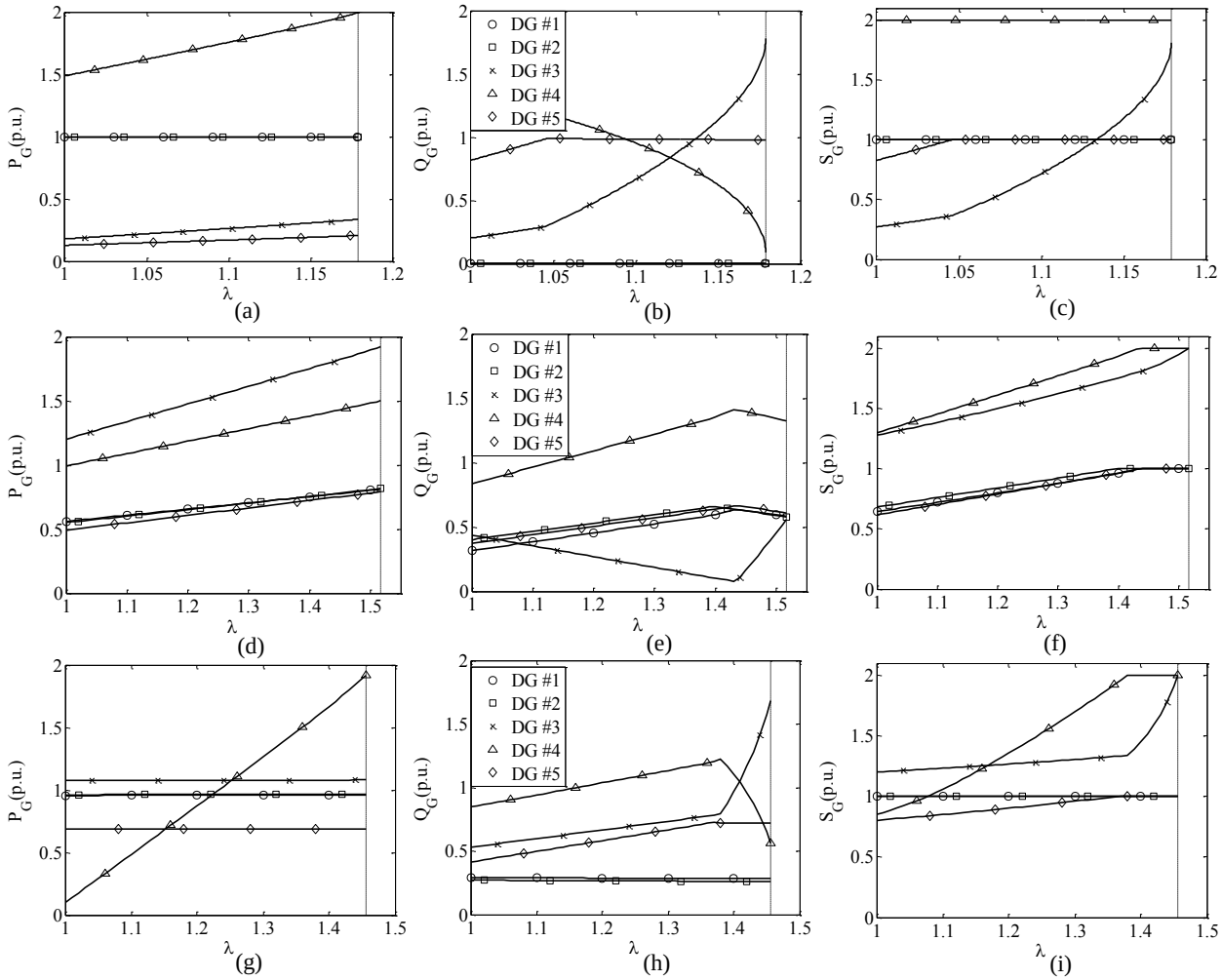

Figure 4.6: Case study # 4-1: DG units' generation as λ increases with the settings obtained from: (a)-(c) minimum cost, (d)-(f) maximum loadability, and (g)-(i) best compromise

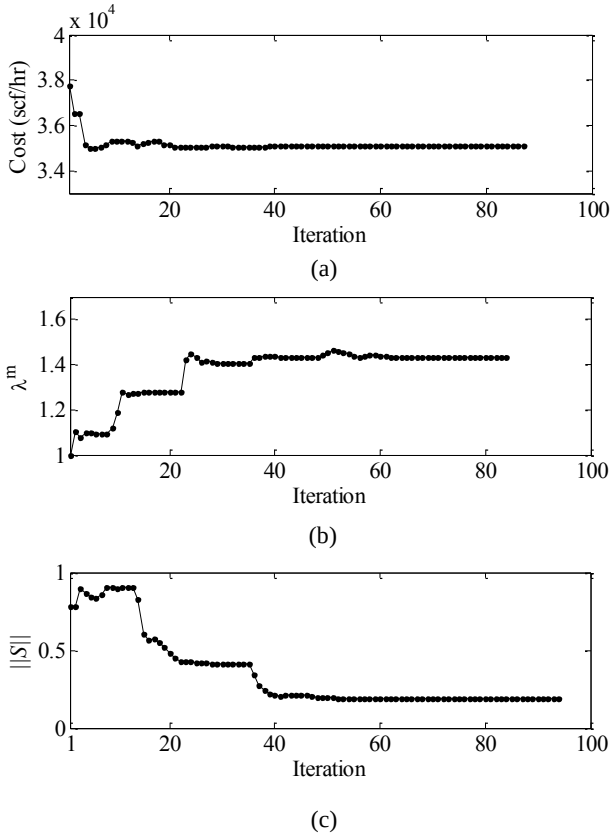

Figure 4.7: Case study# 4-1: convergence characteristics of the OPF problem: a) minimum cost, b) maximum loadability, and c) best compromise

4.5.2 Case study# 4-2: unbalanced microgrid

A 25 bus unbalanced test system [87] is used in this case study. The system single line diagram, feeder parameters (at nominal frequency) and phase load power are given in Appendix A. The islanded microgrid is formed by isolating the distribution system from the main grid by the island isolation device shown on the figure. The feeder parameters and load nominal power are given in. Three DG units have been placed at buses 13, 19 and 25 to feed the system demand in islanded microgrid mode of operation. Table 4.4 shows the ratings, locations, and fuel consumption (Natural Gas) of these DG units. Table 4.5 shows the optimal settings for the DG units obtained by solving the three OPF problems under consideration. Table 4.6 shows the overall islanded microgrid generation cost and maximum loadability when the islanded microgrid is operated with the settings obtained from each OPF problem. Similar to the results obtained in the balanced islanded microgrid case study, the fuzzy-based utopia-tracking algorithm "best compromise" was able to locate the best trade-off between the two objectives under consideration.

Table 4.7 shows the active and reactive power injected, at λ=1, from each phase by each DG when the islanded microgrid is operated with the settings obtained from each of the three OPF problems under consideration. The three-phase active power generation is shared in accordance to the droop settings in

place, even though there is no equal sharing between the generated active powers in each phase. Figure 4.8 shows the minimum voltage for all system phases as the system loading increase when the system is operated with the settings obtained from the three OPF problems under consideration. Points *A*', *D'* and *F'* represent the system maximum loading points when all the system constraints are enforced at the maximum loading point. Points *B'*, *D'* and *G'* represent the system maximum loading when the maximum phase loading constraints are relaxed at the maximum loading point; with all other constraints enforced. Points *C'*, *E'* and *H'* represent the system maximum loading when both the maximum phase loading and the voltage magnitude constraints are relaxed at the maximum loading conditions; with all other constraints enforced. All system constraints are always enforced at the current loading point. Here it is worth noting, that for this system configuration relaxing the phase loading conditions when the islanded microgrid is operating with the settings obtained from the "best compromise" OPF did not result in any improvement in the system loading. Figure 4.9(a)-(c) shows the fast convergence characteristics of the three OPF problem formulations under consideration in the unbalanced islanded microgrid case. The results obtained in this case study show the importance and effectiveness of considering the system maximum loadability in unbalanced islanded microgrid OPF.

Table 4.4: Case study# 4-2: DGs locations, fuel consumption and ratings

DG #	*Location (Bus #)*	*Fuel Consumption (scf/kWh)*	S_{Gmax} *(p.u.)*
1	*13*	*7.806*	*1*
2	*19*	*7.316*	*1*
3	*25*	*11.418*	*1*

Table 4.5: Case study# 4-2: droop settings obtained from the three OPF problems under consideration

DG #	**Minimum Cost**			
	m_p *(p.u.)*	n_q *(p.u.)*	V^* *(p.u.)*	ω^* *(p.u.)*
1	*2.97E-03*	*3.17E-02*	*1.0292*	*1.0059*
2	*3.47E-03*	*4.07E-06*	*1.05*	*1.0074*
3	*2.33E-03*	*2.24E-02*	*1.0089*	*1.005*
DG #	**Maximum Loadability**			
	m_p *(p.u.)*	n_q *(p.u.)*	V^* *(p.u.)*	ω^* *(p.u.)*
1	*2.31E-03*	*2.12E-02*	*1.0243*	*1.0068*
2	*2.96E-03*	*2.57E-03*	*1.0483*	*1.0073*
3	*2.90E-03*	*6.46E-04*	*1.0496*	*1.0073*
DG #	**Best Compromise**			
	m_p *(p.u.)*	n_q *(p.u.)*	V^* *(p.u.)*	ω^* *(p.u.)*
1	*1.52E-03*	*5.00E-02*	*1.0432*	*1.0057*
2	*4.68E-03*	*8.14E-03*	*1.05*	*1.0078*
3	*6.17-04*	*1.62E-02*	*1.05*	*1.0051*

Table 4.6: Case study# 4-2: maximum loadability and total generation cost

	$\lambda^{(m)}$ *(p.u.)*	*Cost (scf/hr)*
Minimum Cost	1.624	7,534.0
Maximum Loadability	2.341	8,899.6
Best Compromise	2.293	7,660.6

Table 4.7: Case study# 4-2: DG units active and reactive phase power generation at, λ=1

DG #	**Minimum Cost**					
	$P_G^{(a)}$	$Q_G^{(a)}$	$P_G^{(b)}$	$Q_G^{(b)}$	$P_G^{(c)}$	$Q_G^{(c)}$
1	0.102	0.109	0.105	0.115	0.102	0.113
2	0.225	0.086	0.227	0.082	0.233	0.09
3	0.006	0.05	0.004	0.051	0	0.045
DG #	**Maximum Loadability**					
	$P_G^{(a)}$	$Q_G^{(a)}$	$P_G^{(b)}$	$Q_G^{(b)}$	$P_G^{(c)}$	$Q_G^{(c)}$
1	0.088	0.063	0.088	0.069	0.088	0.063
2	0.119	0.088	0.12	0.088	0.121	0.091
3	0.122	0.091	0.124	0.088	0.122	0.091
DG #	**Best Compromise**					
	$P_G^{(a)}$	$Q_G^{(a)}$	$P_G^{(b)}$	$Q_G^{(b)}$	$P_G^{(c)}$	$Q_G^{(c)}$
1	0.131	0.064	0.132	0.067	0.136	0.065
2	0.193	0.004	0.192	0	0.201	0.003
3	0.009	0.179	0.013	0.182	0	0.181

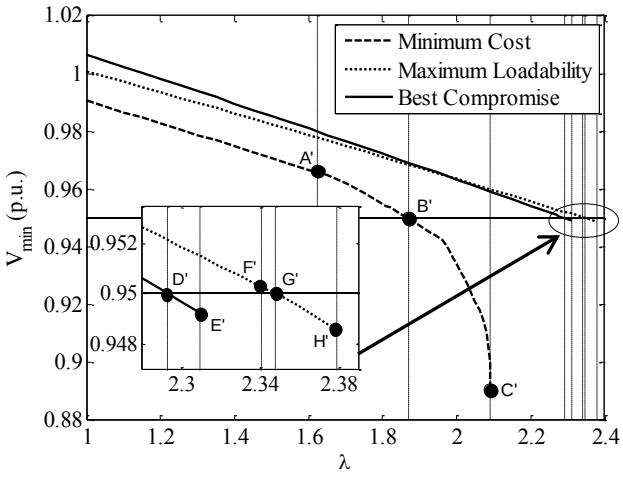

Figure 4.8: Case study# 4-2: minimum voltage as a function of λ under the different settings

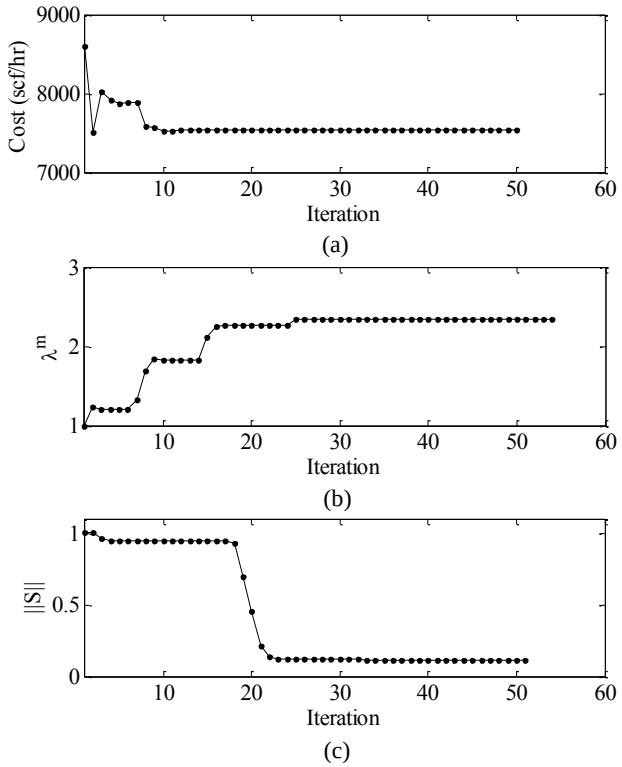

Figure 4.9: Case study# 4-2: convergence characteristics of the OPF problem in case study #2: a) minimum cost, b) maximum loadability, and c) best compromise

4.6 Discussion

This chapter addressed the problem of droop controlled islanded microgrid OPF considering the system maximum loadability. Three OPF problems formulations are proposed; 1) The OPF problem for maximum loadability assessment, 2) The OPF for maximizing system loadability, and 3) The bi-objective OPF problem for loadability maximization and generation cost minimization. A detailed steady-state model that takes into consideration the special operational characteristics of droop controlled islanded microgrids has been adopted in the proposed OPF problems formulations. The importance of considering the system maximum loadability has been investigated on balanced and unbalanced microgrid test systems. The numerical results verify the effectiveness of the proposed OPF problems formulations in considering the droop-controlled islanded microgrid maximum loadability; while taking into account other system constraints; including DG capabilities, power flow constraints, frequency and voltage regulation. The results show that the optimal choice of the islanded microgrid droop settings can allow the microgrid to operate at higher loading factor and/or minimize the overall microgrid generation cost without violating any of the system constraints.

Chapter 5

Optimum Droop Parameters Settings of Decentralized Islanded Microgrids Including Renewable Energy Resources

5.1 Introduction

In chapter 4, the choice of the droop parameters for islanded microgrids operating in the presence of a MGCC was discussed. In such cases, the MGCC periodically collects data about the microgrid generation and demand, solves the islanded microgrid OPF problem and consequently perform a periodic update of the droop settings for the different DG units in the island to implement the required OPF. On the other hand, the operation of islanded microgrid systems without a MGCC (and its associated communication) is still a viable solution in the cases at which the microgrid doesn't have a MGCC or when the MGCC and/or its associated communication links fail to operate. For instance, in the cases of communication/MGCC failure/non-existence, data about the system status and control signals cannot be transmitted online and therefore DG units droop settings cannot be updated periodically. As such, in these scenarios the DG units droop settings have to be predesigned offline for a possible operational planning horizon within which islanded microgrids might be initiated. The absence of the MGCC in these scenarios renders the problem of choosing the optimal droop characteristics more complicated in terms of considering the possible microgrid configurations that can be initiated and the variability associated with the microgrid renewable generation and loads. Accordingly, this chapter proposes a new probabilistic algorithm for determining the optimum choice for such droop settings for individual DG units in a distribution network in cases when a MGCC is unavailable. The proposed algorithm adopts a constraint hierarchy approach to enhance the operation of islanded microgrids by satisfying the operational constraints of the system and expanding its loading margin. The new algorithm takes into consideration the variety of possible islanded microgrid configurations that can be initiated in a distribution network (multi-microgrids), the uncertainty and variability associated with the output power of renewable DG units as well as the variability of the load, and the special features and operational philosophy associated with droop-controlled islanded microgrid systems. The proposed algorithm can thus be an effective and powerful tool for helping DNOs select the optimum droop settings for the DG units in the distribution network in order to enable the successful operation of islanded microgrids either in the absence of an MGCC or when an MGCC fails to operate. The remainder of this chapter is organized as follows: section 5.2 discusses the variety of possible islanded microgrid configurations that can be initiated in a distribution network. In section 5.3, a probabilistic load-generation model that incorporates the stochastic

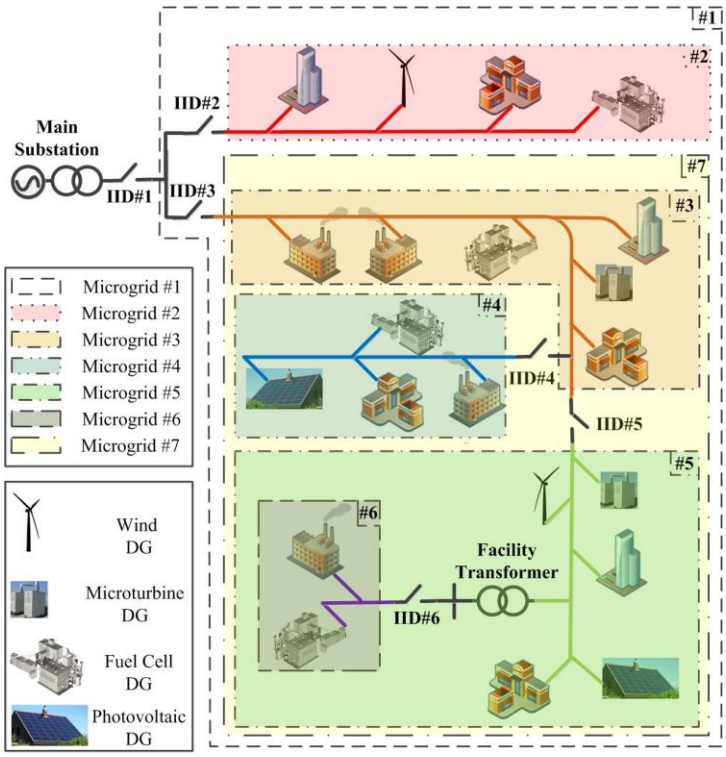

Figure 5.1: Structure of a distribution network considering microgrids

nature of droop-controlled islanded microgrid components is introduced. The formulation of the problem of optimally choosing the droop settings for the individual DG units is explained in section 5.4. Section 5.5 provides the simulation results for a variety of case studies that demonstrate the effectiveness and significance of the proposed approach. Section 5.6 concludes the chapter and summarizes its main contributions.

5.2 Islanded microgrid configurations

In a distribution network that includes DG units, a variety of islanded microgrid configurations can be created and can be identified based on the zone associated with the devices that permit the islanding of the microgrid from the distribution network (i.e., island isolation devices (IIDs)) [10]. Such devices can be circuit breakers or automatic re-closers. Figure 5.1 depicts examples of microgrid configurations that can be initiated in a distribution network. As shown, the distribution network is configured into a set of microgrids, each of which is basically a group of components (e.g., lines, DG units, loads, and protection devices) with an IID at its entry. It is worth noting that a DG unit or load point can belong to different possible microgrid configurations depending on the fault and the IID location. For example, as shown in Figure 1, load points downstream of IID #6 can fall within islanded microgrid #1, #5, #6, or #7, depending on the location of the fault that initiates the islanded operation. Based on this structure and

with the absence of an MGCC, one islanded microgrid will be initiated to include all downstream microgrids if a fault occurs in its upstream system. For instance, Microgrid #6 will be islanded if a fault occurs upstream of it in the electrical region defined by Microgrid #5. However, Microgrid #5 will be islanded if a fault occurs in the electrical region defined by Microgrid #3.

5.3 Probabilistic islanded microgrid model

Accurate droop setting for islanded microgrid systems should take into consideration the stochastic nature of both the generation and the loads. This section explains the analytical development of a combined generation load model for describing all possible system states and their respective probabilities [97]. Assuming that the probabilities of the generation states in the operational planning horizon $\rho_{st}^{G}\{N_{st}^{G}\}$ are independent of the probabilities of the load states $\rho_{st}^{L}\{N_{st}^{L}\}$, the probabilities of states $\rho_{st}\{N_{st}\}$ describing different possible combinations of generation and load states in an islanded microgrid can be obtained by convolving their respective probabilities as follows:

$$\rho_{st}\{N_{st}\} = \rho_{st}^{G}\{N_{st}^{G}\} * \rho_{st}^{L}\{N_{st}^{L}\} \tag{5.1}$$

where $\{N_{st}^{G}\}$ is the set of all possible generation states, $\{N_{st}^{L}\}$ is the set of all possible load states, and $\{N_{st}\}$ is the set of all possible islanded microgrid states. Based on equation (5.1), the generation load model for an islanded microgrid can be obtained by listing all possible combinations of generation output power states and load states. Similarly, different generation states are composed by convolving generation state probabilities based on the state model of each type of DG unit. For two DG units, G_1 and G_2, with different state models, the model of the combined generation states can be obtained as follows:

$$\rho_{st}^{G}\{N_{st}^{G}\} = \rho_{st}^{G1}\{N_{st}^{G1}\} * \rho_{st}^{G2}\{N_{st}^{G2}\} \tag{5.2}$$

where $\{N_{st}^{G1}\}$ and $\{N_{st}^{G2}\}$ are the set of all possible generation states for the first and second DG units, respectively. Generally, the generation states model for variable power DG units is calculated by dividing the continuous probability distribution function (PDF) into several states. For example, the generation states model of wind-based DG units can be extracted by dividing the wind speed PDF into several states with a step of 1 m/sec. The probability of a wind state *st* can then be calculated as follows:

$$\rho_{st}^{wind}(st) = \int_{v_{st,min}}^{v_{st,max}} f(v)dv \tag{5.3}$$

where *f(v)* is the distribution probability of wind speed, $v_{st,min}$ and $v_{st,max}$ are the wind speed limits of state *st*. Similar approaches can be used for other variable power sources [97]. The studies in [97] revealed no significant differences between the results obtained using this analytical approach and those obtained using Monte Carlo simulation (MCS).

5.4 Proposed optimum droop parameters settings

In this work, dispatchable DG units operating in droop-controlled mode provide the energy buffering required for enabling islanded operation [98], [99]. On the other hand, renewable energy resources are locally controlled in order to track their maximum power operating point and are therefore represented as PQ buses in the islanded microgrid model. The choice of droop settings for the operation of the droop-controlled DG units in the event that an islanded microgrid is initiated can significantly impact the capability of such an island to successfully feed its loads. This section presents the formulation of the problem of optimally choosing the droop settings for such DG units in a given distribution network in order first to satisfy the operational constraints of the system and second to enhance the voltage security margins. The droop setting variables to be determined can be given as

$$x = \left\{ x_j \mid \forall j \in B_{droop} \right\} \tag{5.4}$$

where

$$x_j = \left\lfloor \omega_j^*, V_j^*, m_{pj}, n_{qj} \right\rfloor \tag{5.5}$$

and B_{droop} is the set of all droop-controlled buses in the system. The proposed algorithm takes into consideration 1) the unavailability of a MGCC and its associated communication infrastructure, 2) the uncertainty and variability associated with the system loads and renewable generation, 3) the different possible islanded microgrid configurations that can be initiated in the distribution network, and 4) the special features and operational philosophy of droop-controlled islanded microgrid systems. Figure 5.2 shows a flowchart of the proposed probabilistic algorithm. As can be seen, the algorithm is divided into two stages, as detailed in the following subsections.

5.4.1 Stage #1: supply adequacy evaluation

Irrespective of the droop settings in place, an island can be successful if and only if there is enough generation to match the total demand of the island. The first stage in the proposed algorithm is therefore to determine the set of states with sufficient generation to meet its respective demand for each possible islanded microgrid (i.e., the set of admissible microgrid states). Based on the generation-load model described in section 5.3, the necessary condition for an islanded *is* operating at a given state *st* to be admissible is given as follows:

$$\sum_{i \in B^{(is)}} S_{Gi,max}^{(is,st)} \geq \sqrt{\left(\sum_{i \in B^{(is)}} P_{Loi}^{(is,st)} \right)^2 + \left(\sum_{i \in B^{(is)}} Q_{Loi}^{(is,st)} \right)^2} + S_{loss\,\&\,spare}^{(is,st)} \tag{5.6}$$

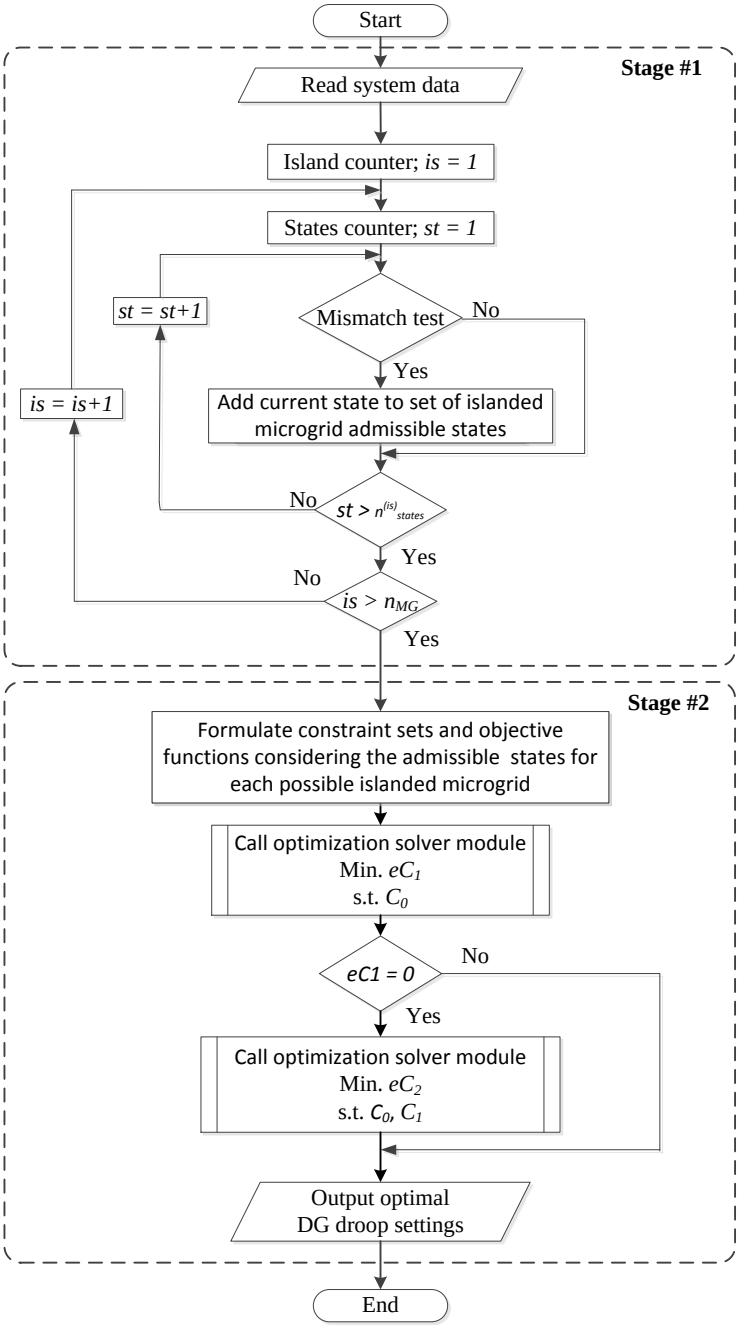

Figure 5.2: Flowchart of the proposed algorithm

where *is* is the index of islanded microgrids, *st* is the index of state, $B^{(is)}$ is the set of all buses in islanded microgrid *is*, $S_{Gi,max}^{(is,st)}$ is the apparent power generation capacity at bus *i* when operating in islanded microgrid *is* at state *st*, $S_{loss\&spare}^{(is,st)}$ is the apparent power loss and spare capacity requirements for islanded microgrid *is* operating at state *st* and $P_{Loi,}^{(is,st)}$, $Q_{Loi,}^{(is,st)}$ are the active and reactive nominal load power at bus

i when operating in islanded microgrid *is* at state *st*, respectively. The condition in (5.6) shows that an islanded microgrid state is considered admissible if enough apparent power generation is available to match the island total load, power loss, and spare capacity requirements. The spare capacity defined in this stage is intended to account for the ability of the microgrid to respond to unexpected and sudden increases in its local power demand (i.e., spinning reserve) [41], [46]. Different options can affect the definition of spare capacity for an islanded microgrid. One option is to define the spare capacity to represent a specific percentage of the load demand. In this work, the spare capacity was arbitrarily defined as 5 % of the total demand in the microgrid [41]. It is worth mentioning that in this stage, the power loss in the island feeders is considered to be 5 % of the microgrid demand [46], [97].

5.4.2 Stage #2: constraint hierarchy approach

Although the choice of droop characteristics cannot lead to any reduction in the islanded microgrid customers' interruption caused by the islanded microgrid unsuccessful operation due to generation-to-load mismatch, a proper setting of droop characteristics can minimize the customers' interruption resulting from the violation of voltage constraints. In this stage, the droop settings are thus optimally selected to minimize customer interruption due to voltage regulation and security issues taking into consideration all admissible states of each possible islanded microgrid. The problem is divided into two steps: the first is to satisfy the operational voltage regulation constraints at the different system buses, and the second is to increase the voltage security margin. In this work, the theory of constraint hierarchy is applied as a means of performing these steps.

The theory of constraint hierarchy was originally defined in [100]. A constraint hierarchy consists of a multiset of labeled constraints, each identified as either mandatory or preferred. The mandatory constraints must hold for any valuation of the system-free variables. The preferred constraints should be satisfied as fully as possible. An arbitrary number of preference levels are permitted for the preferred constraints, with each successive level being weaker than its predecessor. For a given constraint hierarchy *C*, C_0 is the set of mandatory constraints in *C*, with strength *0* always reserved for the mandatory constraints. For n_{levels} levels of preferences, C_p, with $p \in \{1,2,\ldots,n_{levels}\}$, denotes the sets of preferred constraints. A solution *z* to a given constraint hierarchy *C* is a specific valuation of the system-free variables. A solution that satisfies all the mandatory constraints in the hierarchy is called an admissible solution. Z_0 is the set of all possible admissible solutions to *C*.

$$Z_0 = \{z \mid \forall c_0 \in C_0, c_0(z) holds\} \tag{5.7}$$

The set of preferred constraints that each admissible solution in Z_0 also satisfies, respecting their strength level, is used for the selection of the best solution from Z_0. A best solution is one compared to which no

better solution exists. To determine the best solution in Z_0, an error function $eC_p(z)$ is defined for each of the preferred constraint levels. This function returns a non-negative real number that indicates how closely C_p is satisfied for a valuation z, such that $eC_p(z) = 0$ if and only if $C_p(z)$ is satisfied. A solution z_a is better than another solution z_b, if for each level l through some level $p-1$, $eC_l(z_a)$is equal to $eC_l(z_b)$, and also at level p it is strictly less:

$$z_a \text{ is better than } z_b \equiv \exists p > 0 \mid \left(eC_l(z_a) = eC_l(z_b), \forall l \in \{1,\ldots,p-1\}\right) \wedge \left(eC_p(z_a) < eC_p(z_b)\right) \tag{5.8}$$

The constraint hierarchy is built level by level from the constraints of the highest preference in the hierarchy down to those with lower ones. For example, if all C_p constraints can be satisfied, then C_{p+1} (weaker than C_p) will be added to the constraint hierarchy, following which the satisfaction of C_{p+1} can then be checked in turn.

Figure 5.3 illustrates the establishing of the constraint hierarchy for the problem under study. The outer space shown in Figure 5.3 contains the set of solutions Z_0 that satisfy the bounds of the droop settings and the hard constraints of the system at each admissible state for each possible islanded microgrid (i.e., power flow equations as well as generation and line capacity limits). Each solution in Z_0 has a specific ability to minimize islanded microgrid customer interruptions that result from the violation of voltage regulation constraints. An inner subspace Z_1 might thus be defined as the solution domain in which all solutions satisfy the voltage regulation constraints (i.e., no customer interruptions due to a voltage regulation problem). If Z_1 exists, then another sub-space Z_2 is defined so that the system voltage security constraints are satisfied (i.e., $Z_2 \subseteq Z_1 \subseteq Z_0$).

Sustained voltage levels that fall outside the specified voltage regulation constraints result in the unsatisfactory operation of utilization equipment. The operational status of individual load points in particular is determined based on the designed undervoltage/overvoltage protection schemes. However, even if the load points do not have their own protection devices, due to their unsatisfactory operation in the case of a voltage violation, they should be accounted for as interrupted loads [46]. It is worth noting here that consideration of the voltage regulation constraints in the C_0 level might result in an infeasible problem if any load point, at any admissible state of any possible islanded microgrid, is subject to a voltage violation. In this work, the voltage regulation constraint has therefore been defined as the first level of the hierarchy constraint problem. In this level, the proposed algorithm attempts to satisfy the voltage regulation constraints by minimizing the number of voltage violation incidents in the possible islanded microgrids, as given by the error function eC_1. The best solution for this constraint level can hence be found by solving the following optimization problem:

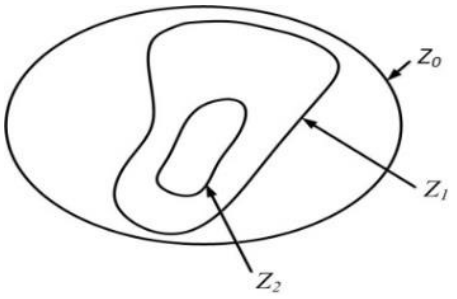

Figure 5.3: Conceptual illustration of the constraint hierarchy theory

$$Min.. \qquad eC_1 \equiv \sum_{is}^{n_{MG}} \left(\sum_{st}^{n_{states}^{(is)}} \left(\sum_{i \in B^{(is)}} \Gamma_i^{(is,st)} \times \Delta V_i^{(is,st)} \right) \right) \tag{5.9a}$$

Subject to:

$$C_0 \begin{cases} F^{(is,st)}(h^{(is,st)}, x) = 0 & (5.9b) \\ x_{lb} \le x \le x_{ub} & (5.9c) \\ I_{ik}^{lb} \le I_{ik}^{(is,st)} \le I_{ik}^{ub} & (5.9d) \\ 0 \le S_{Gj,max}^{(is,st)} - P_{Gj}^{(is,st)} \perp \dfrac{1}{x_j(2)} \times (x_j(1) - \omega^{(is,st)}) - P_{Gj}^{(is,st)} \ge 0 & (5.9e) \\ 0 \le \sqrt{\left(S_{Gj,max}^{(is,st)}\right)^2 - \left(P_{Gj}^{(is,st)}\right)^2} - Q_{Gj}^{(is,st)} \perp \dfrac{1}{x_j(4)} \times \left(x_j(3) - \left|V_j\right|^{(is,st)} \right) - Q_{Gj}^{(is,st)} \ge 0 & (5.9f) \end{cases}$$

$$\forall is \in \{1,2,\ldots,n_{MG}\}, \forall st \in \left\{1,2,\ldots,n_{states}^{(is)}\right\}, \forall j \in B_{droop}^{(is)} \quad \& \forall i,k \in B^{(is)}$$

where n_{MG} is the number of possible islanded microgrids in the system under study, $n_{states}^{(is)}$ is the number of islanded microgrid *is* states, $B_{droop}^{(is)}$ is the set of all droop-controlled buses in islanded microgrid *is*, $\Gamma_i^{(is,st)}$ is a parameter indicating the priority of load point *i* when operating in islanded microgrid *is* at state *st*, $h^{(is,st)}$ is the vector of state variables of islanded microgrid *is* operating at state *st* including system frequency, voltage magnitudes, and angles, $I_{ik}^{(is,st)}$ is the magnitude of the current flowing in the line between buses *i* and *k* when operating in islanded microgrid *is* at state *st*, and $\Delta V_i^{(is,st)}$ is a binary variable indicating the voltage regulation status of load point *i* when operating in islanded microgrid *is* at state *st*. ΔV_i equals zero when the voltage at the load point is within the voltage regulation constraints and equals one otherwise. The variables in the minimization problem given by (5.9a) are the unknown DG units droop parameters settings and the power flow variables for each admissible state of each possible islanded microgrid. The equality constraints in (5.9b) represent the set of islanded microgrid power flow equations

for each admissible state of each possible islanded microgrid. The upper and lower bounds on the droop parameters settings given by (5.9c) are determined based on the allowable voltage and frequency regulation at the DG units PCCs [20]. Equations (5.9d)-(5.9f) represent the line currents and the capacity constraints of the droop-controlled DG units for each admissible state of each possible islanded microgrid and the relationships governing the j^{th} droop-controlled DG unit active and reactive power generation capabilities can be given as :

$$P_{Gj,max}^{(is,st)} = S_{Gj,max}^{(is,st)} \tag{5.10}$$

$$Q_{Gj,max}^{(is,st)} = \sqrt{\left(S_{Gj,max}^{(is,st)}\right)^2 - \left(P_{Gj}^{(is,st)}\right)^2} \tag{5.11}$$

As it was shown in chapter 4, the overall operational limit of the microgrid can be closely associated with the voltage stability of the network. Hence, the incorporation of the voltage collapse criterion in the selection of the droop settings is important for maximizing the distance from the operating point to the point of voltage collapse, which in turn, increases the robustness of the system with respect to withstanding possible contingencies. The voltage security margin quantifies the proximity of an islanded microgrid state to the point of voltage collapse. Accordingly, in this work the second level of the constraint hierarchy attempts to maximize the voltage security margin through the minimizing of the difference between the islanded microgrid maximum loading margin and its respective upper bounds, given by the error function eC_2. The best solution for this constraint level can hence be found by solving the following optimization problem:

$$\textit{Min.} \qquad eC_2 \equiv \sum_{is}^{n_{MG}} \left(\sum_{st}^{n_{states}^{(is)}} \Gamma^{(is,st)} \times \left(\lambda_{ub}^{(is,st)} - \lambda^{(is,st,m)} \right) \right) \tag{5.12a}$$

Subject to:

$$C_0 \begin{cases} F^{(is,st,\ell)}(h^{(is,st,\ell)}, x, \lambda^{(is,st,\ell)}) = 0 & (5.12b) \\ x_{lb} \le x \le x_{ub} & (5.12c) \\ I_{ik}^{lb} \le I_{ik}^{(is,st,\ell)} \le I_{ik}^{ub} & (5.12d) \\ 0 \le S_{Gj,max}^{(is,st,\ell)} - P_{Gj}^{(is,st,\ell)} \perp \dfrac{1}{x_j(2)} \times (x_j(1) - \omega^{(is,st,\ell)}) - P_{Gj}^{(is,st,\ell)} \ge 0 & (5.12e) \\ 0 \le \sqrt{\left(S_{Gj,max}^{(is,st,\ell)}\right)^2 - \left(P_{Gj}^{(is,st,\ell)}\right)^2} - Q_{Gj}^{(is,st,\ell)} \perp \dfrac{1}{x_j(4)} \times \left(x_j(3) - \left|V_j\right|^{(is,st,\ell)} \right) - Q_{Gj}^{(is,st,\ell)} \ge 0 & (5.12f) \end{cases}$$

$$C_1 \quad \left\{ \left|V_i\right|^{lb} \le \left|V_i\right|^{(is,st,\ell)} \le \left|V_i\right|^{ub} \right. \tag{5.12g}$$

$$\forall is \in \{1,2,\ldots,n_{MG}\}, \forall st \in \left\{1,2,\ldots,n_{states}^{(is)}\right\}, \forall \ell \in \{c,m\}, \ \forall j \in B_{droop}^{(is)} \ \& \forall i,k \in B^{(is)}$$

where ℓ is the index of system loading points, *c* and *m* indicate the current and maximum loading points, respectively, $\Gamma^{(is,st)}$ is a parameter indicating the priority of islanded microgrid *is* at state *st*, $\lambda^{(is,st,\ell)}$ is the loading factor of islanded microgrid *is* at state *st* for loading point ℓ and $\lambda_{ub}^{(is,st)}$ is the upper bound on the loading factor of islanded microgrid *is* at state *st* and given by

$$\lambda_{ub}^{(is,st)} = \sum_{i \in B^{(is)}} S_{Gi,max}^{(is,st)} \Bigg/ \left(\sqrt{\left(\sum_{i \in B^{(is)}} P_{Li}^{(is,st)} \right)^2 + \left(\sum_{i \in B^{(is)}} Q_{Li}^{(is,st)} \right)^2} \right) \tag{5.13}$$

5.5 Case studies

The proposed probabilistic approach was coded in a Matlab environment. The optimization problems in (5.9) and (5.12) were solved using an interior point method. The complementary constraints were transformed to nonlinear constraints using a Fischer-Burmeister-based method [56], [95]. The 33-bus balanced test system is used in the case studies [96]. Figure 5.4 shows a single-line diagram of the test system with the two possible islanded microgrids that can be formed by the two IIDs. The system feeder parameters (at nominal frequency) and load power are given in Appendix A. Four dispatchable DG units and two wind-based DG units were allocated to feed the system in islanded microgrid operation mode. The ratings, locations, and types of the DG units are listed in Table 5.1. The upper and lower limits on the variation in node voltage were taken as 1.05 p.u. and 0.95 p.u., respectively. A maximum frequency variation of ± 0.005 p.u. was considered in the case studies investigated. For this work, the load was divided into ten states using the clustering technique developed in [101]. Table 5.2 shows the set of load levels as a percentage of the peak load, and its corresponding probabilities [97]. The wind-speed profile was estimated from the previous historical data, based on which the 12-state model developed in [97] was used, including the generated power and probabilities for each wind turbine. Table 5.3 shows the wind speed levels, and their respective probabilities for each wind turbine [97]. The set of load states was combined with the set of wind power states for each wind turbine in order to extract the generation-load model of each islanded microgrid [97]. Two case studies were considered as a means of evaluating the relevance of the proposed algorithm. The first case study is an examination of the operation of an islanded system with conventional droop settings. The second case study is an investigation of the operation of the system when the droop settings are optimally selected according to the proposed algorithm.

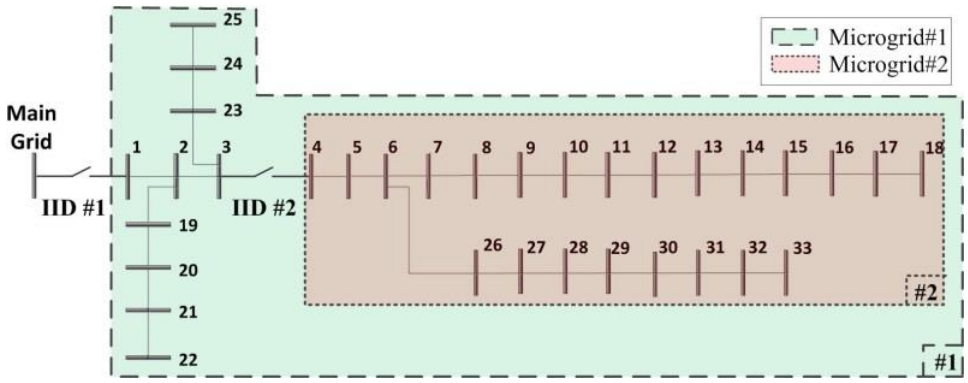

Figure 5.4: Test system with two IIDs (case study# 5-1 and # 5-2)

Table 5.1: Case study# 5-1 and # 5-2: DG locations, ratings, and control modes in the 33-bus test system (S_{base} = 1 MVA)

DG #	Bus #	S_{Gmax} *(p.u.)*	Type	Mode
1	04	3.00	Dispatchable	Droop
2	08	0.50	Dispatchable	Droop
3	18	0.75	DFIG Wind	PQ-0.95 PF Lead
4	22	1.50	Dispatchable	Droop
5	24	0.50	DFIG Wind	PQ-0.95 PF Lead
6	25	1.00	Dispatchable	Droop

Table 5.2: Case study# 5-1 and # 5-2: load states model

Percentage of Peak load (%)	100	85.3	77.4	71.3	65	58.5	51	45.1	40.6	35.1
Probability	0.01	0.056	0.1057	0.1654	0.1654	0.163	0.163	0.0912	0.0473	0.033

Table 5.3: Case study# 5-1 and # 5-2: wind states model

Wind speed limits (m/sec)	0 to 4	4 to 5	5 to 6	6 to 7	7 to 8	8 to 9	9 to 10	10 to 11	11 to 12	12 to 13	13 to 14	14 to 25
Probability	0.073	0.024	0.032	0.044	0.046	0.075	0.089	0.109	0.101	0.109	0.062	0.236

5.5.1 Case study# 5-1: conventional droop settings

In case study# 5-1, the static droop gains of the DG units are designed in order to share the load demand of the islanded microgrid proportionally with the rated capacity of the DG units [20]; V^* and ω^* are selected arbitrarily in order to maintain adequate power-quality levels, in terms of maintaining the frequency and voltage within their respective specified operating limits. Such conventional droop settings are capable of providing proper frequency regulation and nearly exact active power sharing among DG units in islanded microgrids [68]. Using the conventional droop settings, the islanded microgrid power flow algorithm given in chapter 3 is solved for all admissible islanded microgrid states (with $\omega^* = 1.0$ p.u. at different values of V^*). Figures 5.5 (a) and 5.5 (b) show the minimum and maximum voltages,

respectively, that can occur at the different system buses considering all possible islanded microgrids that can be initiated to include such buses as well as all possible generation and load states of such islands, with different arbitrary values of V^*. The figures show that the choice of V^* can significantly affect islanded microgrid voltage regulation. An arbitrary choice of V^* can lead to undervoltage and/or overvoltage problems. Further, when all DG units have the same V^* setting, the change in such a value cannot guarantee effective voltage regulation for all possible operating states. On the other hand, arbitrary selection of different V^* settings for different DG units is not an easy task, given the presence of intermittent renewable power sources and the fact that the voltage profile does not follow a consistent descending trend towards the feeder terminal. Avoiding such improper voltage regulation renders the arbitrary choice of different V^* values for DG units cumbersome, and they need thus to be selected optimally.

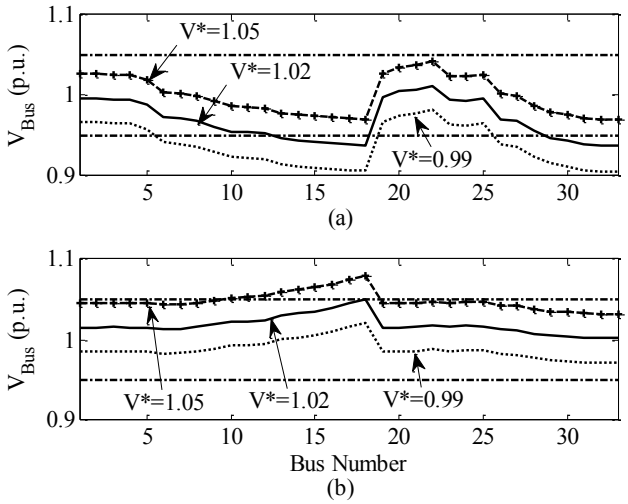

Figure 5.5: Case study# 5-1: (a) minimum and (b) maximum voltage magnitude for all buses at different values of V^* using conventional droop settings considering all admissible system states and all possible islanded microgrids (In this case study, all droop-controlled DG units operate at the same V^* setting)

5.5.2 Case study# 5-2: proposed optimal droop settings

In this case study, three possible scenarios are considered. In the first scenario, the proposed algorithm is applied for optimally selecting the no-load nominal voltage and frequency droop settings (i.e., V^* and ω^*) for the different droop-controlled DG units. In this scenario, the static droop gains are not optimized and are kept proportional to the capacities of the DG units as in case study #1. Table 5.4 lists the optimal V^* and ω^* settings for droop-based DG units obtained in this scenario. Figure 5.6 shows the minimum and maximum voltages based on consideration of all admissible system states and all possible microgrids when operating with the optimal settings obtained in this scenario. The results obtained in the first scenario show that the optimal choice of V^* and ω^* cannot guarantee the satisfaction of the system voltage operational constraints given in C_1. Based on the proposed two-level hierarchy constraint algorithm, because the C_1 constraints are not satisfied, the results obtained in this scenario are optimal only in terms of the error function eC_1. Consequently, the values obtained for V^* and ω^* are not based on consideration of the voltage instability proximity expressed by the error function eC_2.

In the second scenario, the proposed two-level hierarchy constraint algorithm optimally selects all the droop settings for the different DG units in the system (i.e., V^*, ω^*, m_p, and n_q). The third scenario investigates the importance of including consideration of the maximum loadability of the system in the optimal selection of the system droop parameters. Accordingly, in the third scenario, the proposed algorithm is thus limited to consideration of only the C_0 and C_1 levels in the constraint hierarchy. Table 5.4 show the settings obtained in the second and third scenarios. Here it is worth noting that the valuation of the optimization variables obtained in the third scenario is not unique and that other variable valuations can satisfy the problem constraints. Figures 5.7(a) and 5.7(b) show the minimum and maximum voltages that can occur at the different system buses in the second and third scenarios, respectively, considering all admissible system states, as well as all possible islanded microgrids that can be initiated to include such buses. As can be seen in Figures 5.7(a) and 5.7(b), the droop settings obtained in the second and third scenarios are both capable of satisfying the operational voltage constraints for the different system states given by C_1.

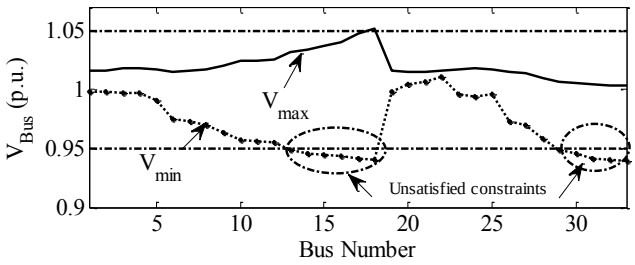

Figure 5.6: Case study# 5-2: minimum and maximum voltage magnitudes with the settings obtained in the first scenario

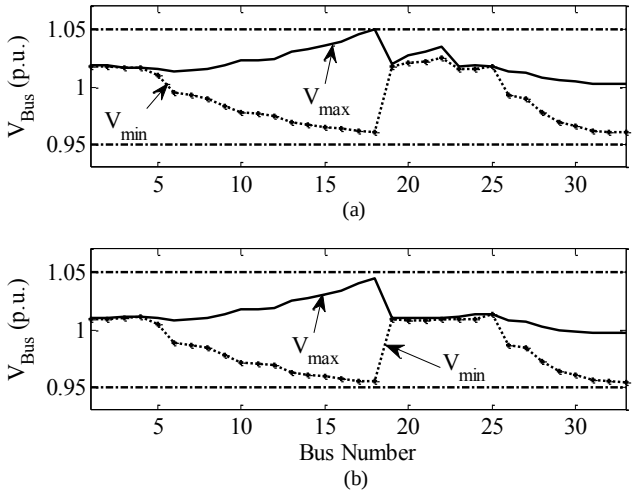

Figure 5.7: Case study# 5-2: minimum and maximum voltage magnitudes with the settings obtained in the (a) second and (b) third scenarios

Table 5.4: Case study# 5-2: optimal droop settings obtained in the three scenario under consideration

DG #	**Scenario #1**			
	V^*	w^*	m_p	n_q
1	1.024	1.0018	1.67E-03	1.67E-02
2	1.017	1.0016	1.00E-02	1.00E-01
4	1.016	1.0014	3.33E-03	3.33E-02
6	1.017	1.0014	5.00E-03	5.00E-02
DG #	**Scenario #2**			
	V^*	w^*	m_p	n_q
1	1.016	1.0009	7.29E-04	1.65E-05
2	1.016	1.0008	4.03E-03	6.17E-02
4	1.04	1.0009	1.22E-03	3.21E-02
6	1.018	1.001	2.47E-03	5.09E-04
DG #	**Scenario #3**			
	V^*	w^*	m_p	n_q
1	1.011	1.0001	3.59E-04	1.30E-05
2	1.011	1	1.88E-03	1.86E-02
4	1.011	1	2.05E-03	2.57E-02
6	1.013	1.0001	1.02E-03	5.32E-05

Figure 5.8 shows the PDFs of the system frequency for the second and third scenarios. As shown in the figure, the lower and upper bounds imposed on the static droop coefficients by equations (5.9c) and (5.12c) guarantee the maintenance of the system frequency within the allowable deviation tolerance. It is worth noting that similar bounds imposed on the reactive power static droop gain coefficients can ensure proper voltage regulation only at the PCC. Voltage drops across the distribution feeders may still lead to voltage violations at different system buses.

Figures 5.9 (a) to 5.9(d) show the maximum system loadability at different wind-power ratios (ratio of the available wind power over the rated wind power capacity) in the second and third scenarios for islanded microgrid #1 and islanded microgrid #2. Two sets of results are plotted in each figure: those labeled "without V_{limit}" represent the maximum system loadability when no bus voltage limits are enforced at the maximum loading point, and the results labeled "with V_{limit}" represent the maximum system loadability when the bus voltage limits are enforced at the maximum loading point. For both sets of results, the line capacity limits and the active and reactive power limits of the DG units are always enforced. As one would expect, the presence of bus voltage limits at the maximum loading point reduces the loadability margin of the islanded systems. These figures also demonstrate that the maximum loadability achieved with the settings obtained in the second scenario is significantly higher than that obtained with the settings from the third scenario. This in turn, indicates the importance of including consideration of the maximum loadability of the system, as given by C_2 in the proposed two-level hierarchy constraint algorithm. However, Figures 5.9(b) and 5.9(d) show that the maximum loadability of islanded microgrid #2 "without V_{limit}" with the settings obtained from the second and third scenarios almost coincide along the wind-power ratio trajectory. This particular observation can be attributed to the presence of a dominant DG unit (DG #1) in islanded microgrid #2, which results in the optimization of the droop settings having a reduced impact on the maximum loadability of the system.

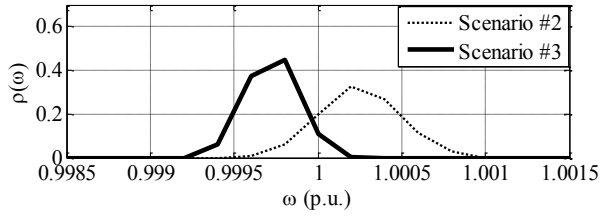

Figure 5.8: Case study# 5-2: PDFs of the system frequency with the settings obtained in the second and third scenarios

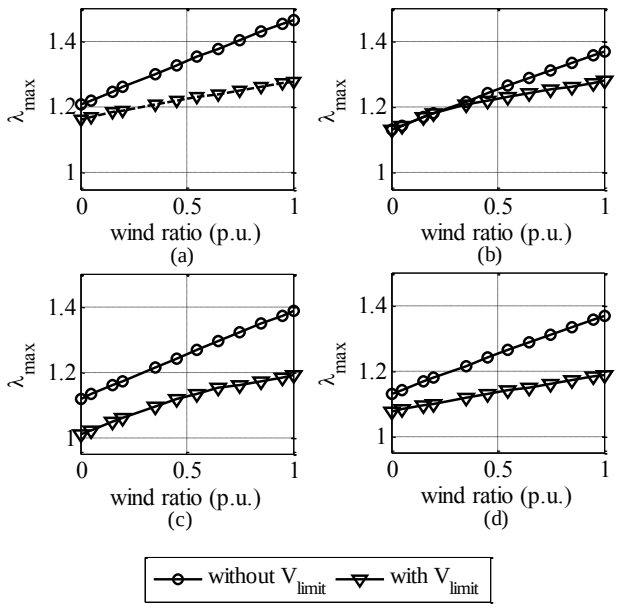

Figure 5.9: Case study# 5-2: maximum loadability with settings obtained in scenarios #2 and #3 at different wind power ratios: (a) microgrid #1, scenario #2, (b) microgrid #2, scenario #2, (c) microgrid #1, scenario #3 and (d) microgrid #2, scenario #3

Figures 5.10 and 5.11 show the DG units' generation as islanded microgrid #1 loading increase for the settings obtained in the second and third scenarios, respectively. As shown in Figures 5.10(a) and 5.11(a), the increase in active power generation with the increase in the system loading is governed by the droop relation for all the droop-controlled DG units in the system. In Figures 5.10(b) and 5.10(c), three system loading levels have been highlighted on the generation plots. At these loading levels, points "A", "B", and "C" correspond to the point at which maximum generation capacity is reached by DG #2, DG #1, and DG #6, respectively. For each of these points, as the DG unit reaches its maximum apparent power capacity, the reactive power production switches from being governed by the droop control to being governed by the available capacity as denoted by (5.11). This change, in turn, affects the reactive power generated by other DG units. For example, Figure 5.10(c) shows that at point "B", DG #1 and DG #2 are producing their maximum apparent power. A further increase in the loading factor from point "B" to point "C" hence results in a decrease in the reactive power production of DG #1 and DG #2 in order to preserve their active power-sharing capability. The increase in reactive power demands resulting from the loading factor increase and the reduction in reactive power production by DG #1 and DG #2 is therefore shared between DG #4 and #6. Given the respective values of the reactive power static droop gains of these DG units, it can be seen that DG #4 feeds a significantly higher portion of the reactive power demand increase. In Figures 5.11(b) and 5.11(c), similar system loading levels are highlighted.

Comparing the results obtained in Figures 5.10 and 5.11, it can be seen that the load sharing obtained by the settings from the second scenario allows for higher system loadability as compared with the settings from the third scenario. These results further demonstrate the ability of the proposed two-level hierarchy constraint algorithm to achieve higher system loadability.

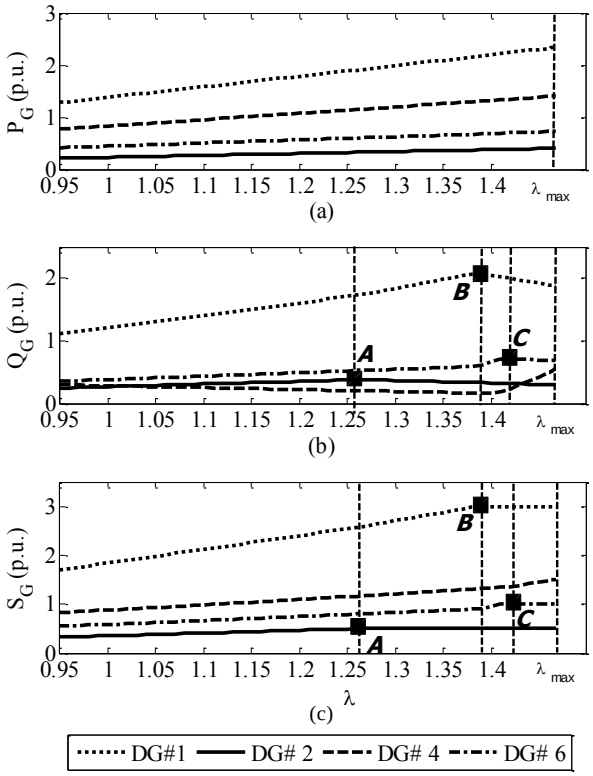

Figure 5.10: Case study# 5-2: DG units generation as λ increases with the settings obtained in scenario #2 for islanded microgrid #1: (a) active power, (b) reactive power, and (c) apparent power.

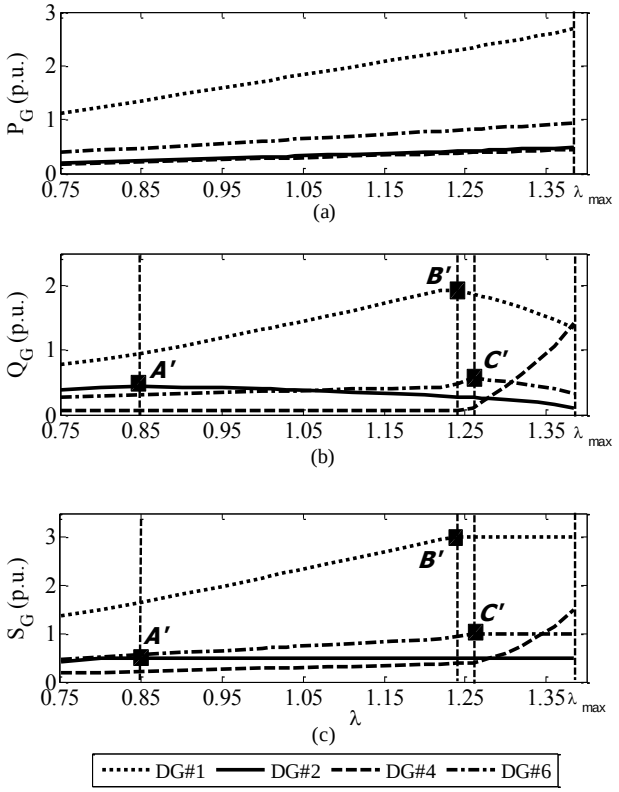

Figure 5.11: Case study# 5-2: DG units generation as λ increases with the settings obtained in scenario #3 for islanded microgrid #1: (a) active power, (b) reactive power, and (c) apparent power

The impact of voltage and generation capacity constraints on the maximum system loadability was analyzed: Figure 5.12 shows the voltage magnitude profile as a function of the system loadability (PV curve) for the most remote bus in islanded microgrid #1 (bus #33) with the settings obtained in the second scenario. Point "X" shows the maximum system loadability when both the voltage and generation capacity constraints are considered, point "Y" shows the maximum system loadability when only the generation capacity constraints are considered, and Point "Z" represents the maximum system loadability when the system is unconstrained. Points "X" and "Y" are LIB points, while point "Z" is an SNB point. The rapid descent in the voltage magnitude from point "B" to point "Y", also depicted in Figure 5.12, could be associated with the transfer of reactive power support from DG #1 to the remoter DG #4 and DG #6 as DG #1 reaches its maximum capacity at point "B". Figure 12 shows that the voltage and generation capacity constraints significantly reduce the loadability margin of the islanded microgrid.

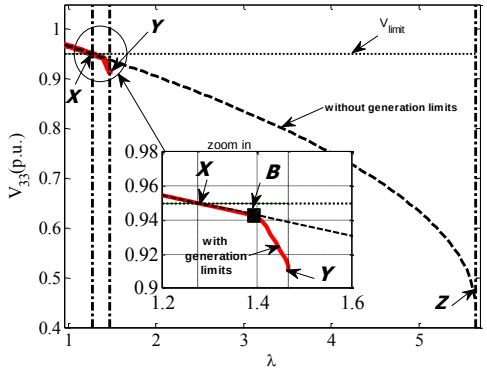

Figure 5.12: Case study# 5-2: voltage at bus #33 as a function of λ with the settings obtained in scenario #2 for islanded microgrid #1

5.6 Discussion

This chapter proposed a new probabilistic algorithm for the offline selection of DG units droop parameters settings for a possible operational planning horizon within which islanded microgrids might be initiated. The proposed algorithm applies a detailed islanded microgrid model along with a probabilistic analytical technique to account for special islanded microgrid features and the variability in system generation and demand. The algorithm also includes consideration of different possible islanded microgrid configurations that can be initiated in the distribution network. A constraint hierarchy approach is incorporated as a means of minimizing islanded microgrid customer interruption, first by satisfying operational system constraints and second by enhancing voltage security margins. Simulation studies have been carried out to demonstrate the effectiveness of the proposed algorithm. The results reveal that the proposed algorithm is capable of significantly reducing islanded microgrid customer interruptions as well as enhancing the islanded microgrids voltage security margins. The findings also show that an effective selection of droop parameters settings will facilitate the successful implementation of the islanded microgrid concept in distribution networks.

Chapter 6

A Multi-Stage Centralized Control Scheme for Islanded Microgrids with High PEV Penetration

6.1 Introduction

Vehicles electrification has been recently considered as one of the smart grid objectives. The widespread of PEVs will reduce fuel consumption and harmful gases emissions. However, without appropriate coordination such widespread of vehicle electrification can hinder the application of the microgrid concept [102]. This chapter proposes a new multi-stage control scheme using a MGCC for the operation of islanded microgrids in the presence of high PEV penetration. The proposed control scheme optimally coordinates the DG units' droop characteristics, the shedding of islanded microgrid power demand (during inadequate generation periods) and the PEVs charging/discharging decisions. To this end, a three-stage droop-based optimal power flow problem is formulated in order to: 1) minimize the load shedding, 2) satisfy the PEVs customers' requirements and 3) minimize the microgrid cost of operation. The proposed control scheme takes into consideration; 1) the special features and operational philosophy of droop-controlled islanded microgrid systems; 2) the variability associated with the output power of renewable DG units and 3) the random behavior of PEV charging. The remainder of this chapter is organized as follows: section 6.2 briefly discusses the islanded microgrid energy management architecture in the presence of PEVs. In section 6.3 the proposed multi-stage centralized control scheme is introduced. Section 6.4 presents several case studies to show the effectiveness and robustness of the proposed control scheme. The simulation studies show that the proposed control scheme can enhance the operation of islanded microgrid systems and facilitate a successful implementation of the islanded microgrid concept in the presence of high PEV penetration. In section 6.5 the chapter is concluded and its main contributions are discussed.

6.2 Microgrid energy management architecture

The anticipated high penetration of PEVs mandates the integration of the PEVs charging/discharging decisions in the energy management architecture of the islanded microgrid systems. It can be shown that such integration will provide flexibility to the islanded microgrid operation. Figure 6.1 shows the framework of a microgrid energy management system in islanded mode of operation. The islanded

microgrid energy management system is implemented in two levels: a MGCC and local controllers. The two levels of control are linked via a two ways communication network. The communication network is required for information flow and control signals communication. The MGCC performs two main functions; namely; 1) data acquisition and forecasting, and 2) optimization. The data acquisition and forecasting functionality is achieved by periodically collecting data about the status of renewable power generation and load consumption. Moreover, in the presence of PEVs charging stations, the MGCC receives data about the PEVs in the system. Along with the on-line collected data, the MGCC incorporates historical power consumption and weather patterns to provide an appropriate forecast of the islanded microgrid power demand and renewable power generation. On the other hand, the objective of the optimization function in the MGCC is to optimally manage the islanded microgrid energy requirements by coordinating the operation of the islanded microgrid local controllers including DG units' local controllers as well as PEVs chargers. Moreover, the MGCC optimization function is designed to ensure service reliability to a diverse combination of loads with different priority factors. As such, the microgrid loads are classified according to their priority that depends on the nature of demand. During emergency operation of islanded microgrids, with insufficient generation to meet the total microgrid demand, the MGCC is designated to control the set of least priority loads by shedding them as and when necessary. The optimal management of the islanded microgrid resources and requirements in the presence of high PEV penetration is the main subject of this chapter.

As shown in Figure 6.1, an aggregator is assumed to be in place to deal with the PEVs data collection and storage. The aggregator role is to collect the required information from the smart charging units of the existing PEVs and send it to the MGCC. At time instant *t*, an aggregator connected to bus *i*, has $N_{PEV}^{i}(t)$ vehicles connected to it, where $i \in \{1,2 \ldots n_{bus}\}$. Upon arrival, the driver of each vehicle, *vh*, provides the aggregator with the vehicle departure time $t_d^i(vh)$, its required state of charge (SOC) at departure $SOCR^i(vh)$, and the minimum allowed SOC for this vehicle $SOC_{min}^{i}(vh)$. The aggregator sends these data along with the vehicle initial SOC, $SOCI^i(vh)$, to the MGCC. Figure 6.1 also shows that renewable energy resources are locally controlled to track their maximum power point (MPPT control mode). On the other hand energy buffering is obtained from dispatchable DG units operating in droop control mode [98], [99].

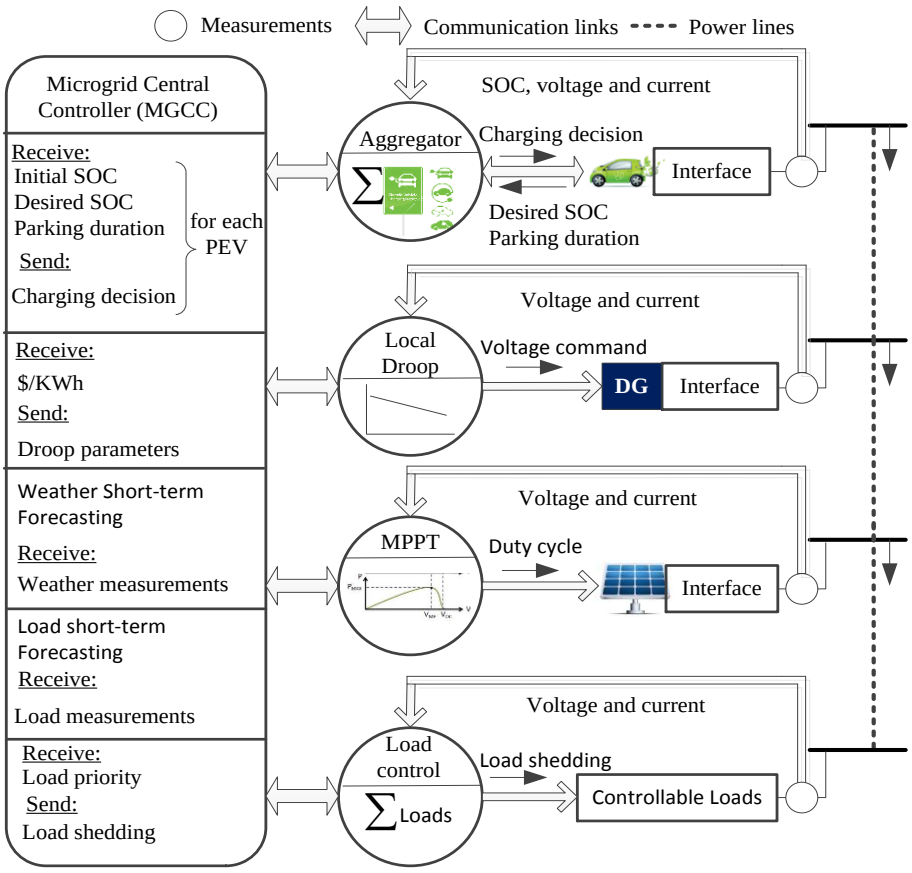

Figure 6.1: schematic diagram of islanded microgrid energy management architecture

6.3 Proposed multi-stage centralized control scheme

The main objective of the MGCC is to ensure a reliable power supply to the microgrid customers with minimum operation costs. In islanded mode of operation, a higher priority is given to the customers' service continuity. This entails: first minimizing the regular load shedding and second maximizing the PEVs customers' satisfaction. Accordingly, a three-stage sequential droop-based OPF problem is formulated based on the priority of the MGCC objectives. Each stage is a sub-problem with a single objective and some constraints. The first sub-problem aims to minimize the downtime or load shedding when the available power in the islanded microgrid is not enough to feed its local loads. The first sub-problem is referred to as the load shedding minimization sub-problem (LSMSP). The second sub-problem, referred to as SOC maximization sub-problem (SMSP), aims to maximize the PEVs customers' satisfaction. The third problem is the cost minimization sub-problem (CMSP). The three sub- problems are solved sequentially with the optimal objective value obtained for each sub-problem set as a constraint

in its subsequent sub-problem. The three sub-problems are not solved simultaneously to avoid having lower priority objectives interfering with achieving the optimal solution of higher priority goals. For instance, the minimization of system generation cost should not interfere with maximizing PEV customer satisfaction.

The proposed three-stage sequential droop-based OPF problem accounts for the random behavior of the PEVs characteristics as well as the uncertainty of renewable power generation and the variations of power demand. To this end, the multi-stage optimization problem is solved over a future finite prediction time-horizon τ. The length of τ is determined based on the possible accurate short-term forecasting that can be obtained for renewable power generation, the parking duration of PEVs and the PEVs charging rate. The prediction horizon τ is discretized into N_p timeslots of equal duration Δt, where $N_p = \tau/\Delta t$. The length of each timeslot Δt is determined based on the required periodic execution of the droop-based OPF problem (i.e. required periodic update of the control settings) in order to guarantee a proper dispatch. As depicted in Figure 6.2, for a prediction horizon τ starting at t_u, the MGCC starts collecting the measured and the forecasted data at t_u-Δt, where $u \in U_{opt}$ with U_{opt} denoting the vector of islanded microgrid optimization events. The MGCC solves the three-stage droop-based OPF problem over τ to get the optimal control settings at every time step $t_u + k_t \times \Delta t, \forall k_t \in \{0,1\ldots,N_p\}$. Here it is noteworthy that there is no prediction applied for future PEVs arrival and the optimization is executed over τ based on the existing PEVs at t_u-Δt.

If there were no uncertainty in the forecasted data and there were no arrival of PEVs within the prediction horizon, one could apply the control sequence obtained from the optimization problem at all time steps within the prediction horizon. However, due to the uncertainty of forecasted data and the random behavior of PEVs, the true system behavior is different from the predicted behavior. In order to allow for the incorporation of the feedback information about the true system state, computed optimal control settings are implemented only until the next optimization event. Therefore, only the optimal control settings obtained for the time step t_u are implemented. The optimal control settings for other time steps pertaining to τ are used as initial conditions for the next dynamic optimization execution starting at time instant t_u, at which the MGCC receives updated measurements and forecasted data and the computation is repeated for a new time horizon starting at t_u+Δt. This in turns alleviates the power fluctuations in response to any forecasting error of data as well as the arrival of PEVs within the prediction time horizon. The main advantage of this approach is that it allows the current timeslot to be optimized while keeping

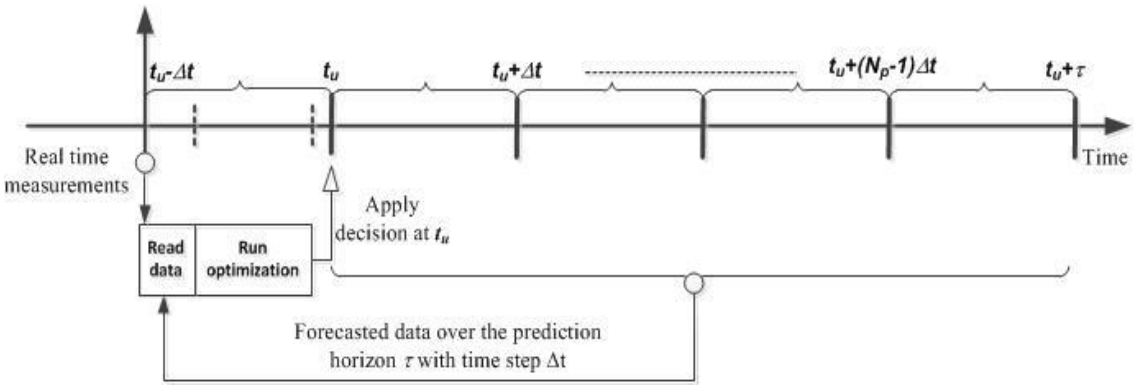

Figure 6.2: The periodic execution of the proposed multi-stage algorithm

future timeslots in account. Hence, optimal droop parameters of the DG units, scheduling of charging/discharging decisions of PEVs and load shedding scheduling can be achieved.

Load shedding schemes disconnects selected electrical loads in order to reduce the overall system power demand so as to match the available power generation. Unlike the grid-connected mode of operation, where the microgrid can get support from the main grid in case of inadequate microgrid generation, in islanded microgrids there is no external generation support available. Accordingly, shedding electrical loads in response to inadequate generation is vital to the continued stable operation of islanded microgrids. Therefore, to ensure service reliability of islanded microgrids during inadequate generation, a load shedding scheme is required. One of the load shedding schemes adopted in the literature is to disconnect the loads according to some pre-determined priority factors [103]. In case of insufficient islanded microgrid generation, it is important to shed loads of lower priority so that loads of higher priority can get continuous electrical supply. Thus, the MGCC has the right of load shedding of the lower priority load as and when necessary to balance the power in the islanded microgrid. Hence in this work, the objective of the first sub-problem is to maximize the islanded microgrid customers' reliability through minimizing the required load shedding in the system. The objective of the first sub-problem can be defined mathematically as follows,

$$Min. \quad \sum_{k_t=0}^{N_p} \sum_{i=1}^{n_{bus}} U_L^i(t_k) \times W_L^i \tag{6.1}$$

where

$$t_k = t_u + k_t \times \Delta t \tag{6.2}$$

$U_L^i(t_k)$ is a binary control variable that determines the operation state of the load at bus *i* at time instant t_k. $U_L^i(t_k) = 0$ means that the load is selected to be shed, otherwise it is fed. W_L^i is the priority factor of the load at bus *i*. W_L^i reflects the predetermined priority of the load depending on the critical nature of the load and its power rating.

The LSMSP should satisfy the power flow constraints for each bus $i \in \{1,2 \ldots n_{bus}\}$ at each time instant t_k, given by

$$P_{Gi}(t_k) = P_{Li}(t_k) \times U_L^i(t_k) + \sum_{vh}^{N_{PEV}^i(t_k)} P_{PEV}^i(t_k, vh) + \sum_{j=1}^{n_{bus}} \left(|V_i(t_k)||V_j(t_k)||Y_{ij}(t_k)| \cos\left(\theta_{ij}(t_k) + \delta_j(t_k) - \delta_i(t_k)\right)\right) \quad (6.3)$$

$$Q_{Gi}(t_k) = Q_{Li}(t_k) \times U_L^i(t_k) - \sum_{j=1}^{n_{bus}} \left(|V_i(t_k)||V_j(t_k)||Y_{ij}(t_k)| \sin\left(\theta_{ij}(t_k) + \delta_j(t_k) - \delta_i(t_k)\right)\right) \quad (6.4)$$

where $P_{Gi}(t_k)$ and $Q_{Gi}(t_k)$ denote the per unit active and reactive generated powers at bus *i* at time instant t_k, $P_{Li}(t_k)$ and $Q_{Li}(t_k)$ denote the per unit active and reactive regular power demands at bus *i* at time instant t_k, $P_{PEV}^i(t_k)$ is the per unit PEV consumed/delivered power by each vehicle *vh* connected to bus *i* at time instant t_k, $|V_i(t_k)|$ and $\delta_i(t_k)$ denote the per unit magnitude and angle of the voltage at bus *i* at time instant t_k, and $|Y_{ij}(t_k)|$ and $\theta_{ij}(t_k)$ are the per unit magnitude and angle of the frequency dependent bus-admittance matrix element between two buses *i* and *j* at time instant t_k, respectively.

As previously discussed in chapter 3, the generated active and reactive powers from a droop-controlled DG unit connected at bus *i* at time instant t_k can be given as follows:

$$P_{Gi}(t_k) = \frac{1}{m_{pi}(t_k)} \left(\omega_i^*(t_k) - \omega(t_k) \right) \quad (6.5)$$

$$Q_{Gi}(t_k) = \frac{1}{n_{qi}(t_k)} \left(V_i^*(t_k) - |V_i(t_k)| \right) \quad (6.6)$$

where $\omega_i^*(t_k)$ and $V_i^*(t_k)$ are the DG unit no-load nominal output voltage frequency and magnitude set points at time instant t_k, respectively. $m_{pi}(t_k)$ and $n_{qi}(t_k)$ are the active and reactive powers static droop gains at time instant t_k, respectively. In order to ensure proper selection of the DG units droop

characteristics, upper and lower bounds are imposed on the droop parameters by the inequality constraint given as

$$x_i^{lb} \le x_i(t_k) \le x_i^{ub} \tag{6.7}$$

where $x_j(t_k)$is the droop parameters of the droop-controlled DG unit connected to bus i at time instant t_k and it is defined as follows:

$$x_i(t_k)=[\ \omega_i^*(t_k),\ V_i^*(t_k),\ m_{pi}(t_k),\ n_{qi}(t_k)\ ] \tag{6.8}$$

The upper and lower bounds imposed on the droop setting parameters are determined based on the allowable voltage and frequency regulation at the DG unit PCC. The inequality constraint in (6.7) can ensure that the system frequency is within the allowable deviation tolerance (frequency is a global system variable). However it is noteworthy that such inequality constraint can only ensure proper voltage regulation at the DG units PCC. Still voltage drop across the distribution feeders may lead to voltage violation at different system buses [46]. The droop-controlled DG units' capacity constraints are given by:

$$0 \le S_{Gi,max} - P_{Gi}(t_k) \perp \frac{1}{m_{pi}(t_k)} \times (\omega_i^*(t_k) - \omega\ (t_k)) - P_{Gi}(t_k) \ge 0 \tag{6.9a}$$

$$0 \le \sqrt{\left(S_{Gi,max}\right)^2 - \left(P_{Gi}(t_k)\right)^2} - Q_{Gi}(t_k) \perp \frac{1}{n_{qi}(t_k)} \times \left(V_i^*(t_k) - |V_i(t_k)|\right) - Q_{Gi}(t_k) \ge 0 \tag{6.9b}$$

The generated power from a renewable DG unit connected at bus i at time instant t_k can be given as follows:

$$P_{Gi}(t_k) = P_{i,DG}(t_k), \qquad Q_{Gi}(t_k) = Q_{i,DG}(t_k) \tag{6.10}$$

where $P_{i,DG}(t_k)$and $Q_{i,DG}(t_k)$denote the forecasted renewable DG generated active and reactive powers at bus i at time instant t_k, respectively.

The consumed/delivered power $P_{PEV}^i(t_k, vh)$ by each vehicle vh connected to bus i at any time instant t_k depends on its charging decision, $D_{PEV}^i(t_k, vh)$, charger-battery transfer power limit $PCH^i(t_k, vh)$ and the charger efficiency $\eta^i(vh)$(charging and discharging efficiencies are assumed to be the same). For charging decisions with $D_{PEV}^i(t_k, vh) \ge 0$

$$P_{PEV}^i(t_k, vh) = \frac{D_{PEV}^i(t_k, vh) \times PCH^i(t_k, vh)}{\eta^i(vh)} \tag{6.11}$$

while for discharging decisions with $D^i_{PEV}(t_k, vh) < 0$

$$P^i_{PEV}(t_k, vh) = D^i_{PEV}(t_k, vh) \times PCH^i(t_k, vh) \times \eta^i(vh) \tag{6.12}$$

where,

$$D^i_{PEV}(t_k, vh) = \begin{cases} 0, & \forall t_k > t^i_d(vh) \\ [-1,1], & elsewhere \end{cases} \tag{6.13}$$

The charger-battery transfer power limit $PCH^i(t_k, vh)$ is function of the PEV battery SOC, which depends on the battery characteristics and the charger ratings. This limit has different characteristics for charging and discharging [104];

$$PCH^i(t_k, vh) = f_{CH}\left(SOC^i(t_k, vh)\right) \tag{6.14}$$

f_{CH} is a function representing the battery charging or discharging characteristics of vehicle *vh* connected to bus *i* at time instant t_k .. The *SOC* of vehicle *vh* connected to bus *i* at any time instant t_k should be between the minimum and required *SOCs* specified by the driver;

$$SOC^i_{min}(vh) \le SOC^i(t_k, vh) \le SOCR^i(vh) \tag{6.15}$$

Further, the SOC of a vehicle *vh* connected to bus *i* at any time instant t_k depends on its SOC at the preceding time step and its rate of charging/discharging

$$SOC^i(t_k, vh) = SOC^i(t_k - \Delta t, vh) + \frac{P^i_{PEV}(t_k, vh) \times \Delta t}{60 \times E^i(vh)} \tag{6.16}$$

where $E^i(vh)$ is the per unit PEV battery capacity.

Additionally, the voltage limits and thermal limits of the feeders should hold,

$$|V_i|^{lb} \le |V_i(t_k)| \le |V_i|^{ub} \tag{6.17}$$

$$|I_{ij}(t_k)| \le I^{ub}_{ij} \tag{6.18}$$

where $|V_i|^{lb}$ and $|V_i|^{ub}$ are the minimum and maximum allowable voltage magnitude limits, respectively. I_{ij} is the per unit branch current between buses *i* and *j*. I^{ub}_{ij} is the thermal capacity limit of the feeder between buses *i* and *j*.

Although the proposed droop-based OPF formulation can handle the short-term forecasting error and the unpredicted arrivals of PEVs at future time steps within τ , a very short-term forecasting error may persist at the first time step of the prediction horizon at which the control signals are implemented. Hence, a power reserve at each time-step is set by imposing:

$$\sum_{i=1}^{n_{bus}} S_{Gi,max}(t_k) \geq R \times \left[\sum_{i=1}^{n_{bus}} S_{Li}(t_k) + \sum_{i=1}^{n_{bus}} S_{PEV}^{i}(t_k) + S_{loss}(t_k) \right] \tag{6.19}$$

where $S_{Gi,max}(t_k)$ is the available generation capacity at bus *i* at time instant t_k, *R* is a coefficient to account for the system power reserve requirements, where the reserve is determined based on the very-short term forecasting accuracy of renewable DG units (i.e. power fluctuations within Δt) and the system primary reserve requirements. $S_{Li}(t_k)$ is the apparent power load demand at bus *i* at time instant t_k, , $S_{PEV}^{i}(t_k)$ is the apparent power PEV demand at bus *i* at time instant t_k, and $S_{loss}(t_k)$ is the total system losses at time instant t_k. The allocated reserve leaves adequate generation margin to deal with power fluctuation owing to forecasting error that otherwise may lead to inadequate generation at the first time step of the prediction horizon.

Hence the LSMSP can be solved by minimizing (6.1) subject to (6.3)-(6.19) $\forall k_t \in \{0,1\ldots,N_p\}$ and the control and state variables $x_{LSMSP}(t_k)$ in the LSMSP can be given as:

$$x_{LSMSP}(t_k) = \begin{cases} Control\,variables: \\ U_L^i(t_k), D_{PEV}^i(t_k, vh),\ x_i(t_k) \\ State\,variables: \\ \omega(t_k), V_i(t_k), Y_{ij}(t_k), SOC^i(t_k, vh), PCH^i(t_k, vh) \end{cases} \tag{6.20}$$

Solving the LSMSP yields the minimum load shedding that can be achieved at each time step t_k, given by $U_{L,LSMSP}^{i}(t_k)$. The SMSP aims to find alternative PEV charging/discharging decisions and DG droop parameters that can satisfy the feasible target load shedding achieved in the LSMSP while at the same time maximizing the PEV customer satisfaction. The PEV customers' satisfaction can be achieved by minimizing the SOC deviation from the required SOC. The SMSP can accordingly be formulated as follows:

$$Min. \quad \sum_{i=1}^{n_{bus}} \sum_{vh}^{N_{PEV}^{i}(t_k)} SOCR^{i}(vh) - SOC^{i}(t_u + \tau, vh) \tag{6.21}$$

Subject to:

$$\left.\begin{matrix} (6.3)-(6.19) \\ U_L^i(t_k) = U_{L,LSMSP}^i(t_k) \end{matrix}\right\} \forall k \in \{0,1\ldots,N_p\}$$

The variables in the SMSP, $x_{SMSP}(t_k)$, are given as follows:

$$x_{SMSP}(t_k) = \begin{cases} Control\ variables: \\ D_{PEV}^i(t_k, vh), x_i(t_k) \\ State\ variables: \\ \omega(t_k), V_i(t_k), Y_{ij}(t_k), SOC^i(t_k, vh), PCH^i(t_k, vh) \end{cases} \tag{6.22}$$

Given the charging decisions obtained from the SMSP, a feasible target SOC can be calculated for each PEV $SOC_{SMSP}^{i}(t_u + \tau, vh)$. Using the objectives values obtained by solving the LSMSP and the SMSP as constraints, the CMSP can be formulated as follows:

$$Min. \quad \sum_{k=0}^{N_p} \sum_{i=1}^{n_{bus}} P_{Gi}(t_k) \times \chi_i + \sum_{k=0}^{N_p} \sum_{i=1}^{n_{bus}} C_{PEV}^{i}(t_k) \tag{6.23}$$

Subject to:

$$\left.\begin{matrix} (6.3)-(6.19) \\ U_L^i(t_k) = U_{L,LSMSP}^i(t_k) \end{matrix}\right\} \forall k_t \in \{0,1\ldots,N_p\}$$

$$SOC^i(t_u + \tau, vh) = SOC_{SMSP}^i(t_u + \tau, vh)$$

where the PEV discharging cost $C_{PEV}^{i}(t_k)$ is given as follows:

$$C_{PEV}^{i}(t_k) = \begin{cases} 0, \ \forall D_{PEV}^i(t_k, vh) \geq 0 \\ -\sum_{vh}^{N_{PEV}^{i}(t_k)} c_{PEV-kWh} \times D_{PEV}^i(t_k, vh) \times PCH^i(t_k, vh) \times \Delta t / 60, \ Otherwise \end{cases} \tag{6.23}$$

and $c_{PEV-kWh}$ is the cost of PEV discharge per *kWh*. The variables in the CMSP $x_{CMSP}(t_k)$ are given as follows:

$$x_{CMSP}(t_k) = x_{SMSP}(t_k) \tag{6.24}$$

6.4 Case studies

In this section a simulation model has been developed to implement the proposed multi-stage centralized control scheme. In the developed case studies Δt is chosen as 10 minutes and τ is chosen to be 3 hours. The proposed algorithm has been tested over an operation period of one day. The simulation model has been built in two simulation environments (MATLAB and GAMS). The islanded microgrid model and the local controllers are implemented in MATLAB. The real time measurements and forecasted data are continuously collected in the MATLAB environment and exported to GAMS, which represents the optimization function of the MGCC. The GDXMRW software interface has been used to import/export data between GAMS and MATLAB.

The 33-bus distribution test system is used in the case studies to verify the effectiveness of the proposed control scheme [96]. The system single line diagram, feeder parameters (at nominal frequency) and load power are given in Appendix A. For the purpose of the proposed study, it is assumed that the system is in the islanded microgrid mode of operation. Five dispatchable DG units have been allocated to feed the system in the islanded microgrid mode of operation. The dispatchable DG units' ratings, locations, types and cost of operation are given in Table 6.1. In order to account for the islanded microgrid operational reserve requirements, the MGCC allocates a fixed 6 % of the nominal demand from the most expensive DG unit (i.e. DG #3) as a spinning reserve. Renewable power resources with different characteristics have been installed at different locations along the test system. Five photovoltaic units each 0.1 MW rating, are installed at buses 5,7,13,21 and 27. Two wind turbines each 0.5 MW rating are installed at buses 16 and 19.

As can be seen in Table 6.2, five PEVs parking lots with different locations and capacities are assumed to exist in the test system. Based on historical data [62], a probabilistic distribution model for the arrival of vehicles and their customers' requirements has been extracted for each parking lot. The probabilistic model has been used to generate the PEVs random behavior for the day under study. Figure 6.3 shows the number of the PEVs in each parking lot during the day under study, based on the generated behavior. The PEV parking residence time is modeled as random distribution variable with mean time 540, 540, 210, 210 and 540 minutes for the five parking lots, respectively. For simplicity, all chargers are assumed to be second level chargers with 7.2 KW rating. All PEVs are assumed to have an all-electric range (AER) of 50 miles. In addition, all PEV batteries have the same charging/discharging characteristics, given in [104]

with some adjustment to match the ratings of the utilized chargers and the AER. The cost of PEV discharge $c_{PEV-kWh}$ is chosen as 0.6 $/kWh to reflect the impact of battery discharge on its life time. This price has been calculated as the equivalent gas price required for undertaking the same trip taken by 1 *kWh* of electrical energy discharged from the battery.

Statistical time series models are usually adequate for short term renewable power forecast. In this work, the auto regression moving average (ARMA) technique is used to model the wind speed and solar irradiance. The ARMA model is developed to forecast in 10 minutes intervals using MATLAB. The ARMA model parameters are determined from historical wind speed and solar irradiance data for the period. The generated wind speeds are then combined with the wind turbine parameters in order to evaluate the forecasted wind electrical power generation. Similarly, the generated solar irradiance data are combined with the photovoltaic system parameters to calculate the predictable photovoltaic power generation. The ARMA based process is developed to automatically forecast the renewable power generation over the specified prediction horizon at each time step i.e. the forecast is updated every ten minutes for the next 3 hours. In order to account for the accuracy of the forecasting model, the forecasting error is simulated by comparing the actual data (shown in Figure 6.4) with those obtained from the ARMA models. In this work it is assumed that the MGCC can forecast the regular power demand over the prediction time horizon with negligible error using historical data [103].

Table 6.1: Case study# 6-1: droop-controlled DGs' locations, ratings, types and cost of operation

DG #	Bus #	S_{Gmax} *(MVA)*	Price $/kWh
1	08	1.5	0.024
2	29	2.0	0.022
3	12	1.0	0.058
4	22	1.0	0.054
5	25	1.0	0.051

Table 6.2: Case study# 6-1 and #6-2: Parking lots locations, capacities and types

Lot #	Bus #	*Capacity (vehicles)*	Type
1	12	60	Residential
2	19	100	Residential
3	24	60	Commercial
4	29	60	Commercial
5	32	100	Residential

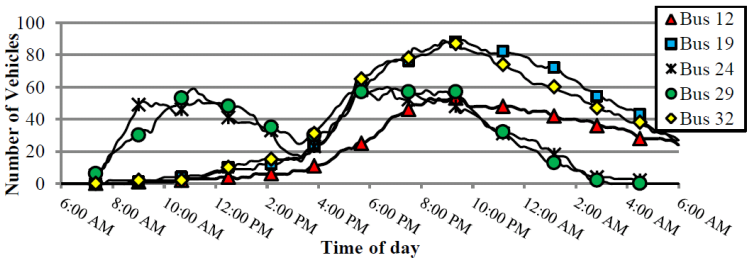

Figure 6.3: Case study# 6-1 and #6-2: the Distribution of PEVs in each parking lot during the day under study

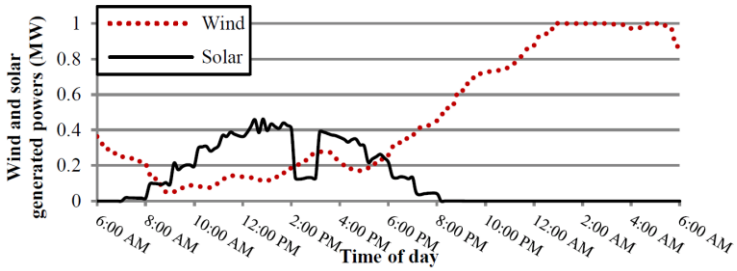

Figure 6.4: Case study# 6-1 and #6-2: wind and photovoltaic generation profiles for the day under study

Two different case studies have been carried out to evaluate the importance of the proposed algorithm. The first case study is considered to investigate the performance of the proposed scheme during normal operation (islanded microgrid has enough generation to feed all demands including PEVs and hence no load shedding is required). The second scenario examines the effectiveness of the proposed scheme when a shortage of generation exists.

6.4.1 Case study# 6-1: islanded microgrid operation with adequate generation

In this case study, it is assumed that the islanded microgrid operates in normal mode and there is enough generation to feed the regular load and PEVs demand during the day under study. Three possible scenarios have been carried out in this case study to show the effectiveness and robustness of the proposed multi-stage centralized control scheme. In the first scenario, it is assumed that there are no communication links (centralized control unit is deactivated) i.e. islanded microgrid operates with the local droop control using conventional droop parameters, in order to share the load demand of the islanded microgrid in proportional to the DG units rated capacity, and the charging of PEVs is un-coordinated. In this scenario, the static droop gains of the DG units are designed based on 0.5% and 5% allowable frequency and voltage regulation respectively; ω^* and V^* are selected arbitrary in order to

maintain adequate power-quality levels (at 1.0 p.u. and 1.03 p.u., respectively), in terms of keeping frequency and voltage within their specified operating limits, respectively. In the second scenario, it is assumed that the function of the centralized control unit is to optimally set the droop parameters of droop-controlled DG units, while the charging of PEVs is uncoordinated i.e. (no communication links between PEVs charging stations and the MGCC). In the third scenario, it is considered that the MGCC has communication links with both DG units and PEVs charging stations. Figure 6.5 shows the total charging demand of PEVs during the day under study in the third scenario (coordinated charging) compared with those obtained in the first and second scenario (uncoordinated charging). As shown in the figure, the proposed multi-stage control scheme shifted the PEVs charging demand from the periods of high loading to the periods of less loading allowing such load to be fed from less expensive DG units. Additionally, such coordination resulted in a reduction of the PEV peak load from 673 kW to 409 kW. Here it is noteworthy that considering the PEV discharging cost in the problem formulation in (6.22) forces the MGCC to avoid any PEV discharge decision during the normal operation of the islanded microgrid.

Figures 6.6 and 6.7 show the active and reactive power sharing, respectively, between the droop-controlled DG units during the day under study. Figure 6.6 (a) shows that conventional droop control can realize nearly exact active power sharing among DG units in islanded microgrids. However, as seen in Figure 6.7(a), the reactive power sharing between the DG units is not exact and depends on the system parameters i.e. mismatches in the power line impedances. Figure 6.6 (b) shows that in the second scenario the active power sharing among the DG units is scheduled to minimize the total cost of operation for the islanded microgrid. As a result of minimizing the cost of operation, DG #2 and DG #1 have the priority of sharing the active power demand. DG#5 shares in feeding the power demand only during heavily loading durations and when DG#2 and DG#1 reached to their rated capacity. Figure 6.6 (c) shows that the shift of PEVs charging reduced the active power injected from DG#5 (more expensive) by shifting some of its demand to DG #1 and 2 (less expensive) at off-peak durations. As can be seen in Figure 6.6 (c), proper coordination of PEVs resulted in reducing the amount of generation required in the period of 4-6 PM, which requires injecting active power from the more expensive DG #5. As a result, the generation cost is reduced. Table 6.3 shows the islanded microgrid generation cost for the day under study. As shown in the table, optimal droop parameters in the second scenario reduced the generation cost by 32.58% compared with the first scenario. Further, a proper coordination of the PEV charging along with the optimal droop parameters resulted in 36.75% reduction in the cost of generation.

Table 6.3: Case study# 6-1: islanded microgrid generation cost

Scenario #	*1*	*2*	*3*
Cost ($)	2290.13	1543.96	1448.48

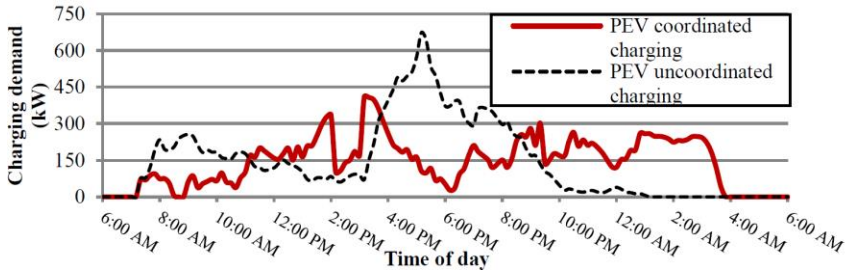

Figure 6.5: Case study# 6-1: total charging demand of PEVs during the day under study

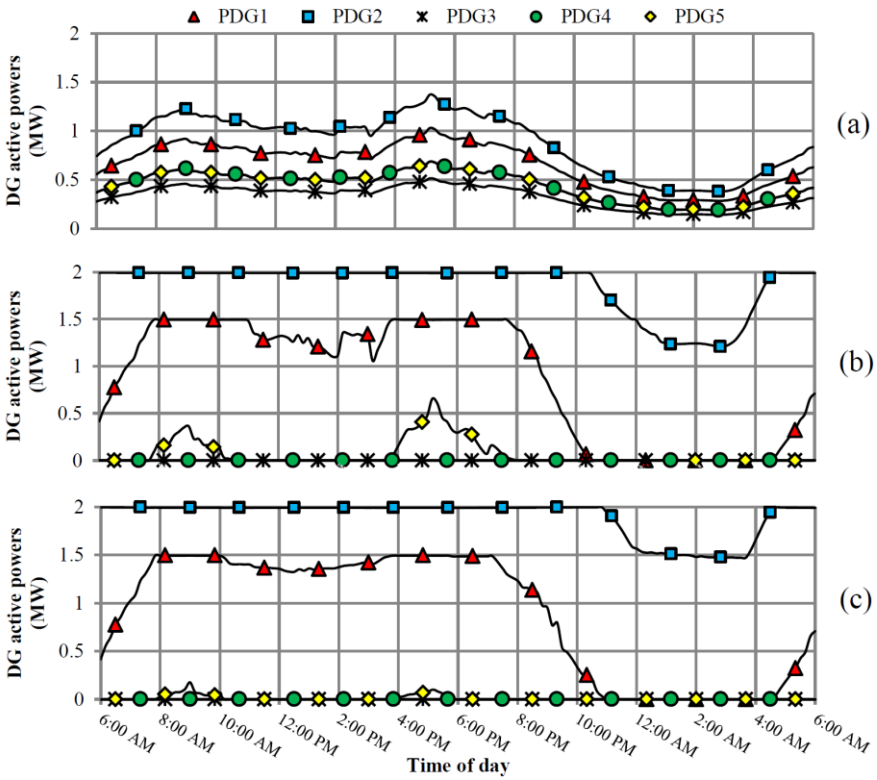

Figure 6.6: Case study# 6-1: droop-based DG units' active power generation (a) first scenario, (b) second scenario, and (c) third scenario

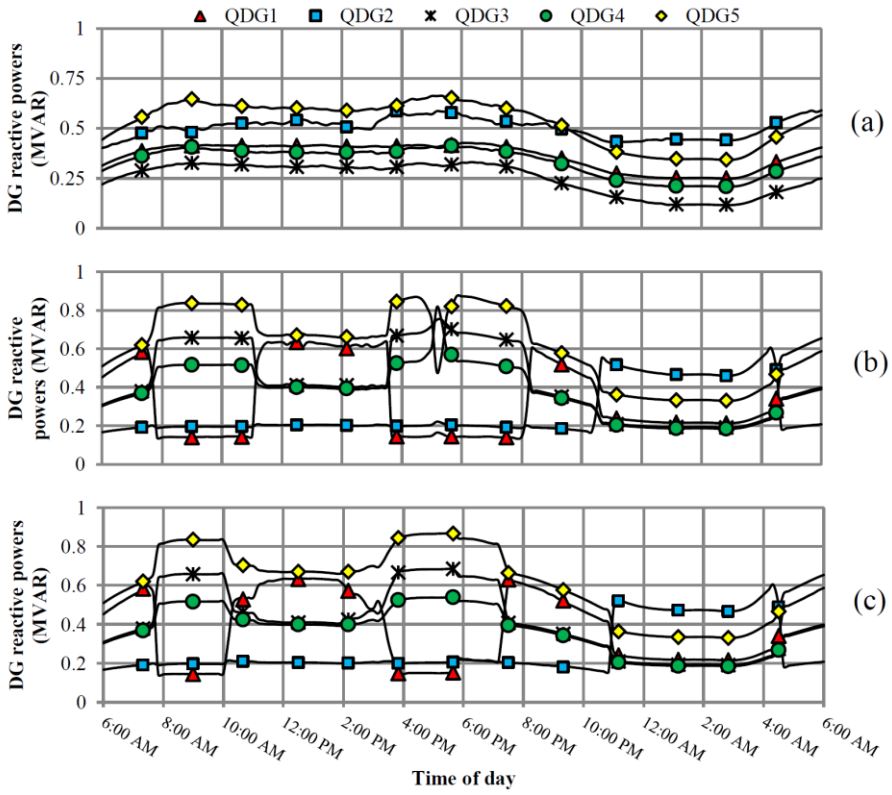

Figure 6.7: Case study# 6-1: droop-based DG units' reactive power generation (a) first scenario, (b) second scenario, and (c) third scenario

The pattern of active power sharing has a significant effect on the selection of the reactive power droop gains and consequently on the reactive power sharing between the DG units. As shown in Figure 6.7 (b) and (c), DG#2 and DG#1 inject their available reactive power during most of the day. However, to feed the total reactive power demand, DG#5, DG# 4 and DG#3, share the rest of the reactive power demand based on the impact of their reactive power on the cost of operation (system losses). As shown in the figures, during the heavy loading period (8:00am-10:30am and 4:00pm-8:00pm), the injected reactive power from DG#1 is reduced significantly to support the active power demand. As a result, the injected reactive powers from DG#5, DG# 4 and DG#3 increase to support the rest of the reactive power demand. Similar scenario can also appear in the period of 5:30pm-5:50 pm; where DG#5 acted to support the active power demand by reducing its reactive power. As such, DG#4 and DG#3 acted to support the reactive power demand. The results in this case study showed that the proposed coordination scheme can

effectively shape the PEVs charging demand in a way that results in minimizing the generation cost while satisfying the PEVs customers' requirements.

6.4.2 Case study# 6-2: islanded microgrid operation with inadequate generation

This case study tests the robustness of the proposed multi-stage control scheme during inadequate generation. In this case, it is assumed that there is a shortage in the capacity of available DG units compared to the total system demand. DG #1 and #4 are considered to be out of service. Two scenarios are carried out in this case study. The proposed multi-stage centralized control scheme is applied in the two scenarios; however, in the first scenario, it is assumed that the PEVs are not allowed to discharge. Figs. 6.8 (a) and (b) show the total islanded microgrid demand for the regular load before and after the load shedding. Also, the figures show the PEVs charging/discharging power and the total load demand including PEVs for the first and second scenarios, respectively. Table 6.4 shows the unserved regular and PEVs demand in the two scenarios. As shown in the table, allowing the PEV to discharge reduced the percentage of unserved regular loads from 2.72% to 1.61%. Similarly, the PEV discharge allowed for higher vehicle satisfaction rate by decreasing the PEV unserved load from 31.19% to 19.79%. As shown in the figures, the proposed centralized control scheme created smart charging/discharging cycles for the PEVs with long staying time to supply the load demand during the shortage of power generation. As can be seen, PEVs can operate as energy storage; where they might charge during the low loading conditions (when generation has enough power to feed the demand) followed by a discharging decision that is activated in the period at which the generation is less than the regular demand. Another observation is that based on the load points priorities, charging decisions might be initiated in certain duration even though the generation is less than the regular demand (i.e. such charging decisions are accompanied with shedding of some load points). Such charging decisions are followed by discharging decisions in a subsequent duration when the shortage in generation (power mismatch) is of larger value in order to prevent the shedding of higher priority load points. Such charging/discharging mechanism keeps automatically a flatten load shedding profile during the period of inadequate generation. Further, it is noteworthy that the charging/discharging cycles are followed by achieving the PEVs customers' satisfaction during the light loading conditions. Fig. 6.9 shows the number of load points shed throughout the day under study in the two scenarios. It is noteworthy that the load shedding mechanism is governed by the load priorities and the active power mismatch that is affected by the charging/discharging scheme of the PEVs. As shown in the figure, the proposed PEVs charging scheme reduced the active power

mismatch, thus the load shedding is reduced and the customer's reliability is improved. Hence it can be seen that the proposed algorithm reduced the number of load points' interruption.

Table 6.4: Case study# 6-2: islanded microgrid customer satisfaction indices

Scenario #	***1***	***2***
Unserved regular load (%)	2.72	1.61
Unserved PEVs (%)	31.19	19.79

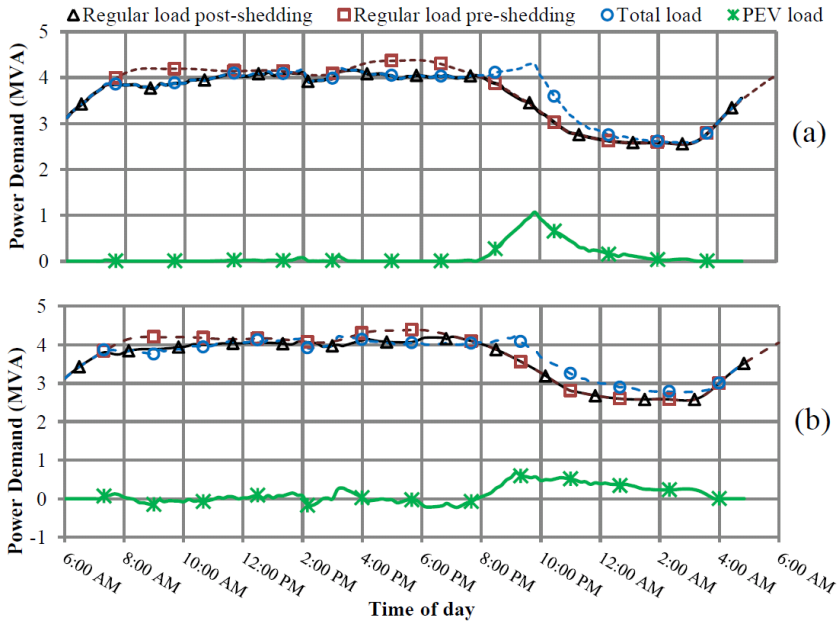

Figure 6.8: Case study# 6-2: demand profile for the day under study: (a) scenario #1, and (b) scenario #2

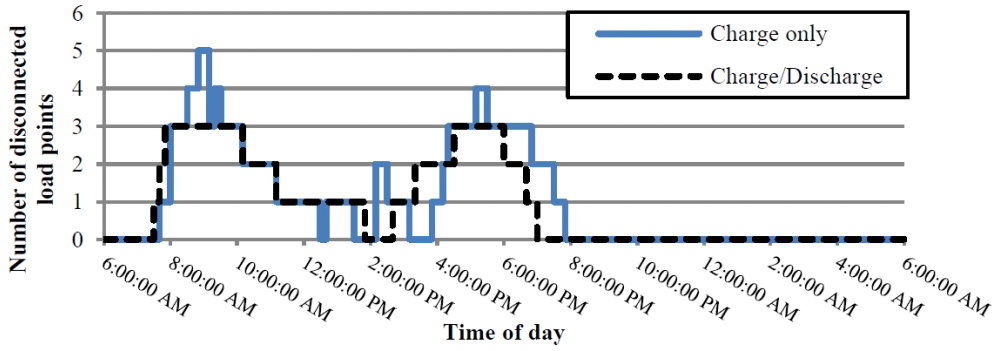

Figure 6.9: Case study# 6-2: number of load points shed during the day under study. Load points to be shed in priority ascending order are {2, 5, 14, 12, 22, 31}

6.5 Discussion

This chapter proposed a muli-stage centralized control scheme for islanded microgrid operation in the presence of high penetration of PEVs. The proposed control scheme adopts a droop-based three-stage OPF to 1) minimize the islanded microgrid load shedding during inadequate generation, 2) maximize the PEVs customers' satisfaction, and 3) minimize the islanded microgrid generation cost. The proposed control scheme takes into consideration the main features of droop-based islanded microgrid and the PEVs characteristics. Several case studies have been carried out to examine the effectiveness and robustness of the proposed scheme under different operating conditions. The results show that the proposed cooperative control scheme can effectively shape the PEVs charging in a way that results enhancing the islanded microgrid customers' reliability, while considering the islanded microgrid generation cost. Moreover, the results demonstrate the capability of PEVs to behave as an electric shifting demand, peak clipping, and as a source of energy during inadequate generation in unscheduled events of islanded microgrid. Hence, the results show that the proposed control scheme is capable of significantly reducing the islanded microgrid load shedding as well as enhancing the PEVs customers' satisfaction.

Chapter 7
Summary, Contributions and Future Work

7.1 Summary and conclusions

The research in this thesis presents new analysis and operational control algorithms to tackle some of the challenges facing the islanded microgrid operation and hence facilitate its practical implementation.

In chapter 3 a novel power flow algorithm was proposed for microgrids operating in the islanded mode. It was shown that the absence of the utility bus in the islanded mode of operation render the conventional power flow algorithms, previously proposed in the literature, ineffective. The proposed algorithm accounts for the absence of the utility bus by reformulating the power flow problem without a slack bus. Moreover, the special features of islanded microgrid systems are considered in the proposed algorithm; where: 1) some of the DG units are controlled by droop control, and 2) system frequency is not constant. A Newton trust region method was adopted to solve the set of non-linear equations describing the power flow problem in the islanded mode of operation. Simulation results and numerical comparative studies were presented to demonstrate the effectiveness of the proposed algorithm in accurately modelling islanded microgrids.

In chapter 4 it was shown that the consideration of a maximum loadability criterion in the islanded microgrid OPF problem can significantly increase the islanded microgrid loading margin. Such an increase, in the loading margin, can play a crucial role in allowing for a successful operation of islanded microgrid systems; given its limited generation resources when operating in isolation from the utility grid. Three OPF problems for islanded microgrids were proposed to allow for the required maximum loadability consideration; 1) The OPF problem for maximum loadability assessment, 2) The OPF for maximizing the system loadability, and 3) The bi-objective OPF problem for loadability maximization and generation cost minimization. Moreover, a fuzzy-based utopia tracking algorithm was developed to achieve a best compromise solution between system maximum loadability and system minimum generation costs. Comparative numerical simulation studies showed the importance and consequence of considering a system maximum loadability criterion in the OPF problem of islanded microgrids.

In chapter 5 a new probabilistic algorithm was proposed for determining the optimum choice of the droop settings for individual DG units in distribution networks when a MGCC is not available. The proposed

algorithm achieves an optimum choice of the DG units droop settings, offline, for a possible operational planning horizon within which the islanded microgrid might be initiated. Moreover, the proposed algorithm accounts for 1) the uncertainty and variability associated with renewable DG output power as well as load variability; and 2) the different microgrid configurations that can be created within a typical distribution network. By adopting a constraint hierarchy approach the proposed algorithm enhance the operation of islanded microgrids by satisfying the operational constraints of the system and expanding its loading margin, considering the different states in which the islanded system may exist. Simulation case studies demonstrate the capability of the proposed algorithm in enhancing the islanded microgrid operation through the reduction of customer interruptions and the enhancement of the islanded microgrid loadability margins.

In chapter 6 a new multi-stage control scheme for islanded microgrids with high PEV penetration was proposed. It was shown that the coordinated operation and control of islanded microgrid resources together with PEVs can play a pivotal role in the successful and optimized operation of the islanded microgrid systems. The proposed algorithm hence achieves the required functionality through; 1) coordinating the PEVs charging/discharging decisions across multiple time steps, 2) considering the uncertainty and variability associated with the output power of renewable DG units, as well as the load variability, 3) during inadequate generation periods, coordinating the PEV charging/discharging decisions with the islanded microgrid load shedding, and 4) considering the random PEVs charging behavior. Simulation studies show that the proposed control scheme can enhance the operation of islanded microgrid systems in the presence of high PEV penetration and facilitate a successful implementation of the islanded microgrid concept, under the smart grid paradigm.

7.2 Contributions

The main contributions in this thesis can be highlighted as follows:

1- Concluding and demonstrating that conventional power flow algorithms are not suitable for islanded microgrids steady-state analysis, and accordingly developing a novel power flow analysis algorithm for accurately modeling microgrid systems operating in the islanded mode.

2- Proposing and demonstrating the importance of system maximum loadability consideration in islanded microgrid systems OPF problems, and consequently developing an algorithm to achieve a best compromise solution between system maximum loadability and minimum generation cost in islanded microgrids OPF problems.

3- Concluding and demonstrating the unsuitability of conventional droop setting methodologies (based solely on DG units' capacities) for the decentralized operation of islanded microgrids including renewable energy resources, and accordingly developing an offline design methodology to enhance the decentralized operation of islanded microgrids including renewable energy resources through satisfying the system operational constraints and increasing the system loadability margins while at the same time considering the different islanded microgrid configurations that can be initiated in the distribution system.

4- Demonstrating the importance of the coordinated operation and control of islanded microgrid resources together with PEVS, and accordingly developing a coordinated control scheme to enable the islanded microgrid operation under high penetration of PEVs.

7.3 Directions for future work

In continuation of this work, the following subjects are suggested for future studies:

1- Extending the proposed islanded power flow algorithm to enable harmonic power flow consideration in islanded microgrids.

2- Optimal allocation for DG units considering the operational characteristics of islanded microgrid systems.

3- Development of a new algorithm to enable for the optimum reconfiguration of islanded microgrid systems.

Appendix A

Data of the Distribution Test Systems

Table A.1: Parameters of the 6-bus test system

Identical DG units (10 KVA (3-Ph), 127 V (L-N), 60 Hz)						
m_p *(rad/s/W)*	n_q *(V/VAR)*	ω^* (rad/sec)	V^* (V)	L_f *(mH)*	R_f *(Ω)*	C_f (μF)
9.40E-05	0.0013	377	127	1.35	0.1	150

K_{pv}	K_{iv}	H	K_{pv}	K_{iv}
5.00E-02	390	0.75	10.5	16000

Lines parameters (per-phase)			
From bus	To bus	R_{line} (Ω)	L_{line} (mH)
1	2	0.43	0.318
1	4	0.3	0.35
2	5	0.2	0.25
2	3	0.15	1.843
3	6	0.05	0.05

Loads parameters (per-phase)		
Bus number	R_{load} (Ω)	L_{load} (mH)
1	6.95	12.2
3	5.014	9.4

Table A.2: Parameters of the 38-bus test system [85] (V_{base}= 12.66 KV, S_{base}=1 MVA)

Sending bus	Receiving bus	R (p.u.)	X (p.u.)	Load at receiving bus			
				P_0 (p.u.)	Q_0 (p.u.)	k_{pv}	k_{qv}
1	2	0.000574	0.000293	0.1	0.06	0.92	4.04
2	3	0.00307	0.001564	0.09	0.04	0.18	6
3	4	0.002279	0.001161	0.12	0.08	1.51	3.4
4	5	0.002373	0.001209	0.06	0.03	0.92	4.04
5	6	0.0051	0.004402	0.06	0.02	0.18	6
6	7	0.001166	0.003853	0.2	0.1	1.51	3.4
7	8	0.00443	0.001464	0.2	0.1	1.51	3.4
8	9	0.006413	0.004608	0.06	0.02	0.18	6
9	10	0.006501	0.004608	0.06	0.02	1.51	3.4
10	11	0.001224	0.000405	0.045	0.03	1.51	3.4
11	12	0.002331	0.000771	0.06	0.035	0.92	4.04
12	13	0.009141	0.007192	0.06	0.035	1.51	3.4
13	14	0.003372	0.004439	0.12	0.08	0.92	4.04
14	15	0.00368	0.003275	0.06	0.01	1.51	3.4
15	16	0.004647	0.003394	0.06	0.02	0.18	6
16	17	0.008026	0.010716	0.06	0.02	1.51	3.4
17	18	0.004558	0.003574	0.09	0.04	0.18	6
2	19	0.001021	0.000974	0.09	0.04	0.92	4.04
19	20	0.009366	0.00844	0.09	0.04	1.51	3.4
20	21	0.00255	0.002979	0.09	0.04	0.18	6
21	22	0.004414	0.005836	0.09	0.04	0.92	4.04
3	23	0.002809	0.00192	0.09	0.05	1.51	3.4
23	24	0.005592	0.004415	0.42	0.2	1.51	3.4
24	25	0.005579	0.004366	0.42	0.2	1.51	3.4
6	26	0.001264	0.000644	0.06	0.025	1.51	3.4
26	27	0.00177	0.000901	0.06	0.025	0.18	6
27	28	0.006594	0.005814	0.06	0.02	1.51	3.4
28	29	0.005007	0.004362	0.12	0.07	1.51	3.4
29	30	0.00316	0.00161	0.2	0.6	1.51	3.4
30	31	0.006067	0.005996	0.15	0.07	0.92	4.04
31	32	0.001933	0.002253	0.21	0.1	0.92	4.04
32	33	0.002123	0.003301	0.06	0.04	1.51	3.4
8	34	0.012453	0.012453	0	0	0	0
29	35	0.012453	0.012453	0	0	0	0
12	36	0.012453	0.012453	0	0	0	0
22	37	0.003113	0.003113	0	0	0	0
25	38	0.003113	0.003113	0	0	0	0

Table A.3: Load data and line connectivity of the 25-bus unbalanced test system [87] (Z_{base}= 1.73056, S_{base}=10/3 MVA)

Sending bus	Receiving bus	Conductor type	length (ft)	Load at receiving bus					
				Phase (*a*)		Phase (*b*)		Phase (*c*)	
				P_L (KW)	Q_L (KVAR)	P_L (KW)	Q_L (KVAR)	P_L (KW)	Q_L (KVAR)
1	2	1	1000	0	0	0	0	0	0
2	3	1	500	35	25	40	30	45	32
2	6	2	500	40	30	45	32	35	25
3	4	1	500	50	40	60	45	50	35
3	18	2	500	40	30	40	30	40	30
4	5	2	500	40	30	40	30	40	30
4	23	2	400	60	45	50	40	50	35
6	7	2	500	0	0	0	0	0	0
6	8	2	1000	40	30	40	30	40	30
7	9	2	500	60	45	50	40	50	35
7	14	2	500	50	35	50	40	60	45
7	16	2	500	40	30	40	30	40	30
9	10	2	500	35	25	40	30	45	32
10	11	2	300	45	32	35	25	40	30
11	12	3	200	50	35	60	45	50	40
11	13	3	200	35	25	45	32	40	30
14	15	2	300	133.3	100	133.3	100	133.3	100
14	17	3	300	40	30	35	25	45	32
18	20	2	500	35	25	40	30	45	32
18	21	3	400	40	30	35	25	45	32
20	19	3	400	60	45	50	35	50	40
21	22	3	400	50	35	60	45	50	40
23	24	2	400	35	25	45	32	40	30
24	25	3	400	60	45	50	30	50	35

Table A.4: Impedance of different types of conductors in the 25-bus unbalanced test system

Type	Impedance (Ohms/mile)		
1	0.3686+0.6852i	0.0169+0.1515i	0.0155+0.1098i
	0.0169+0.1515i	0.3757+0.6715i	0.0188+0.2072i
	0.0155+0.1098i	0.0188+0.2072i	0.3723+0.6782i
2	0.9775+0.8717i	0.0167+0.1697i	0.0152+0.1264i
	0.0167+0.1697i	0.9844+0.8654i	0.0186+0.2275i
	0.0152+0.1264i	0.0186+0.2275i	0.9810+0.8648i
3	1.9280+1.4194i	0.0161+0.1183i	0.0161+0.1183i
	0.0161+0.1183i	1.9308+1.4215i	0.0161+0.1183i
	0.0161+0.1183i	0.0161+0.1183i	1.9337+1.4236i

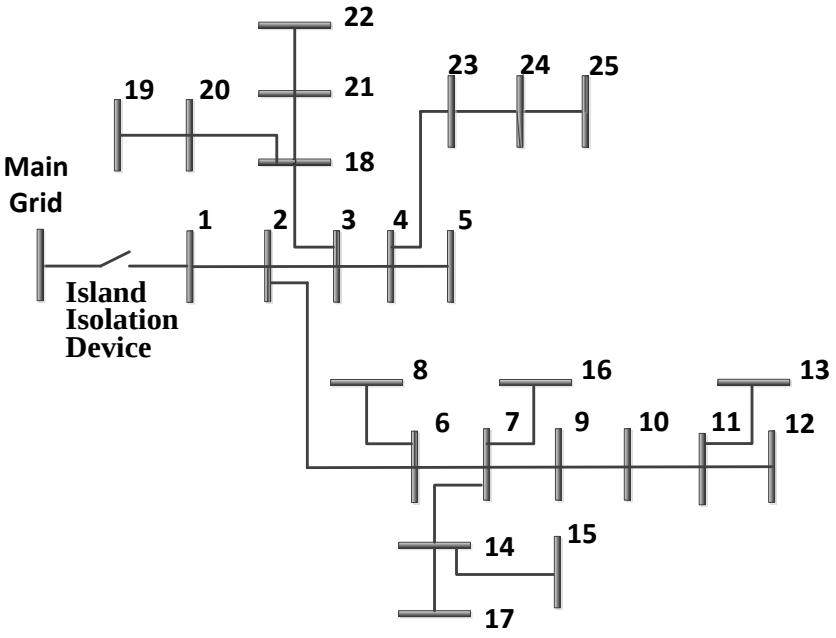

Figure A.1: The 25-bus unbalanced test system [87]

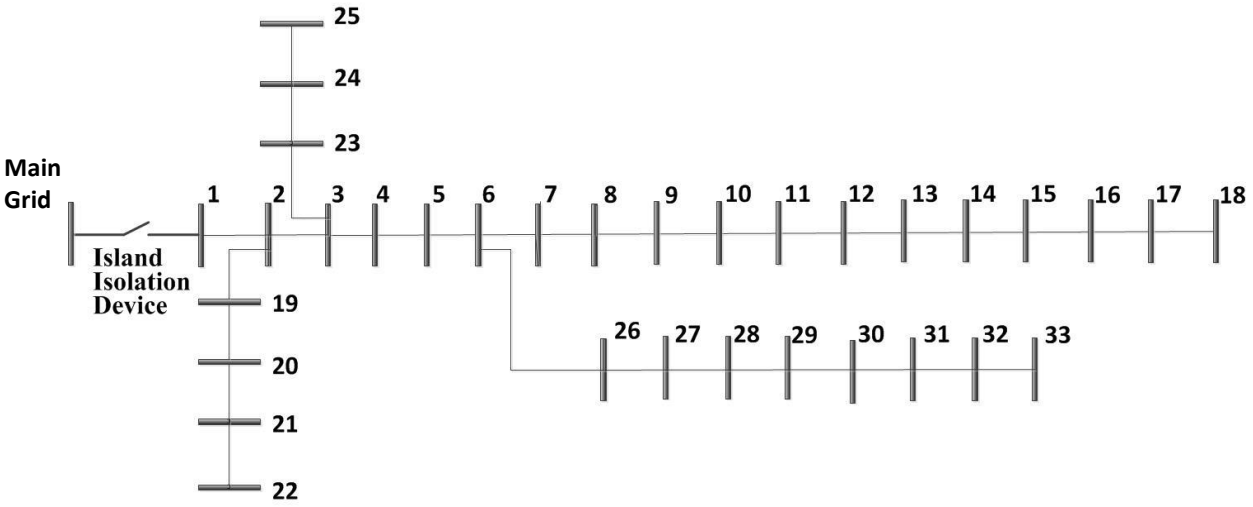

Figure A.2: The 33-bus balanced test system [96]

Table A.5: Parameters of the 33-bus test system [96] (V_{base}= 12.66 KV, S_{base}=1 MVA)

Sending bus	**Receiving bus**	$\boldsymbol{R}$ (Ohm)	$\boldsymbol{X}$ (Ohm)	**Load at receiving bus**	
				$\boldsymbol{P_L}$ (KW)	$\boldsymbol{Q_L}$ (KVAR)
1	2	0.0922	0.0470	100	60
2	3	0.4930	0.2511	90	40
3	4	0.3660	0.1864	120	80
4	5	0.3811	0.1941	60	30
5	6	0.8190	0.7070	60	20
6	7	0.1872	0.6188	200	100
7	8	0.7114	0.2351	200	100
8	9	1.0300	0.7400	60	20
9	10	1.0440	0.7400	60	20
10	11	0.1966	0.0650	45	30
11	12	0.3744	0.1238	60	35
12	13	1.4680	1.1550	60	35
13	14	0.5416	0.7129	120	80
14	15	0.5910	0.5260	60	10
15	16	0.7463	0.5450	60	20
16	17	1.2890	1.7210	60	20
17	18	0.7320	0.5740	90	40
2	19	0.1640	0.1565	90	40
19	20	1.5042	1.3554	90	40
20	21	0.4095	0.4784	90	40
21	22	0.7089	0.9373	90	40
3	23	0.4512	0.3083	90	50
23	24	0.8980	0.7091	420	200
24	25	0.8960	0.7011	420	200
6	26	0.2030	0.1034	60	25
26	27	0.2842	0.1447	60	25
27	28	1.0590	0.9337	60	20
28	29	0.8042	0.7006	120	70
29	30	0.5075	0.2585	200	600
30	31	0.9744	0.9630	150	70
31	32	0.3105	0.3619	210	100
32	33	0.3410	0.5302	60	40

Bibliography

[1] K. Moslehi and R. Kumar, "A reliability perspective of the smart grid," *IEEE Trans. Smart Grid*, vol. 1, no. 1, pp. 57-64, Jun. 2010.

[2] J. A. Momoh, "Smart grid design for efficient and flexible power networks operation and control," in *Power Systems Conference and Exposition, 2009. PSCE'09. IEEE/PES*, 2009, pp. 1-8.

[3] A. Ipakchi and F. Albuyeh, "Grid of the future," *IEEE Power and Energy Magazine*, vol. 7, no. 2, pp. 52-62, Mar. 2009.

[4] S. Favuzza, G. Graditi, M. G. Ippolito, F. Massaro, R. Musca, E. Sanseverino and G. Zizzo, "Transition of a distribution system towards an active network. Part I: Preliminary design and scenario perspectives," in *2011 International Conference on Clean Electrical Power (ICCEP)*, 2011, pp. 9-14.

[5] H. Farhangi, "The path of the smart grid," *IEEE Power and Energy Magazine*, vol. 8, no. 1, pp. 18-28, Jan. 2010.

[6] L. F. Ochoa, C. J. Dent and G. P. Harrison, "Distribution network capacity assessment: Variable DG and active networks," *IEEE Trans. Power Syst.*, vol. 25, no. 1, pp. 87-95, Feb. 2010.

[7] G. T. Heydt, "The next generation of power distribution systems," *IEEE Trans. Smart Grid*, vol. 1, no. 3, pp. 225-235, Dec. 2010.

[8] R. H. Lasseter, "Microgrids," in *IEEE Power Eng. Soc. Winter Meeting*, 2002, pp. 305-308.

[9] G. Venkataramanan and C. Marnay, "A larger role for microgrids," *IEEE Power and Energy Magazine*, vol. 6, no. 3, pp. 78-82, May 2008.

[10] "IEEE guide for design, operation, and integration of distributed resource island systems with electric power systems," IEEE Standard 1547.4, Jul. 2011.

[11] R. H. Lasseter, "Smart Distribution: Coupled Microgrids," *Proceedings of the IEEE* , vol. 99, no. 6, pp. 1074-1082, Jun. 2011.

[12] In-Su Bae and Jin-O Kim, ""Reliability Evaluation of Customers in a Microgrid," *IEEE Trans. Power Syst.*, vol. 23, no. 3, pp. 1416-1422, Aug. 2008.

[13] J. Rocabert, A. Luna, F. Blaabjerg and P. Rodríguez, "Control of Power Converters in AC Microgrids," *IEEE Trans. Power Electron.*, vol. 27, no. 11, pp. 4734-4749, Nov. 2012.

[14] R. Palma-Behnke, L. Reyes and G. Jimenez-Estevez, "Smart grid solutions for rural areas," in *IEEE 2012 Power and Energy Society General Meeting*, 2012, pp. 1-6.

[15] A. K. Basu, S. Chowdhury and S. P. Chowdhury, "Impact of Strategic Deployment of CHP-Based DERs on Microgrid Reliability," *Power Delivery, IEEE Transactions on* , vol. 25, no. 3, pp. 1697-1705, Jul. 2010.

[16] F. Katiraei and M. R. Iravani, "Power Management strategies for a microgrid with multiple distributed generation units," *IEEE Trans. Power Syst.*, vol. 21, no. 4, pp. 1821-1831, Nov. 2006.

[17] M. Marei, E. F. El-Saadany and M. M. A. Salama, "Flexible distribution generation: FDG," in *IEEE Power Engineering Society Summer Meeting*, 2002, pp. 49-53.

[18] A. Tuladhar, H. Jin, T. Unger and K. Mauch, "Parallel operation of single phase inverter modules with no control interconnections," in *12th Annual Applied Power Electron. Conf. and Exposition*, 1997, pp. 97-100.

[19] F. Blaabjerg, R. Teodorescu, M. Liserre and A. V. Timbus, "Overview of control and grid synchronization for distributed power generation systems," *IEEE Trans. Ind. Electron.*, vol. 53, no. 5, pp. 1398-1409, Oct. 2006.

[20] N. Pogaku, M. Prodanovic and T. C. Green, "Modeling, analysis and testing of autonomous operation of an inverter-based microgrid," *IEEE Trans. Power Electron.*, vol. 22, no. 2, pp. 613-625, Mar. 2007.

[21] M. Prodanovic, T. Green and H. Mansir, "A survey of control methods for parallel three-phase inverters connection," in *Proc. Inst. Elect. Eng.* , 2000, pp. 472-477.

[22] J. F. Chen and C. L. Chu, "Combination voltage-controlled PWM inverters for UPS parallel operation," *IEEE Trans. Power Electron.*, vol. 10, no. 5, pp. 547-558, Sept. 1995.

[23] Y. Pei, G. Jiang, X. Yang and Z. Wang, "Auto-master-slave control technique of parallel inverters in distributed AC power systems and UPS," in *35th Power Electron. Specialists Conf.* , 2004, pp. 2050-2053.

[24] J. A. P. Lopes, C. L. Moreira and A. G. Madureira, "Defining control strategies for microgrids islanded operation," *IEEE Trans. Power Syst.*, vol. 21, no. 2, pp. 916-924, May 2006.

[25] C. Chen, Y. Wang, J. Lai, Y. Lee and D. Martin, "Design of parallel inverters for smooth mode transfer microgrid applications," *IEEE Trans. Power Electron.*, vol. 25, no. 1, pp. 6-15, Jan. 2010.

[26] Y. A.-R. I. Mohamed and E. F. El-Saadany, "Adaptive decentralized droop controller to preserve power sharing stability of paralleled inverters in distributed generation microgrids," *IEEE Trans. Power Electron.* , vol. 23, no. 6, pp. 2806-2816, Nov. 2008.

[27] J. M. Guerrero, J. C. Vasquez, J. Matas, L. De-Vicuna and M. Castilla, "Hierarchical control of droop-controlled ac and dc microgrids-a general approach toward standardization," *IEEE Trans. Ind. Electron.*, vol. 58, no. 1, pp. 158-172, Jan. 2011.

[28] M. C. Chandorkar, D. M. Divan and R. Adapa, "Control of parallel connected inverters in standalone ac supply systems," *IEEE Trans. Ind. Appl.*, vol. 29, no. 1, pp. 136-143, Jan. 1993.

[29] J. L. Dineley, "Power system stability - Part 2 Hardware, generators and their controls," *Power Engineering*

Journal, vol. 5, no. 4, pp. 191-196, Jul. 1991.

[30] R.W. De Doncker and J. P. Lyons, "Control of three phase power supplies for ultra low THD," in *Conference Proceedings of the Sixth Annual Applied Power Electronics Conference and Exposition, APEC '91*, 1991, pp. 622-629.

[31] F. Katiraei, "Dynamic analysis and control of distributed energy resources in a micro-grid," University of Toronto, Toronto, PhD Thesis 2005.

[32] E. Coelho, P. Cortizo and P. Garcia, "Small signal stability for single phase inverter connected to stiff Ac system," in *IEEE Ind. App. Conf., 34th IAS annual meeting*, 1999, pp. 2180-2187.

[33] E. Coelho, P. Cortizo and P. Garcia, "Small-signal stability for parallel-connected inverters in stand-alone ac ac supply systems," *IEEE Trans. Ind. App.*, vol. 38, no. 2, pp. 533-542, Mar. 2002.

[34] Y. Li, D. M. Vilathgamuwa and P. C. Loh, "Design, analysis, and real-time testing of a controller for a multibus microgrid system," *IEEE Trans. Power Electron.*, vol. 19, no. 5, pp. 1195-1203, Sept. 2004.

[35] J. M. Guerrero, L. G. De-Vicuna, J. Matas, M. Castilla and J. Miret, "A wireless controller to enhance dynamic performance of parallel inverters in distributed generation systems," *IEEE Trans. Power Eelectron.*, vol. 19, no. 5, pp. 1205-1213, Sept. 2004.

[36] M. Delghavi and A. Yazdani, "An Adaptive Feedforward Compensation for Stability Enhancement in Droop-Controlled Inverter-Based Microgrids," *IEEE Trans. Power Del.*, vol. 26, no. 3, pp. 1764-1773, Jul. 2011.

[37] G. Diaz, C. Gonzalez-Moran, J. Gomez-Aleixandre and A. Diez, "Composite loads in stand-alone inverter based microgrids-modeling procedure and effects on load margin," *IEEE Trans. Power Syst.*, vol. 25, no. 2, pp. 894-904, May 2010.

[38] H. Nikkhajoei and R. Iravani, "Steady-state model and power flow analysis of electronically-coupled distributed resource units," *IEEE Trans. Power Del.*, vol. 22, no. 1, pp. 721-728, Jan. 2007.

[39] M. Z. Kamh and R. Iravani, "Unbalanced model and power-flow analysis of microgrids and active distribution systems," *IEEE Trans. Power Del.*, vol. 25, no. 4, pp. 2851-2858, Oct. 2010.

[40] M. Z. Kamh and R. Iravani, "A unified three-phase power flow analysis model for electronically coupled distributed energy resources," *IEEE Trans. Power Del.*, vol. 26, no. 2, pp. 899-909, Apr. 2011.

[41] C. A. Hernandez-Aramburo, T. C. Green and N. Mugniot, "Fuel consumption minimization of a microgrid," *IEEE Trans. Ind. Appl.*, vol. 41, no. 3, pp. 673-681, May 2005.

[42] E. Barklund, N. Pogaku, M. Prodanovic, C, Hernandez-Aramburo and T. C. Green, "Energy management in autonomous microgrid using stability-constrained droop control of inverters," *IEEE Trans. Power Electron.*, vol. 23, no. 5, pp. 2346-2352, Sept. 2008.

[43] P. H. Divshali, S. H. Hosseinian and M. Abedi, "A novel multi-stage fuel cost minimization in a VSC-based microgrid considering stability, frequency, and voltage constraints," *IEEE Trans. Power Syst.*, vol. 2, no. 28, pp. 931-939., May 2013.

[44] S. Conti, R. Nicolosi, S. A. Rizzo and H. H. Zeineldin, "Optimal dispatching of distributed generators and storage systems for MV islanded microgrids," *IEEE Trans. Power Del.*, vol. 27, no. 3, pp. 1243-1251. , Jul. 2012.

[45] A. Basu, A. Bhattacharya, S. Chowdhury and S. P. Chowdhury, "Planned scheduling for economic power sharing in a CHP-based microgrid," *IEEE Trans. Power Syst.*, vol. 27, no. 1, pp. 30-38, Feb. 2012.

[46] H. E. Farag, M. M. A. Abdelaziz and E. F. El-Saadany, "Voltage and reactive power impacts on successful operation of islanded microgrids," *IEEE Trans. Power Syst.*, vol. 28, no. 2, pp. 1716-1727, May 2013.

[47] Benyamin Khorramdel and Mahdi Raoofat, "Optimal stochastic reactive power scheduling in a microgrid considering voltage droop scheme of DGs and uncertainty of wind farms ," *Energy*, vol. 45, pp. 994-1006, 2012.

[48] A. Micallef, M. Apap, C. Spiteri-Staines and J. M. Guerrero, "Secondary control for reactive power sharing in droop-controlled islanded microgrids," in *Proc. 21st IEEE International Symposium Ind. Electron.*, 2012, pp. 1627-1633.

[49] W. Rosehart, C. Roman and A. Schellenberg, "Optimal Power Flow with complementarity constraints," *IEEE Trans. Power Syst.*, vol. 20, no. 2, pp. 813-822, May 2005.

[50] R. J. Avalos, C. A. Canizares, F. Milano and A. J. Conejo, "Equivalency of continuation and optimization to determine saddle-node and limit-induced bifurcations in power systems," *IEEE Trans. Circuits Syst.*, vol. 56, no. 1, pp. 210-223, Jan. 2009.

[51] W. Rosehart, C. Canizares and V. Quintana, "Multi-objective optimal power flow to evaluate voltage security costs in power networks," *IEEE Trans. Power Syst.*, vol. 18, no. 2, pp. 578-587, May 2003.

[52] Z. Xiao-Ping, J. Ping and E. Handschin, "Continuation Three-Phase Power Flow: A Tool for Voltage Stability Analysis of Unbalanced Three-Phase Power Systems," *IEEE Trans. Power Syst.*, vol. 20, no. 3, pp. 1320 - 1329, Aug. 2005.

[53] Y. Kataoka and Y. Shinoda, "Voltage stability limit of electric power systems with Generator reactive power constraints considered," *IEEE Trans. Power Syst.*, vol. 20, no. 2, pp. 951-962, May 2005.

[54] M. M. A. Abdelaziz and E. F. El-Saadany, "Maximum loadability consideration in droop-controlled islanded microgrids optimal power flow," *Electric Power Sys. Res.*, vol. 106, no. C, pp. 168-179, Jan. 2014.

[55] M. M. A. Abdelaziz, E. F. El-Saadany and R. Seethapathy, "Assessment of Droop-Controlled Islanded Microgrid Maximum Loadability," in *IEEE Power and Energy Society General Meeting*, 2013, pp. 1-6.

[56] G. Diaz and C. Gonzalez-Moran, "Fischer-Burmeister-Based Method for Calculating Equilibrium Points of Droop-Regulated Microgrids," *IEEE Trans. Power Syst.*, vol. 27, no. 2, pp. 959-967, May 2012.

[57] G. Diaz, "Maximum loadability of droop regulated microgrids - formulation and analysis," *IET Generation, Transmission & Distribution*, vol. 7, no. 2, pp. 175-182, Feb. 2013.

[58] M. M. A. Abdelaziz, H. E. Farag and E. F. El-Saadany, "Optimum droop parameter settings of islanded microgrids with renewable energy resources," *IEEE Trans. Sustainable Energy*, vol. 5, no. 2, pp. 434- 445, Apr. 2014.

[59] M. M. A. Abdelaziz, E. F. El-Saadany and R. Seethapathy, "Economic Droop Parameter Selection for Autonomous Microgrids Including Wind Turbines," in *the proceedings of the 3rd International Conference on Renewable Energy: Generation and Applications ICREGA2014*, Al-Ain, UAE, 2014, pp. 1-6.

[60] R. Liu, L. Dow and E.Liu, "A Survey of PEV Impacts on Electric Utilities"," in *in Proc. 2011 IEEE Innovative Smart Grid Technologies (ISGT) Conf.*, 2011, pp. 1-8.

[61] E. Akhavan-Rezai, M. F. Shaaban,E. F. El-Saadany and A. Zidan, "Uncoordinated charging impacts of electric vehicles on electric distribution grids: normal and fast charging comparison," in *in Proc.2012 IEEE Power PES General Meeting* , 2012, pp. 1-7.

[62] M. F. Shaaban, Y. M. Atwa and E. F. El-Saadany, "PEVs modeling and impacts mitigation in distribution networks," *IEEE Trans. Power Syst.*, vol. 28, no. 2 , pp. 1122 - 1131, May 2013.

[63] C. Liu, J. Wang, A. Botterud, Y. Zhou and A. Vyas, "Assessment of impacts of PHEV charging patterns on wind-thermal scheduling by stochastic unit commitment," *IEEE Trans. Smart Grid*, vol. 3, no. 2, pp. 675-683, Jun. 2012.

[64] S. Han, S. Han and K. Sezaki, "Estimation of achievable power capacity from plug-in electric vehicles for V2G frequency regulation: case studies for market participation," *IEEE Trans. Smart Grid*, vol. 2, no. 4, pp. 632-641, Dec. 2011.

[65] C. Pang, P. Dutta and M. Kezunovic, "BEVs/PHEVs as dispersed energy storage for V2B uses in the smart grid," *IEEE Trans. Smart Grid*, vol. 3, no. 1, pp. 473 - 482, Mar. 2012.

[66] Y. He, B. Venkatesh and L. Guan, "Optimal scheduling for charging and discharging of electric vehicles," *IEEE Trans. Smart Grid*, vol. 2, no. 3, pp. 1095 - 1105 , Sept 2012.

[67] S. Y. Derakhshandeh, A. S. Masoum, S. Deilami, M. Masoum and M. E. Hamedani Golshan, "Coordination of Generation Scheduling with PEVs Charging in Industrial Microgrids," *IEEE Trans. Power Syst.*, vol. 28, no. 3, Aug. 2013.

[68] M. M. A. Abdelaziz, H. E. Farag, E. F. El-Saadany and Y. Mohamed, "a novel and generalized three-phase power flow algorithm for islanded microgrids using a newton trust region method," *IEEE Trans. Power Syst.*, vol. 28, no. 1, pp. 190-201, Feb. 2013.

[69] W. H. Kersting, "Series impedance of overhead and underground lines," in *Distribution system modeling and analysis*.: Boca Raton: CRC Press, 2002, ch. 4, pp. 77-108.

[70] IEEE Task Force on Load Representation for Dynamic Performance, "Bibliography on load models for power flow and dynamic performance simulation," *"IEEE Trans. Power Syst.*, vol. 10, no. 1, pp. 523–538, Feb. 1995.

[71] P. Kundur, "“Power system loads," in *Power System Stability and Control*.: New York: McGraw-Hill, 1994, ch. 7, pp. 271-314.

[72] T. C. Green and M. Prodanovic, "Control of inverter-based micro-grids," *Elect. Power Syst. Res.*, vol. 77, no. 9, pp. 1204-1213, Jul. 2007.

[73] J. M. Guerrero, L. G. De-Vicuna, J. Matas, M. Castilla and J. Miret, "Output impedance design of parallel-connected UPS inverters with wireless load-sharing control," *IEEE Trans. Ind. Electron.*, vol. 52, no. 4, pp. 1126-1135, Aug. 2005.

[74] J. M. Guerrero, J. Matas, L. G. De-vicuna, M. Castilla and J. Miret, "Decentralized control for parallel operation of distributed generation inverters using resistive output impedance," *IEEE Trans. Ind. Electron.*, vol. 52, no. 2, pp. 994-1004, Apr. 2007.

[75] W. Yao, M. Chen, J. Matas, J. M. Guerrero and Z.-M. Qian, "Design and analysis of the droop control method for parallel inverters considering the impact of the complex impedance on the power sharing," *IEEE Trans. Ind. Electron., vol. 58, no. 2, pp. 576-588*, vol. 58, no. 2, pp. 576-588, Feb. 2011.

[76] K. De Brabandere, B. Bolsens, J. V. den Keybus, A. Woyte, J. Driesen and R. Belmans, "A voltage and frequency droop control method for parallel inverters," *IEEE Trans. Power Electron.*, vol. 22, no. 4, pp. 1107-1115, Jul. 2007.

[77] D. Shirmohammadi, H. W. Hong, A. Semlyen and G. X. Luo, "A compensation based power flow method for weakly meshed distribution and transmission networks," *IEEE Trans. Power Syst*, vol. 3, no. 2, pp. 753-762, May 1988.

[78] G. X. Luo and A. Semlyen, "Efficient load flow for large weakly meshed networks," *IEEE Trans. Power Syst.*, vol. 5, no. 4, pp. 1309-1316, Nov. 1990.

[79] C. S. Cheng and D. Shirmohammadi, "C. S. Cheng and D. SA three-phase power flow method for real-time distribution system analysis," *IEEE Trans. Power Syst.*, vol. 10, no. 2, pp. 671-679, May 1995.

[80] M. M. A. Abdelaziz, H. E. Farag, E. F. El-Saadany and Y. Mohamed, "A globally convergent trust-region method for power flow studies in active distribution systems," in *IEEE Power and Energy Society General Meeting*, 2012, pp. 1-7.

[81] J. Nocedal and S. J. Wright, "Trust-region methods," in *Numerical optimization, 2nd ed.*: New York: Springer, 1999, ch. 4, pp. 66-100.

[82] A. R. Conn, N. I. M. Gould and P. L. Toint, "Global convergence of the basic algorithm," in *Trust-region methods*.: Philadelphia: SIAM, 2000, ch. 6, pp. 115-167.

[83] J. J. More and D. C. Sorensen, "Computing a trust region step," *J. Sci. Stat. Comput.*, vol. 4, pp. 553-572, Sept. 1983.

[84] H. E. Farag, E. F. El-Saadany, R. El-Shatshat and A. Zidan, "A generalized power flow analysis for distribution systems with high penetration of distributed generation," *Elect. Power syst. Res.*, vol. 81, no. 7, pp. 1499-1506, Jul. 2011.

[85] D. Singh, R. K. Misra and D. Singh, "Effect of load models in distributed generation planning," *IEEE Trans. Power Syst.*, vol. 22, no. 4, pp. 2204-2212, Nov. 2007.

[86] E. Rokrok and M. E. H. Golshan, "Adaptive voltage droop scheme for voltage source converters in an islanded multibus microgrid," *IET Gen., Transm., Distrib.*, vol. 4, no. 5, pp. 562-578, May 2010.

[87] G.K. V. Raju and P.R. Bijwe, "Efficient reconfiguration of balanced and unbalanced distribution systems for loss minimisation," *IET Gen., Transm., Distrib.*, vol. 2, no. 1, pp. 7-12, Jan. 2008.

[88] N.R. Ullah, K. Bhattacharya and T. Thiringer, "Wind farms as reactive power ancillary service providers-technical and economic issues ," *IEEE Trans. Energy Convers.*, vol. 24, no. 3, pp. 661-672, Sept. 2009.

[89] M. M. A. Abdelaziz and E. F. El-Saadany, "Determination of Worst Case Loading Margin of Droop-Controlled Islanded Microgrids," in *The 3rd International Conference on Electric Power and Energy Conversion Systems*, 2013, pp. 1-6.

[90] Su Xiangjing, P. Wolfs and M. A. S. Masoum, "Optimal operation of multiple unbalanced distributed generation sources in three-phase four wire LV distribution network," in *In proceedings of 22nd Australasian Universities Power Engineering Conference (AUPEC)*, 2012, pp. 1-6.

[91] R.T. Marler and J.S. Arora, "Survey of multi-objective optimization methods for engineering," *Struct. Multidisc. Optim.*, vol. 26, no. 1, pp. 369–395, 2004.

[92] V. M. Zavala and A. Flores-Tlacuahuac, "Stability of multiobjective predictive control: a utopia-tracking approach," *Automatica*, vol. 48, no. 10, pp. 2627-2632, 2012.

[93] V. M. Zavala, "Real-time resolution of conflicting objectives in building energy management: an utopia-tracking approach," in *In proceedings of the 5th national conference of IBPSA-USA*, 2012, pp. 1-6.

[94] C. Huang, H. Yang and C. Huang, "Bi-objective power dispatch using fuzzy satisfaction maximizing decision approach," *IEEE Trans. Power Syst.*, vol. 12, no. 4, pp. 1715-1721, Nov. 1997.

[95] A. Fischer, "A special newton-type optimization method," *Optimiz.:J. Math. Program. Oper. Res.* , vol. 24, no. 3, pp. 269-284, 1992.

[96] M. E. Baran and F. F. Wu, "Network reconfiguration in distribution systems for loss reduction and load balancing," *IEEE Tras. Power Syst.*, vol. 4, no. 2, pp. 1401-1407, Apr. 1989.

[97] Y. M. Atwa, E. F. El-Saadany, M. M. A. Salama, R. Seethapathy, M. Assam and S. Conti, "Adequacy evaluation of distribution system including wind/solar DG during different modes of operation," *IEEE Trans. Power Syst.*, vol. 26, no. 4, pp. 1945 - 1952, Nov. 2011.

[98] G. Díaz, C. González-Morán and C. Viescas, "Operating point of islanded microgrids consisting of conventional doubly fed induction generators and distributed supporting units," *IET Renewable Power Generation*, vol. 6, no. 5, pp. 303-314, Sept. 2012.

[99] H. E. Farag, M. M. A. Abdelaziz and E. F. El-Saadany, "The Effects of Renewable Energy Resources on the Implementation of Distributed Resources Islanded Systems," in *IEEE Power and Energy Society General Meeting 2013*, 2013, pp. 1-6.

[100] A. Boring, R. Duisberg, B. Freeman-Benson, A. Kramer and M. Woolf, "Constraint Hierarchies ," in *Proc. OOPSLA'87*, 1987, pp. 48-60.

[101] C. Singh and Y. Kim, "An efficient technique for reliability analysis of power systems including time dependent sources ," *IEEE Trans. Power Syst.*, vol. 4, no. 3, pp. 1090-1096, Aug. 1989.

[102] M. M. A. Abdelaziz, M. F. Shabaan, H. E. Farag and E. F. El-Saadany, "A Multistage Centralized Control Scheme for Islanded Microgrids With PEVs," *IEEE Trans. Sustainable Energy*, to be published DOI: 10.1109/TSTE.2014.2313765.

[103] R. Faranda, A. Pievatolo and E. Tironi, "Load Shedding: A New Proposal," *IEEE Trans. Power Syst.*, vol. 22, no. 4, pp. 2086-2093, Nov. 2007.

[104] F. Marra, Ya Yang Guang, C. Traholt, E. Larsen, C. N. Rasmussen and You Shi, "Demand profile study of battery electric vehicle under different charging options," in *Proc. IEEE Power and Energy Society General Meeting, 2012* , 2012, pp. 1-7.